May 2020

Quantitative Optical Imaging of Metabolic and Structural Biomarkers in Rodent Injury Models

Shima Mehrvar
University of Wisconsin-Milwaukee

QUANTITATIVE OPTICAL IMAGING OF METABOLIC AND

STRUCTURAL BIOMARKERS IN RODENT INJURY MODELS

by

Shima Mehrvar

A Dissertation Submitted in

Partial Fulfillment of the

Requirements for the Degree of

Doctor of Philosophy

in Engineering

at

The University of Wisconsin-Milwaukee

May 2020

ABSTRACT

QUANTITATIVE OPTICAL IMAGING OF METABOLIC AND STRUCTURAL
BIOMARKERS IN RODENT INJURY MODELS

by

Shima Mehrvar

The University of Wisconsin-Milwaukee, 2020
Under the Supervision of Professor Mahsa Ranji

The assessment of organ metabolic function using optical imaging techniques is an overgrowing field of disease diagnosis. The broad research objective of my PhD thesis is to detect quantitative biomarkers by developing and applying optical imaging and image processing tools to animal models of human diseases. To achieve this goal, I have designed and implemented an optical imaging instrument called *in vivo* fluorescence imager to study wound healing progress. I have also developed a 3-dimensional (3D) vascular segmentation technique that uses intrinsic fluorescence images of whole organs.

Intrinsic fluorophores (autofluorescence signals) provide information about the status of cellular bioenergetics in different tissue types. Reduced nicotinamide adenine dinucleotide (NADH) and oxidized flavin adenine dinucleotide (FAD) are two key Krebs cycle coenzymes in mitochondria, which are autofluorescent. The ratio of these two fluorophores (NADH/FAD) is used as an optical biomarker for mitochondrial redox state of the tissues. The custom-designed optical tools have enabled me to probe the metabolic state of diseases as well as structural information of the organs at different regimes (*in vivo,* at cryogenic temperature, and *in vitro*). Here are the main projects that I have conducted and significantly contributed to:

1) **Fluorescent metabolic imaging.** I have designed and implemented an *in vivo* fluorescence imaging device to study diabetic wounds in small animals. This device can monitor the dynamics of the metabolism of the skin by capturing the images of the surface fluorescence of NADH and FAD. The area of the wounds can also be monitored simultaneously. The spatiotemporal mitochondrial redox ratio changes can give information on the status of wound healing online. This device was utilized to study diabetic wounds and the effect of photo-biomodulation on the wound healing progress.

   I have also utilized the optical cryo-imaging system to study the three-dimensional (3D) mitochondrial redox state of kidneys, hearts, livers, and wound biopsies of the small animal models of various injuries. For example, cryo-imaging was conducted on irradiated rat hearts during ischemia-reperfusion (IR) to investigate the role of mitochondrial metabolism in the differential susceptibility to IR injury. Also, I developed a 3D image processing tool that can segment and quantify the medullary versus the cortical redox state in the kidneys of animal injury models.

2) **3D Vascular-Metabolic Imaging (VMI).** I have designed VMI, an image processing algorithm that segments vascular networks from intrinsic fluorescence. VMI allows the simultaneous acquisition of vasculature and metabolism in multiple organs. I demonstrate that this technique provides the vascular network of the whole organ without the need for a contrast agent. A proof validation has performed using TdTomato fluorescence expressing endothelium. The VMI also showed convincing evidence for the "minimum work" hypothesis in the vascular network by following Murray's law. For a proof-of-concept, I have also utilized a partial body irradiation model that VMI can provide information on radiation-induced vascular regression.

3) **Time-lapse fluorescence microscopy.** I have utilized fluorescence microscopy to quantify the dynamics of cellular reactive oxygen species (ROS) concentration. ROS is imaged and quantified under oxygen or metabolic stress conditions in cells *in vitro*. This approach enabled me to study the sensitivity of retinal endothelial cells and pericytes to stress under high glucose conditions.

In short, I developed and utilized optical bio-instrumentation and image processing tools to be able to detect metabolic and vascular information about different diseases.

To my parents,

for always loving and supporting me.

TABLE OF CONTENTS

LIST OF FIGURES

LIST OF TABLES

LIST OF ABBREVIATIONS

3D - Three-Dimensional

AB/AM - antibiotic/antimycotic

ACE - Angiotensin-Converting Enzyme

ADP - Adenosine Diphosphate

ATP - Adenosine Triphosphate

CCD - Charged Coupled Device

DNA - Deoxyribose Nucleic Acid

DMEM - Dulbecco's Modified Eagle's Medium

DR - Diabetic Retinopathy

eNOS - endothelial nitric oxide synthase

EC - Endothelial Cell

ETC - Electron Transport Chain

FAD - Flavin Adenine Dinucleotide

FBS - Fetal Bovine Serum

FR - Far red

H&E - Hematoxylin and Eosin

HBSS - Hank's Balanced Salt Solution

HG - High Glucose

IR - Ischemia Reperfusion

IRI - Ischemia Reperfusion injury

IRirr - Ischemia Reperfusion irradiated

IRnon - Ischemia Reperfusion non-irradiated

Isc60 - Ischemia for 60 minutes

Isc90 - Ischemia for 90 minutes

ISCirr - Ischemia irradiated

ISC - Ischemia non-irradiated

Lisino - Lisinopril

LN_2 - Liquid Nitrogen

LT - Liver Transplantation

Micro-CT - Micro-Computed Tomography

NADH - Nicotinamide Adenine Dinucleotide

NADPH - Nicotinamide Adenine Dinucleotide Phosphate

NAD(P)H - Combination of NADH and NADPH

NG - Normal Glucose

NIRS - Near-infrared

NIRS - Near-infrared Spectroscopy

OS - Osmolality

OS - Oxidative Stress

PBI - Partial Body Irradiation

PAEC - Pulmonary Artery Endothelial Cell

PBS - Phosphate Buffered Saline

PC - Pericyte

PCP - Pentachlorophenol

PBM - Photobiomodulation

POTS - Postural Orthostatic Tachycardia Syndrome

REC - Retina Endothelial Cells

RNS - Reactive Nitrogen Species

ROS - Reactive Oxygen Species

RPC - Retina Pericyte

RR - Redox Ratio

SD - Sprauge Dawley

TC - Time Control

TCirr – Time Control irradiated

TCnon – Time Control non-irradiated

UNX - Unilateral Nephrectomy or Uninephrectomy

VMI - Vascular-Metabolic Imaging

WTI - Whole Thoracic Irradiation

ACKNOWLEDGMENTS

Chapter 1

Introduction

1. Introduction

The advancement of optical imaging technologies is one of the fastest-growing research areas. Most of these studies are focused on understanding biological systems and disease diagnosis by the determination of tissue properties. Optical imaging techniques combine safe radiation (non-ionizing) with fast, low-cost, and high-contrast imaging [1]. Among optical imaging systems, fluorescence imaging can provide biochemical information and functional imaging on cells, tissues, and even the whole organ.

The research presented here includes the development of fluorescence imaging instruments in different regimes, conducting experiments, acquiring images, and processing them to extract markers for tissue metabolism and structure. This information bridges physiological function to the tissue structure, which is one of the most important information in understanding, treatment, and prevention of disease.

1.1. Major contributions

I have contributed in the following 3 major areas:

1.1.1. Optical bio-instrumentation

I have designed and implemented an optoelectronic device called *in vivo* fluorescence imager. It is designed to be able to monitor intrinsic mitochondrial fluorophores, namely NADH and FAD, from the surface of skin *in vivo*. I have also been involved in designing a user interface platform to control the device and synchronize the acquisition. The optical design of the device has been upgraded to be able to translate the system to future clinical applications.

1.1.2. 3D image processing of fluorescence cryo-images

The 3D fluorescence cryo-imager has conventionally been utilized to capture the 3D images of NADH and FAD. My contribution is the implementation of 3D image processing algorithms on the metabolic cryo-images to visualize the morphology alongside the biochemistry of multiple organs. This can importantly give both physiological and anatomical information.

To analyze the heterogeneity of the mitochondrial fluorophores regarding the anatomy of a kidney, a **medullary and cortical segmentation algorithm** is designed and implemented. This provides a platform to study animal injury models and their effects on the regional mitochondrial redox state in kidneys. Using this tool, the effect of partial body irradiation and lisinopril treatment afterwards on kidneys have been studied.

Vascular-metabolic imaging (VMI) using intrinsic fluorescence is another technique that I have designed to extract and quantify the 3D vessel network of whole organs from label-free fluorescence images. VMI has been validated using a TdTomato rat expressing endothelium. I showed that VMI fallows the minimum work hypothesis proposed by Murray's law, and the segmented vasculature has successfully detected the defective vasculature and the resulting impaired blood circulation in radiation-induced injuries.

1.1.3. Experimentation, image acquisition, and data interpretation

The first two mentioned contributions were for studying the underlying mechanism of multiple animal injury models and the effect of specific treatments on them. For that, I involved in experimentation, image acquisition, and interpretation of the metabolic data from the following animal injury models: a) the effect of radiation-induced injuries and lisinopril mitigation on the kidney, b) the susceptibility of the irradiated hearts to further ischemia-reperfusion injury, c)

3

ischemia-reperfusion injury in liver, d) diabetic wound healing and the effect of photobiomodulation, e) Unilateral nephrectomy, and e) Tmem overexpression of hearts.

Conducting all these experimental studies required the assembly of the required tools and designing experimental protocols to study the metabolism in the cryogenic, *in vivo,* and *in vitro* regimes. For each regime used in this study, unique treatment and preparation of the tissues, as well as proper imaging and acquisition methods are required. The cells, samples, and surgery needs are provided by the Medical College of Wisconsin, the University of Wisconsin-Madison, and the College of Nursing at the University of Wisconsin-Milwaukee. My PhD contributions and research are published in the following peer-reviewed journals and conference proceedings.

Journal Publications

J1. **S Mehrvar**, S Mostaghimi, F Foomani, N Narayanan, B Fish, AKS Camara, MM Medhora, and M. Ranji, "3D vascular-metabolic imaging using inverted intrinsic fluorescence," (In submission process)

J2. **S Mehrvar**, S Mostaghimi, FH Foomani, B Abroe, JT Eells, S Gopalakrishnan and M Ranji, "670nm Photobiomodulation improves the Mitochondrial Redox State of Diabetic Wounds," (Submitted)

J3. **S Mehrvar**, FH Foomani, S Shimada, C Yang, N Zheleznova, S Mostaghimi, A Cowley, and M Ranji, "The Early Effects of Uninephrectomy on Rat Kidney Metabolic State Using Optical Imaging," (under revision)

J4. S Gopalakrishnan, **S Mehrvar**, S Maleki, H Schmitt, P Summerfelt, AM Dubis, B Abroe, TB Connor, J Carroll, W Huddleston, M Ranji, and JT Eells, "Photobiomodulation Preserves

Mitochondrial Redox State and is Retinoprotective in a Rodent Model of Retinitis Pigmentosa," (In submission process).

J5. **S Mehrvar**, K Rymut, F Foomani, S Mostaghimi, JT Eells, M Ranji, and S Gopalakrishnan, "Noninvasive fluorescence imaging of mitochondrial redox state to assess diabetic wounds," *IEEE Journal of Translational Engineering and Health Medicine,* (2019)

J6. **S Mehrvar**, MF la Cour, MM Medhora, AKS Camara, and M Ranji, "Optical Metabolic Imaging for Assessment of Radiation-Induced Injury to Rat Kidney and Mitigating by Lisinopril," *Annals of Biomedical Engineering*, (2019)

J7. SA Lewis, T Takimoto, **S Mehrvar**, H Higuchi, A Doebley, G Stokes, N Sheibani, S Ikeda, M Ranji, and A Ikeda. "The effect of Tmem135 overexpression on the mouse heart," *PloS one*, (2018)

J8. P Kadamati, JJ Sugar, BJ Quirk, **S Mehrvar**, GG Chelimsky, HT Whelan, TC Chelimsky, and M Ranji, "Near-infrared spectroscopy muscle oximetry of patients with postural orthostatic tachycardia syndrome," *Journal of Innovative Optical Health Sciences,* (2018)

J9. Z Ghanian, **S Mehrvar**, N Jamali, N Sheibani, and M Ranji, "Time-lapse microscopy of oxidative stress demonstrates metabolic sensitivity of retinal pericytes under high glucose condition," *Journal of Biophotonics,* (2018)

J10. **S Mehrvar**, MF la Cour, JS Heisner, M MasoudiMotlagh, MM Medhora, M Ranji, AKS Camara, "Optical metabolic imaging of irradiated rat heart exposed to ischemia–reperfusion injury," *Journal of Biomedical Optics*, (2018)

J11. **S Mehrvar**, MF la Cour, J Kim, A Martin, MA Zimmerman, JC Hong, and M Ranji, "Optical imaging for the assessment of hepatocyte metabolic state in ischemia and reperfusion injuries," *Biomedical Optics Express*, (2017)

Selected Conference Proceedings and Presentations

C1. S Mostaghimi, **S Mehrvar**, FH Foomani, B Abroe, JT Eells, M Ranji, and S Gopalakrishnan, **"**The Effect of NIR Light Treatment in Metabolic State of Diabetic Wounds," *BMES*, Philadelphia (2019)

C2. **S Mehrvar**, F Foomani, S Mostaghimi, M Medhora, AKS Camara, and M Ranji, **"**Radiation-induced Injuries to Rat Kidney Vasculature," *BMES*, Philadelphia (2019)

C3. FH Foomani, **S Mehrvar**, S Mostaghimi, S Shimada, C Yang, N Zheleznova, AW Cowley Jr., and Mahsa Ranji, **"**The Early Effects of Uninephrectomy on Rat Kidney Metabolic State Using Optical Imaging," *BMES*, Philadelphia (2019)

C4. **S Mehrvar**, KT Rymut, JT Eells, M Ranji, and S Gopalakrishnan, "Optical imaging for the metabolic redox state assessment of wound healing in diabetic mice," *Biophotonics Congress: Optics in the Life Sciences*, Tucson (2019)

C5. **S Mehrvar**, MF la Cour, MM Medhora, AKS Camara, and M Ranji, "Optical cryoimaging for assessment of radiation-induced injury to rat kidney metabolic state," *Proc. of SPIE*, San Francisco (2018)

C6. **S Mehrvar**, KT Rymut, JT Eells, M Ranji, and S Gopalakrishnan, "When time does not heal wounds: optical imaging of diabetic wounds," *three-minute thesis competition (3MT),* Milwaukee (2018)

C7. **S Mehrvar**, FH Foomani, S Mostaghimi, MM Medhora, AKS Camara, and M Ranji, "Optical cryoimaging to assess metabolic state of radiation-induced injury in rat kidney," *SPIE BIOS,* San Francisco (2018*)*

C8. **S Mehrvar**, MF la Cour, J Kim, A Martin, MA Zimmerman, JC Hong, and M Ranji, "Optical imaging for liver transplant application," *5th Annual Solid Organ Transplantation Research Symposium,* Milwaukee (2017)

C9. Z Ghanian, **S Mehrvar**, N Jamali, N Sheibani, and M Ranji, "A Comparison of retina endothelial cells and pericytes in metabolic sensitivity using time-lapse microscopy," *McPherson Eye Research Institute Poster Session,* Madison (2017)

C10. **S Mehrvar**, MF la Cour, M Medhora, AKS Camara, and M Ranji, "Ischemia reperfusion in hearts: optical cryo-imaging," *Milwaukee Engineering Research Conference*, Milwaukee (2017)

C11. **S Mehrvar**, MF la Cour, MM Medhora, AKS Camara, and M Ranji, "Optical Cryoimaging of Hearts during Ischemia and Reperfusion," *IEEE Larry Hause Student Poster Competition*, Milwaukee (2017)

C12. **S Mehrvar**, Z Ghanian, G Kondouri, AKS Camara, M Ranji, "Time-lapse microscopy of lung endothelial cells under hypoxia," *Proc. of SPIE*, San Francisco (2017)

1.2. Biological backgrounds

1.2.1. Organ anatomy and vasculature

Defective vasculature and the resulting impaired blood circulation in organs cause pathological injures, such as organ failure and stroke [2]. Therefore, vascular imaging has a pivotal role in diagnosis, follow-up of disease evolution, and assessment of treatment efficacy [3]. Assessment of vascular structure in rodent models is key to characterize organ vasculatures quantitatively [4, 5]. This quantitation could be beneficiary in analyzing conditions, such as hypertension [6], diabetes [7], and retinopathy [8]. Vascular imaging is also important in therapeutic angiogenesis [9].

The gold standard for vascular imaging of small animal organs is histology, which has a major limitation for obtaining a 3D picture of structural components as a connected vascular tree [10]. Additionally, adapting this technique to small animals besides transgenic mice [11] requires the development of molecular tools such as specific antibodies [12, 13]. Imaging modalities such as micro-computed tomography (micro-CT) [4, 14], ultra-microscopy [14], near-infrared fluorescence imaging [15], magnetic resonance imaging [16], and ultrasound imaging [17] are existing tools for vascular imaging in 3D, but they are complex and costly. Labeling with a contrast agent is the only way to produce the needed contrast for most vascular imaging technologies [18]. A solvent can also be used to optically clear the tissue and overcome the limiting 3D vascular image contrast in high scattering organs like the kidney [19]. Imaging systems typically provide information about just one biological marker that limits the capacity to decipher complex disease with multiple hallmarks [20]. Integrating multiple imaging modalities to have a hybrid imaging tool can produce multi-parametric data set [21]. For instance, positron emission tomography (PET)

8

is the gold standard for molecular imaging. A hybrid imaging technology, such as PET-CT [22] acquires anatomical and molecular information, which in turn comes with increased cost, acquisition time, and complexity.

1.2.2. Cell physiology and metabolism

The structural and functional units of life are cells, the building block of all known living organisms [23]. Many injuries and diseases can be traced back to irregularities in the behavior within the cell [24]. Early detection and treatment of such injuries could lead to a significantly lower rate of permanent damage and help in reducing further therapy costs.

Mitochondria play central roles in various key cellular processes, such as ATP production, the regulation of calcium homeostasis, cell death pathways, and disposal of ROS [23]. The chemical reactions in mitochondria result in providing energy for the cell that is essential for the organism to remain healthy and viable. Mitochondria are specialized for aerobic respiration in the presence of oxygen [25]. In this process, a chain of mitochondrial coenzymes is oxidized, resulting in adenosine triphosphate (ATP), which is the unit of energy for the cells. Any irregularity in the amount of oxygen in the cell and its surrounding environment leads to perturbation to cell functions and eventually, cell death [26].

The electron transport chain, represented in Figure 1 is a complex system of chemical reactions that take place in the inner mitochondrial membrane to produce ATP [23]. In the electron transport chain, two coenzymes, nicotinamide adenine dinucleotide (NADH) and flavin adenine dinucleotide (FADH2), are oxidized through a series of protein complexes [23]. A change in the oxidation state of these two cofactors, or in other words, a change in the concentration of the oxidized form, is a direct marker of a change in tissue oxidation status and metabolism [27].

9
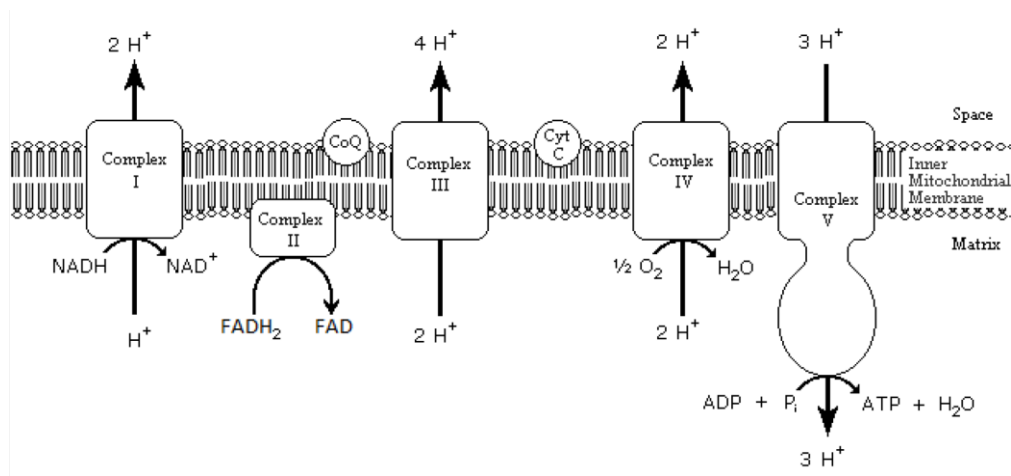
Figure 1: A simplified block diagram of the electron transport chain. NADH plays role in complex I and FADH2 in complexII.

The normal metabolism of oxygen has some natural by-products, which can produce ROS. ROS are chemically reactive molecules containing oxygen and play a vital role in cell signaling and redox regulating. The excessive amount of ROS leads to oxidative stress that is greatly involved in pathologies of various diseases [28]. In mitochondria, incomplete processing of oxygen and the release of free electrons result in the production of mitochondrial ROS, produced at a rate higher than their scavenging capacity [29, 30]. Any irregularity in the amount of oxygen introduced to the mitochondria represents an imbalance between the production and consumption of ROS. A slight increase in oxidative stress leads to mitophagy, in which the mitochondria degrades, but the cell manages to recycle the nutrients released. However, in extreme case, the excessive amount of ROS or the production of peroxides and free radicals, can cause damage to any and all parts of a cell [31]. This is especially important given that a variety of diseases can disrupt the balance of oxygen flow into and around cells, causing improper function of the mitochondria, and thus an increased rate of cell death via apoptosis or necrosis [26].

Mitochondrial dysfunction is a term that is used when there is an impairment in any of these processes. Mitochondrial dysfunction inevitably leads to cellular damage, and it is linked to various diseases and injuries such as Parkinson [32], obesity [33], Alzheimer [34], and cancer [35].

Multiple approaches have been developed to assess mitochondrial dysfunction. For instance, mitochondrial function and dysfunction can be determined with isolated mitochondrial assays such as mitochondrial respiratory control [36]. In an intact cell assay, cell respiratory control can give the rate of ATP production, the proton leak rate, the coupling efficiency, the maximum respiratory rate, the respiratory control ratio, and the spare respiratory capacity [37]. Phosphorus-31 nuclear magnetic resonance spectroscopy can give insights on bioenergetic monitoring *in vivo* by providing an indicator of mitochondrial oxidative phosphorylation [38].

1.3. Optical metabolic imaging

Living tissues can be studied using optical imaging. A wide range of optical imaging techniques can be utilized to visualize tissue morphologies or to assess metabolic processes [39]. Optical imaging techniques provide quantitative physiological and structural information reflecting disease progression. Furthermore, these techniques have been shown to possess high sensitivity and specificity for discriminating between diseased and healthy tissue [40]. Among optical imaging systems, fluorescence imaging techniques provide the capability of monitoring the metabolic state of cells, tissue, and organ through probing the intrinsic or exogenous fluorophores. Optical metabolic imaging can be classified into three main categories [41]:

Auto-fluorescence imaging of redox ratios. Imaging intrinsic fluorophores (auto-fluorescence signals) of tissue provide information about the status of cellular bioenergetics in

different tissue types [42-44]. This approach quantifies mitochondrial redox state by imaging reduced nicotinamide adenine dinucleotide (NADH) and oxidized flavin adenine dinucleotide (FAD), two key Krebs cycle coenzymes in mitochondria. NADH and FAD fluorescence signals can be captured without the use of exogenous fluorescent dyes. Studies conducted by other researchers as well as our team show that the ratio of these fluorophores, (NADH/FAD), the redox ratio, acts as a quantitative marker of the tissue metabolism in injury due to ischemia-reperfusion [42, 44-48], hyperoxia[49], diabetes [50], gene knockout [43, 51-54], and also as indicators for the response of different treatments such as photodynamic therapy [55], cancer therapy [56-58], and mitigating radiation-induced injuries [59].

Fluorescence imaging of exogenous markers. By Imaging exogenous fluorophores, the mitochondrial ROS production rate, which is correlated with OS, can be monitored. Using fluorescence time-lapse microscopy, the dynamics of oxidative stress concentration in injuries can be quantified *in vitro*. Also, the new methodology and experimental protocol can quantify the changes in oxidative stress because of different stress conditions in an uncoupled or inhibited state of cells. This approach studies the metabolic activity preferences under different metabolic stressors such as hypoxia or high glucose condition.

Oxygenation imaging. Tissue oxygen consumption correlates with cytochrome oxidase in the tissues. Therefore, whole-body respiration can be correlated with the overall rate of mitochondrial electron transport. However, the inference of mitochondrial dysfunction from changes in oxygen consumption is difficult due to the complexity of whole organisms and tissues. Therefore, without having another source of information, a dysfunction in the supply of substrates or the consumption of ATP in the tissues may not show mitochondrial dysfunction [37]. However, optical absorption provides the contrast for functional imaging since it provides information on

12

the oxygen saturation of hemoglobin. Near-infrared spectroscopy (NIRS) by utilizing the light in the near-infrared window (700-1300nm), can determine the *in vivo* concentrations of chromophores, noninvasively. The oxygen consumption and hemodynamics of skeletal muscles can be monitored by NIRS in various diseases [60-62]. As a side-project, NIRS is applied to monitor the muscle oxygenation of patients with postural orthostatic tachycardia syndrome (POTS) [63].

1.4. Animal injury models

The animal injury models that are studied here include the followings.

Diabetic wound and photobiomodulation (PBM). Chronic lower-extremity ulcers are a common complication of diabetes, and approximately 15% to 25% of individuals diagnosed with diabetes will develop a lower extremity ulcer at some point in their lifetime [64]. Moreover, diabetic ulcers often persist for months to years in debilitated patients [65-67]. These ulcers can become infected causing pain, discomfort, hospitalizations, and poor quality of life, which impose a tremendous economic burden on the healthcare system with costs conservatively estimated for the management of diabetic foot ulcers to be $9–$13 billion in the United States [68]. This increases a secondary demand; a need to be able to monitor and track the cellular changes during the wound healing trajectory, so that effective interventions can be identified and implemented during the early stages benefiting the patient population [69].

PBM using far-red (FR) to near-infrared (NIR) light is a non-invasive, painless, and inexpensive therapeutic modality with documented efficacy in preclinical and clinical studies in

soft-tissue injuries and wound healing. We studied the excisional wound on the db/db mouse and the progress of wound healing was also monitored after FR-PBM.

Uninephrectomy (UNX). The compensatory hypertrophy of a remaining kidney following unilateral nephrectomy (UNX) and other forms of reduced renal mass is essential to sustain normal kidney functions and for the long-term survival [70]. Compensatory kidney hypertrophy refers to the increase in the size, weight, and functionality of the remaining kidney to restore the lost renal function [71]. The degree to which the remaining kidney can compensate for a reduction in total renal mass is remarkable as seen to occur in many chronic kidney diseases, diabetes, and most dramatically in the kidney of donors for transplantation [72, 73]. The hypertrophic and other adaptive responses of the remaining kidney following a 50% loss of renal mass are adequate to sustain homeostatic responses required for normal function, and kidney donors from transplantation exhibit relatively low risk of end-stage renal disease [74]. However, it is also evident that the loss of a kidney may reduce the overall margin of safety when faced chronically with excess solute or electrolyte loads and accelerate the progression of chronic kidney disease [75]. Although the long-term clinical impact of UNX and renal hypertrophy may be debated, the rapid hypertrophic response during the first several days following UNX is critical to prevent the immediate consequences of acute kidney failure and for the survival. However, the mechanistic basis of these rapid compensatory responses remains poorly understood. It is unclear what signals the remaining kidney to hypertrophy [70]. The goal of the present study was to determine whether renal oxidative stress may be important in this signaling process.

Partial body irradiation and mitigating by lisinopril. The Ionizing radiation induces cell death mainly by DNA damage, making it a useful therapy to treat tumors. However, organ damage to non-tumor (normal tissue) can also occur by radiation. The gut, bone marrow, skin, lung, and

14

kidney are acutely injured by radiation, though damage to each system is dependent on the time after exposure and the dose of radiation. The gut and bone marrow manifest injury within days after radiation, while renal failure takes months to develop. However, after the bone marrow, the kidney is one of the most radiosensitive organs manifesting effects from doses as low as 6 Gy and up. Therefore, the kidney could exhibit injuries in cancer survivors undergoing radiotherapy [76-78]. Furthermore, exposure to high doses of radiation from a radiological terrorist attack or nuclear accident will injure the kidney and cause renal dysfunction [79, 80]. As the effects of radiation on the kidneys can be life-threatening, the assessment of the mechanism of injury and the development of medical countermeasures to treat the effects of irradiation become increasingly essential.

Late renal dysfunction after irradiation is mainly attributed to radiation-induced nephropathy, which is characterized by a slow progressive reduction of renal function, and its clinical symptoms such as increased serum creatinine levels, proteinuria, azotemia, anemia and high blood pressure [77, 81]. It is well-known that irradiation at higher doses may attenuate renal hemodynamics, which contributes importantly to elevated levels of reactive oxygen species (ROS), glomerulosclerosis, tubulointerstitial fibrosis, and renal dysfunction [82, 83].

A rat model of one leg-out partial body irradiation (PBI) (i.e., shielding one hind leg) has been previously described [84]. The whole animal model is developed to study the effects of radiation in the context of exposures of multiple organs that are injured at different times. This model spares enough bone marrow to repopulate the hematopoietic system but not the other organs. Our studies revealed that angiotensin-converting enzyme (ACE) inhibitors such as enalapril, captopril, fosinopril, and lisinopril abrogated the radiation-induced injuries and renal toxicity[84, 85]. Moreover, ACE inhibitors, particularly lisinopril, demonstrated significant

protection in cancer patients[86, 87]. Our team has shown that combining lisinopril with hydration and antibiotics provides optimum mitigation of acute and delayed radiation injuries in multiple organs after a single dose of 13 Gy[85]. There was a 100% morbidity rate in rats exposed to 13 Gy by 160 days, while the morbidity was only 20% in animals treated with lisinopril with saline and Enrofloxacin with G-CSF at the same time after irradiation.

Whole thoracic irradiated heart exposed to ischemia reperfusion. Radiation The two main causes of death in the United States are heart disease and cancer [2]. Studies have shown that the two may be interconnected in radiotherapy during the treatment of intrathoracic malignancies [88]. Indeed, radiation is an independent risk factor for death from cardiovascular disease in cancer patients after prolonged thoracic radiotherapy [88]. Insofar as cardiomyocytes are well-differentiated and nonproliferating cells, the heart is perceived as relatively radiation-resistant as compared to other tissues, such as bone marrow, gut, or lungs [89, 90]. Therefore, it has been suggested that radiation damage to the heart is primarily caused by inflammatory changes in the microvasculature with a reduced number of capillaries, leading to occlusion of vessels, reduced vascular density, perfusion defects, and eventually, myocardial ischemia, cell death, and fibrosis [91-94]. The manifestation of cardiovascular disease is more likely to occur with a high dose and a long-time exposure to irradiation; hence, the potential for short-term low-dose irradiation-induced injuries is less likely to occur in the heart. Evidence indicates that there are compelling associations between high therapeutic doses of thoracic radiation and increased risks for cardiovascular disease in long-term cancer survivors [95-98].

In the present study, we investigated the impact of a single low dose 15Gy WTI on the mitochondrial function before, during, and after global ex vivo IR injury. Our aims were: (a) to determine whether WTI predisposes the myocardium to worsened outcome following IR injury

and (b) whether altered mitochondria metabolism, specifically redox state, is a key contributor to WTI aggravated IR injury.

Ischemia-reperfusion injury in liver. End-stage liver disease is a leading cause of death in the USA. Liver transplantation (LT) is the only cure, but liver organs qualified for LT are in shortage. One of the reasons for this shortage is ischemia and reperfusion injury (IRI), which has a significant negative impact on organ functionality. IRI occurs both during hepatic surgery with clamping of the vascular pedicle of the porta hepatis (Pringle maneuver) and in LT [99]. Hepatic IRI has a profound clinical impact on graft function after LT with organs from marginal or extended criteria donors because its deleterious effects are augmented in these grafts. IRI causes early organ failure in up to 12% of patients, and 15% to 25% of patients experience long-term graft dysfunction [100]. Post-reperfusion syndrome, with an incidence rate of up to 30%, causes acute cardiovascular collapse that could lead to patient death [101]. Poor graft function after LT contributes to the need for a retransplantation of the liver and results in an increase in resource utilization. In the present study, we investigated the mitochondrial redox state of livers before, during, and after global IRI.

Hyperglycemia in retina endothelial cells. Increased oxidative stress and mitochondrial dysfunction have been linked to the development and progression of diabetic retinopathy and trigger the pro-apoptotic actions of mitochondria [102, 103]. Specifically, oxidative stress plays a key role in retinal vascular cell injury and degeneration of capillaries during diabetes [103]. However, little is known about the primary retinal vascular cell target and the mechanism(s) involved in metabolic stress associated with diabetes and pathogenesis of diabetic retinopathy.

The distribution of vascular pericytes (PC) and endothelial cells (EC) reflect specific functional features of the microvasculature in different organs and relate to the organ metabolic demand and

17

specialized cellular functions. The greatest PC density has been noted in the retinal blood vessels, which is needed for the particularly high metabolic activity of the retina and requires meticulously regulated blood flow. The greater pericyte number and coverage has been linked to higher capillary and venular blood flow and better microvascular barrier. Due to the important role of retinal pericytes (RPCs) in controlling blood flow, a higher sensitivity to metabolic changes is expected for these cells compared with retinal endothelial cells (RECs), especially under stress conditions. We previously showed that RPCs are more sensitive to the adverse effects of high glucose compared with RECs [104, 105]. However, the reason for this selective sensitivity remains unknown. We proposed this sensitivity may be linked to a preference of bioenergetic sources for these cells.

Here, we measured the metabolic resistivity of the RPC and REC by monitoring reactive oxygen species (ROS) production in real-time, while the live cells were challenged with various metabolic stressors. Stress conditions were induced by a mitochondrial uncoupler or inhibitors of electron transport chain (ETC) complexes affecting the oxidative metabolic pathway. Moreover, the metabolic stress was exacerbated by HG condition to gain insight into the underlying cause of RPC sensitivity to HG. Using time-lapse microscopy, an experimental protocol was previously designed to quantify the dynamics of ROS production in vitro [40, 106]. In this protocol, the nano-molar concentration of MitoSOX red was used to monitor mitochondrial ROS production levels and the rate in live cells over time. Using this experimental protocol, the dynamics of ROS production in REC and RPC were determined. Live cells were incubated with PCP (a mitochondrial uncoupler) or rotenone and antimycin A (mitochondrial ETC inhibitors) under normal glucose (NG). Furthermore, the mitochondrial stress from PCP treatment was compared under HG.

Hypoxia in pulmonary artery endothelial cells. Hypoxia is severe oxygen stress, which mostly causes irreversible injury in lung cells. However, in some studies, it is reported that hypoxia decreases the severity of injuries. This study assessed the effect of the oxygen tension on fetal pulmonary artery endothelial cells (FPAECs).

Chapter 2

Fluorescence Metabolic Imaging

2. Fluorescence metabolic imaging

2.1. *In vivo* fluorescence imaging of diabetic wounds

The objective of this project is to examine the correlation of mitochondrial metabolism to the delayed wound healing in diabetic mice by developing a surface fluorescence imaging instrument. Diabetes is known to cause delayed wound healing, and extremity diabetic ulcers may end with lower limb amputations and mortalities. It is expected that diabetes can alter the spatiotemporal distribution of the mitochondrial redox state of wounds. Using surface fluorescence imaging, we monitored mitochondrial redox state, i.e., reduced nicotinamide adenine dinucleotide (NADH), oxidized flavin adenine dinucleotide (FAD), in the *in vivo* diabetic wounds. What follows is a brief description of wound induction and experimental protocol, the explanation of surface fluorescence imager, and signal processing along with the results.

2.1.1. Experimental protocols

The experiments conducted were approved by the Institutional Animal Care and Use Committee (IACUC) at the University of Wisconsin Milwaukee. Genetically diabetic male ~20-week old mice (db/db; BKS.Cg-m+/+ Leprdb) were obtained from Jackson Laboratories (Bar Harbor, ME). The blood glucose level and the weight of the mice were measured. Mice were anesthetized with 4% isoflurane. A 10mm circular full-thickness wound was prepared midline at the shoulder-level. Age-matched non-diabetic mice were used as controls (n=6/group).

In vivo images of metabolic indices (NADH and FAD) were captured just after wound induction. For the assessment of wound healing progress, the wounds also imaged at the 2nd, 4th, and 6th day of post-wounding. At the end of the experimental protocol, mice were euthanized,

wound biopsies were collected and snap-frozen in liquid nitrogen for later 3D cryo-imaging of the volumetric mitochondrial redox state. Table 1 shows the experimental protocol timeline. Biopsies from the two groups of mice (n=4/group) were collected right after wound induction.

For studying the effect of FR-PBM, db/db mice were randomly assigned to 670 nm PBM or sham treatment groups. Treatment consisted of irradiation of the wound using a 670 nm LED array (Quantum Devices, Barneveld. WI) to deliver a light dose of 4.5 J/cm2 at the wound surface (60 mW/cm2 for 90 sec) five times per week. The 670nm LED array was positioned directly over the wound area at a distance of 1 cm. Sham-treated mice had the LED array positioned above the wound for 90 seconds, but not illuminated. *In vivo* fluorescence imaging was performed at day 0, 3, 6, and 9 post-wounding (n=6 FR-PBM, n=5 Sham-treated). The imaging procedure takes around 5 min, and during this time, all the animals are kept anesthetized. This anesthetic stage keeps the animals' movement in minimum during the imaging. At the end of the experimental protocol, the entire wounds were excised and snapped frozen immediately. The frozen biopsies were then imaged by cryo-imaging for the volumetric redox study.

2.1.2. Instrumentation

Figure 2 illustrates a schematic view of the costume-designed surface fluorescence imager. This system can record the online and real-time fluorescence images of tissues using a charge-coupled camera (QImaging, Rolera EM-C^2, 14 bit) with 1,004×1,002 pixel arrays. A mercury arc lamp (Intensilight, Nikon, Tokyo, Japan) generates the excitation light through a liquid light guide. For each channel, the light spectrum is filtered by optical filters at selected wavelengths to excite the specific fluorophores from the surface of the wounds. For mitochondrial redox
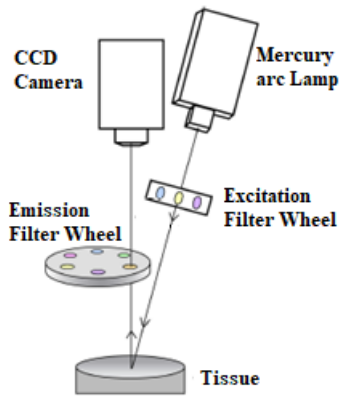
Figure 2: A schematic view of in vivo fluorescence imager. Specific filter set is chosen at excitation and emission wavelength of NADH and FAD.

experiments, we set the excitation filter for NADH at 350 nm (80-nm bandwidth, UV Pass Blacklite, HD Dichroic, Los Angeles, CA). The FAD excitation filter was set at 437 nm (20-nm bandwidth, 440QV21, Omega Optical, Brattleboro, VT). NADH and FAD emission filters are set at 460 nm (50-nm bandwidth, D460/50M, Chroma, Bellows Falls, VT) and 537 nm (50-nm bandwidth, QMAX EM 510-560, Omega Optical), respectively. Two neutral density filters (ThorLabs, NJ) are used as excitation and emission filters for white field channel imaging. The appropriate excitation and emission filters are selected using two motorized filter wheels (FW103H, ThorLabs, NJ), which is controlled by a two-channel APT™ benchtop stepper motor controller (BSC202, ThorLabs, NJ).

2.1.3. Image processing

NADH and FAD autofluorescence images of wounds were analyzed using MATLAB. The images of two cuvettes containing 50µM NADH and 0.5µM FAD solutions from their respective channels were used for calibration. The calibration performed to minimize day-to-day variations in light intensity. The wound border was found manually using the white field image, and then the wound segmented for both NADH and FAD images. The ratio of these two images (NADH/FAD)

23

was calculated pixel-by-pixel. Subsequently, the mean of redox ratio histograms was considered as the quantitative marker and calculated according to Eq. (1):

$$RR = \frac{1}{N}\sum (wound\ pixels)$$

(1)

where N is the number of wound pixels.

2.1.4. Results

Figure 3 shows the on-line fluorescence redox ratio images of diabetic wound vs. control during the first six days of wound healing. Table 1 shows a statistical analysis of all the redox ratios calculated based on Eq. 1. Comparing diabetic mouse to control, lower NADH and higher FAD fluorescence signals were observed throughout the wound resulting in a dropped redox ratio value (oxidized state) over time. At the end of day 4 of wound healing, the surface redox ratio of the diabetic wound had a 61% lower state (oxidation of ETC) compared to control.
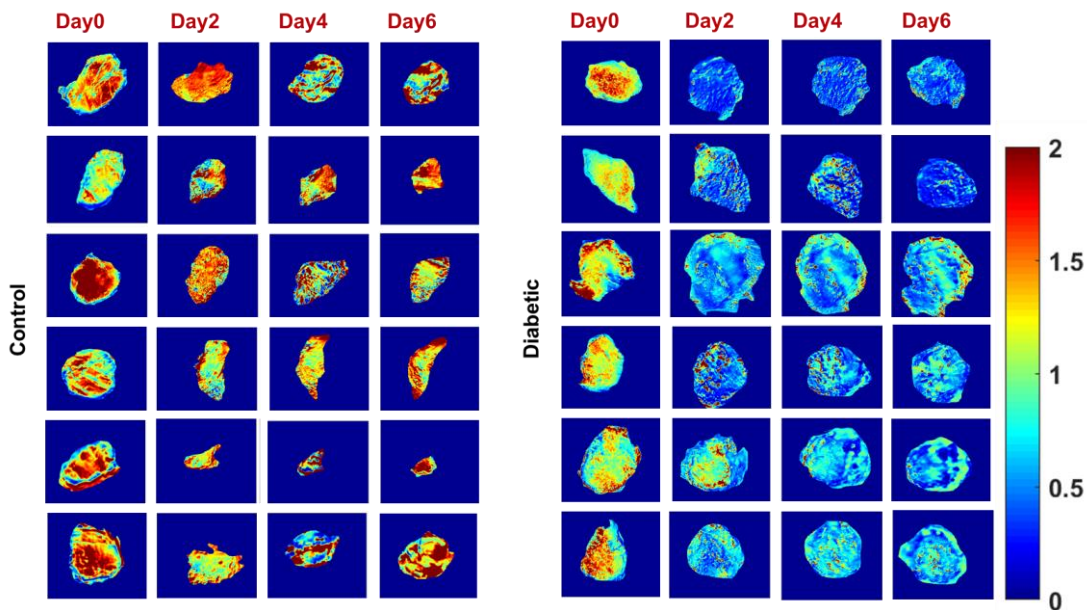
Figure 3: Real-time metabolic images of the wounds from all diabetic and control mice. *In diabetic mice, a decrease in redox ratio and an increase in size of the wounds are observed in comparison with controls over time.*

*Table 1: A comparison of image quantifications over days Diabetic versus Control. Surface RR and area of the wounds measured by in vivo fluorescence imager. * significant differences with the control (P<0.05).*

		DAY0	DAY2	DAY4	DAY6
SURFACE RR	**Control**	1.32 ± 0.08	1.37 ± 0.05	1.27 ± 0.06	1.52 ± 0.04
	Diabetic	1.16 ± 0.03	$0.67 \pm 0.06*$	$0.65 \pm 0.03*$	$0.60 \pm 0.06*$
NORMALIZED AREA	**Control**	1	0.61 ± 0.09	0.57 ± 0.09	0.50 ± 0.08
	Diabetic	1	$1.21 \pm 0.05*$	$1.18 \pm 0.03*$	$1.38 \pm 0.06*$

Temporal images from fluorescence imaging of the effect of FR-PBM are shown in Figure 4. It can be conducted that the redox ratio in the FR-PBM wounds is much higher than those of sham-treated mice. This is a consequence of a decrease in the NADH and an increase in the FAD
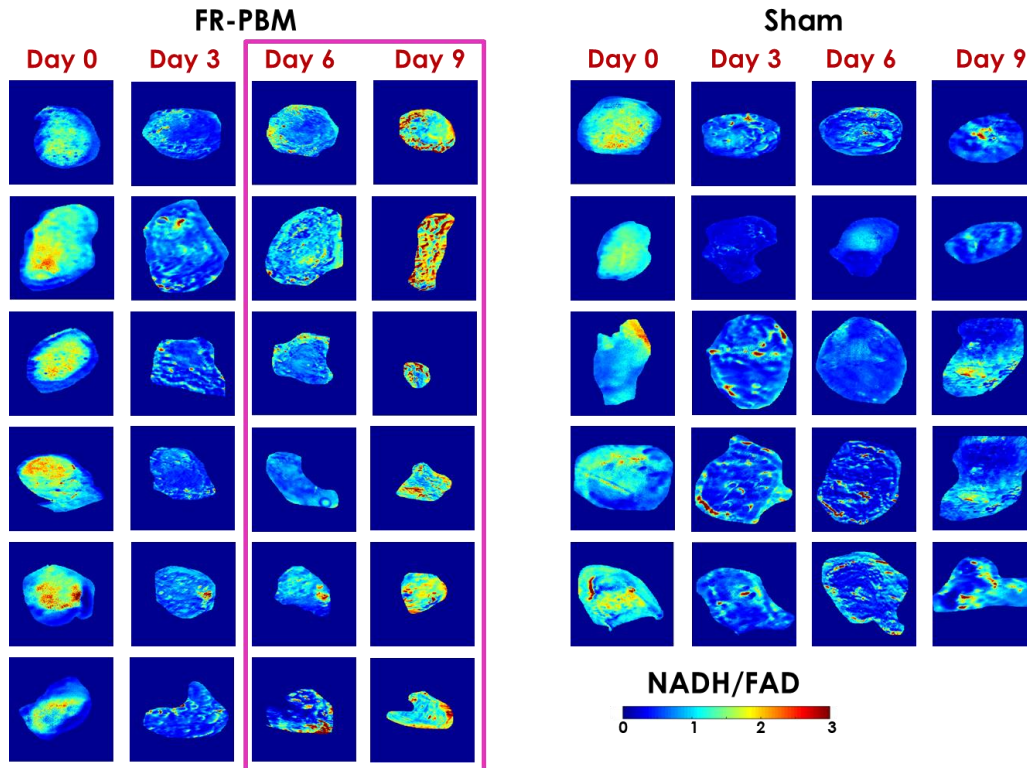
Figure 4: Real-time metabolic images of the wounds from all diabetic sham-treated and FR-PBM mice. FR-PBM caused an increase in redox ratio and a decrease in size of the wounds at day 9 of post wounding.

level of the FR-treated wounds over days, which caused the conspicuous higher redox ratio at days 6 and 9.

Table 2 presents the data and the statistical analysis for FR-PBM and sham-treated groups of mice over days. As it has been previously discussed in methods, Surface RR and wound size are obtained using *in vivo* fluorescence imager, and their corresponding changes over time are called RR change rate and closure rate, respectively. FR-PBM treatment caused a significant increase in Surface RR at days 6 and 9, and the change rate of surface RR became significant at day 9. Therefore, as time passed, the mitochondrial redox state of the wounds in the FR-treated group increased with a faster rate than the Sham-treated group.

In sham-treated diabetic mice, normalized wound size increased from day 0 to day 3 and resulted in a negative closure rate (bigger wound size than day 0). Despite the descending rate of wound size at day 3 and day 9 in sham-treated wounds (positive closure rate), the wound size is still bigger than the wound size at day 0. On the other hand, in the FR-PBM group, the wound

*Table 2: A comparison of image quantifications over days diabetic Sham-treated versus FR-PBM. Surface RR and size of the wounds measured by in vivo fluorescence imager. * significant differences with the control (P<0.05).*

		Day0	Day3	Day6	Day9
Surface RR	FR-PBM	1.01 ± 0.07	0.46 ± 0.03	0.55 ± 0.05*	1.26 ± 0.07*
	Sham	1.08 ± 0.07	0.47 ± 0.05	0.36 ± 0.06	0.67 ± 0.04
RR change rate	FR-PBM	-	-0.54 ± 0.07	0.09 ± 0.05	0.71 ± 0.08*
	Sham	-	-0.61 ± 0.11	-0.05 ± 0.06	0.25 ± 0.04
Normalized wound size	FR-PBM	1	0.87 ± 0.08*	0.82 ± 0.02*	0.61 ± 0.09*
	Sham	1	1.32 ± 0.14	1.26 ± 0.09	1.08 ± 0.11
Closure rate	FR-PBM	-	0.13 ± 0.08*	0.05 ± 0.06	0.21 ± 0.11
	Sham	-	-0.32 ± 0.14	0.06 ± 0.10	0.18 ± 0.11

26

starts to diminish in size from day zero, and it keeps its descending trend to the end of experimental protocol time. The normalized wound sizes in the FR-PBM and sham-treated groups were significantly different on days 3, 6, and 9. The FR-treated wound is 44% smaller than the wound in the diabetic sham-treated group on day 9.

2.2.   3D optical cryo-imaging

The objective of this project is to evaluate the redox state of organs in various models of injuries using fluorescent imaging. Imaging intrinsic fluorophores (autofluorescence signals) of tissue provide information about the status of cellular bioenergetics in different tissue types. Rapid freezing of organs in liquid nitrogen temperatures preserves the metabolic state of the tissue and increases the quantum yield. This approach quantifies mitochondrial redox state by imaging reduced NADH and oxidized FAD, two key Krebs cycle coenzymes in mitochondria. In this section, a brief explanation of the cryo-imager instrument is presented.

2.2.1.   Experimental protocols and tissue preparation

To perform cryo-imaging, tissues are frozen rapidly after extraction form the animal, which results in the preservation of the tissue's metabolic state [107]. Using optical cryo-imaging, I investigated intact rodent organs in the following injury models. All the experiments complied with the standards presented in the Care and Use of Laboratory Animals and were approved by the Institutional Animal Care and Use Committee.

A) **Wound biopsy from db/db mouse.** Transgenic diabetic mice (db/db; BKS.Cg-m+/+ Leprdb) were obtained. A 10mm circular full-thickness wound was prepared midline at the shoulder-level. Age-matched non-diabetic mice were used as controls. For the assessment of

27

healing progress, at the end of the 6th day of post-wound, mice were euthanized, and wound biopsies were collected.

B) **Photobiomodulation (PBM).** The FR-PBM was performed by 670 nm LED arrays engineered to eliminate heat (GaAlAs LED arrays, Quantum Devices, Barneveld WI). db/db mice were randomly assigned to 670 nm PBM or sham treatment groups. Treatment consisted of irradiation of the wound to deliver a light dose of 4.5 J/cm^2 at the wound surface (60 mW/cm^2 for 90 sec) five times per week. The 670nm LED array was positioned directly over the wound area at a distance of 1 -2 cm. Sham-treated mice had the LED array positioned above the wound for 90 seconds, but not illuminated. *In vivo* fluorescence imaging was performed at day 0, 3, 6, and 9 post-wounding (n=6 FR-PBM, n=5 Sham-treated). The imaging procedure takes around 5 min, and during this time, all the animals are kept anesthetized, which minimized movement artifacts during imaging. At the end of the experimental protocol, the entire wounds were excised and snapped frozen immediately. The frozen biopsies were then imaged by cryo-imaging for the volumetric redox study.

C) **Uninephrectomy (UNX).** The effect of unilateral nephrectomy (UNX) on the mitochondrial oxidation state of the remnant kidney was studied in Sprague Dawley (SD) rats. All rats were studied at 6-7 weeks of age. SD rats were obtained from Harlan Sprague Dawley Inc (Madison, WI) and SS rats (SS/JrHsdMcwi) from colonies maintained at the Medical College of Wisconsin (MCW). Rats were fed a custom AIN-76 diet (Dyets, Bethlehem, PA) containing 0.4% NaCl since weaning. Two groups of SD rats were studied: rats with UNX (n=9) of the right kidney, and sham surgery rats in which the same procedures were performed with the right kidney not removed (n=8). All surgeries were performed under isoflurane anesthesia. On day 3 following recovery from UNX or sham surgery, rats were

28

again anesthetized for the rapid removal of the right and left kidneys of the sham rats, and removal of the remaining kidney (left kidney) of the UNX-performed rats. Removed kidneys were hemisected and dropped into a container of isopentane cooled by liquid nitrogen. After 2 min in the cooled isopentane, the kidneys were moved into liquid nitrogen and then stored at -80°C until cryo-imaging was performed.

D) **Partial body irradiated rat kidney and lisinopril treatment.** The non-anesthetized rats were exposed to a total single dose of 13 Gy partial body irradiation (PBI) by shielding part of one hind limb of each rat. The details of the animal model and lisinopril treatment used in this study can be found in our previous report [85, 108, 109]. Briefly, 10 irradiated rats along with 6 age-matched non-irradiated controls were given the antibiotic and hydration post-irradiation. Five of the irradiated rats were randomly chosen to receive further treatment with lisinopril starting one week after irradiation and continued at 24 mg m^{-1} d^{-1} until the tissue was harvested. The kidneys were imaged by optical cryo-imaging to compare the irradiation impact on mitochondrial redox in the three groups of rats; 1) non-irradiated controls (Control, n=6), 2) leg-out partial body irradiated (PBI, n=5), and 3) leg-out partial body irradiated followed by lisinopril treatment (PBI+Lisino, n=5).

E) **Whole thoracic irradiated rat heart exposed to ischemia reperfusion.** Unanesthetized female WAG/RijCmcr (Wistar) rats were irradiated in batches, with a single dose of 15 Gy to the whole thorax only as already described [110]. On day 35 after irradiation, the animals were sacrificed, and the hearts were extracted for ex-vivo Langendorff perfusion. In brief, after cannulating the hearts for retrograde perfusion via the aorta, they were left to stabilize for 25 to 30 mins before initiating the ischemia, ischemia-reperfusion (IR), or time control (TC) perfusion protocol. For the ischemia only group, the hearts were subjected to global

ischemia for 25 min by constricting the retrograde flow through the aortic cannula. The IR groups underwent similar ischemia for 25 min, followed by reperfusion, i.e., removing the aortic constriction, for 60 min. The TC hearts were perfused for the same protocol duration as the IR experiments, without ischemia. The TCs are expected to show no significant difference in redox signal intensity and cardiac function over the entire protocol; thus, validating the reliability of the ex vivo model for evaluating IR-induced damage.

F) **Ischemia reperfusion injury in rat liver.** A total of five groups of Sprague-Dawley (SD) rats containing five per group were studied. The first group consisted of the control (ctrl), which received no treatment. The second group consisted of rats subjected to 60 minutes of ischemia (Isc60), which was achieved by temporarily occluding the blood vessel pedicles to the median and lateral lobes of the liver with a clamp. The third group received treatment like the second group, but with 90 minutes of ischemia injury (Isc90). The fourth and fifth groups had the same ischemia treatments as Isc60 and Isc90, but instead of harvesting the liver after ischemia, the clamp was removed, and the abdomen was closed to allow reperfusion for 24 hours for each ischemia injury group (IRI60 and IRI90). Two different ischemia durations were used to investigate the effect of longer ischemia time, followed by reperfusion injury.

2.2.2. Cryo-imaging system

The custom-built cryo-imager at the Biophotonics Lab, University of Wisconsin Milwaukee, images autofluorescence signals of NADH and FAD at the freezing time, and the redox ratio (NADH/FAD) is calculated from the three-dimensional (3D) image [42, 44]. Freezing, embedding, cryo-imager system (Figure 5), and imaging procedures were previously described in detail [40]. Briefly, the cryo-preserved tissues were first embedded in a customized black mounting medium

1) Lens
2) Stepper Motor
3) CCD Camera
4) Tissue Block
5) Microtome Blade
6) Excitation Filter Wheel
7) Emission Filter Wheel
8) Ultra Low Freezer
9) Excitation Source
10) Power Supply
11) Frame Grabber
12) Data Acquisition System
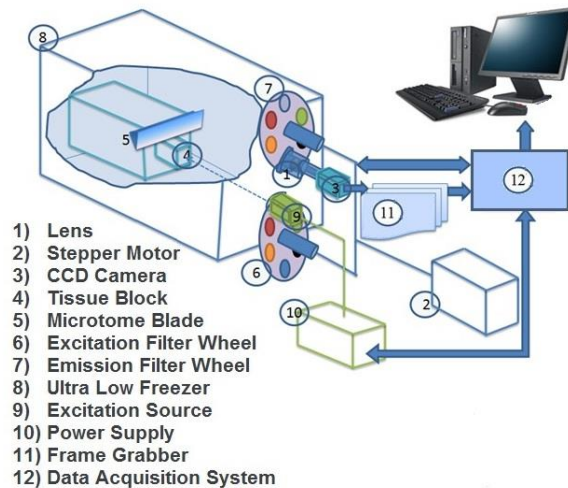
Figure 5: A schematic view of cryo-imager used in this study. All components of the system are labeled.

for imaging and fixed into the cryo-imager system. The system has an automated acquisition system, which sequentially slices the tissue with a microtome blade and acquires separate images of NADH and FAD from the surface of the frozen tissue. A mercury arc lamp (200 W lamp, Oriel, Irvine, CA, with a bulb from Ushio Inc., Japan) was used as the light source. The excitation filter for NADH was set at 350 nm (80-nm bandwidth, UV Pass Blacklite, HD Dichroic, Los Angeles, CA), and the corresponding FAD filter was set at 437 nm (20-nm bandwidth, 440QV21, Omega Optical, Brattleboro, VT). Another set of filters was used to only pass the desired emitted auto-fluorescent signals before reaching the image recordings system (CCD camera, QImaging, Rolera EM-C2, 14 bit). Emission filters for NADH and FAD were set at 460 nm (50-nm bandwidth, D460/50M, Chroma, Bellows Falls, VT) and 537 nm (50-nm bandwidth, QMAX EM 510-560, Omega Optical), respectively. All filters were controlled by two motorized filter wheels (Oriental Motor Vexta Step Motor PK268-01B). The lateral pixel size was 40 µm/pixel, and the z resolution, defined by slice size, was set to 30 µm.

2.2.3. Image processing

A biomarker for the whole organ redox state quantification and visualization is calculated through the following steps. NADH and FAD autofluorescence images are taken from tissue coronal slices and post-processed with an algorithm in MATLAB (MATLAB Inc., Boston, MA). As previously described [42], calibration was performed to minimize the day-to-day variations in light intensity, mirror angle, and non-uniformity of the illuminations pattern. The low-intensity voxels as background and high-intensity voxels as fat tissue were set to zero by thresholding. 3D rendering of the redox ratio (NADH/FAD) for all kidneys were calculated voxel-by-voxel. Subsequently, the histograms of the redox ratio, which is a distribution of pixel intensities through the whole volume, were calculated. The corresponding mean values of the whole sample histograms were calculated according to the following equation,

$$mean\_whole = \frac{1}{N}\sum(whole\ kidney\ voxels),$$

(2)

where N is the number of voxels within the organ. The mean redox ratio values of the histograms can be used for quantitative analyses of metabolic states.

Medullary and cortical redox ratio quantification. The objective of my research is to quantify the 3D heterogeneity and spatial distribution of the redox state in different organs using an image processing tool. It is expected that injuries can alter the metabolic heterogeneity and the distribution of mitochondrial redox state. For example, the kidney medullary region can respond differently to injuries comparing to the cortex. 3D cryo-images can also give an anatomical distribution of the mitochondrial redox state throughout the organ. My 3D image processing algorithm allows the segmentation of medullary and cortical regions in redox cryo-images. The developed image processing tool also can quantify the spatial distribution and correlation of the regional mitochondrial redox state to the various renal injury models.

32
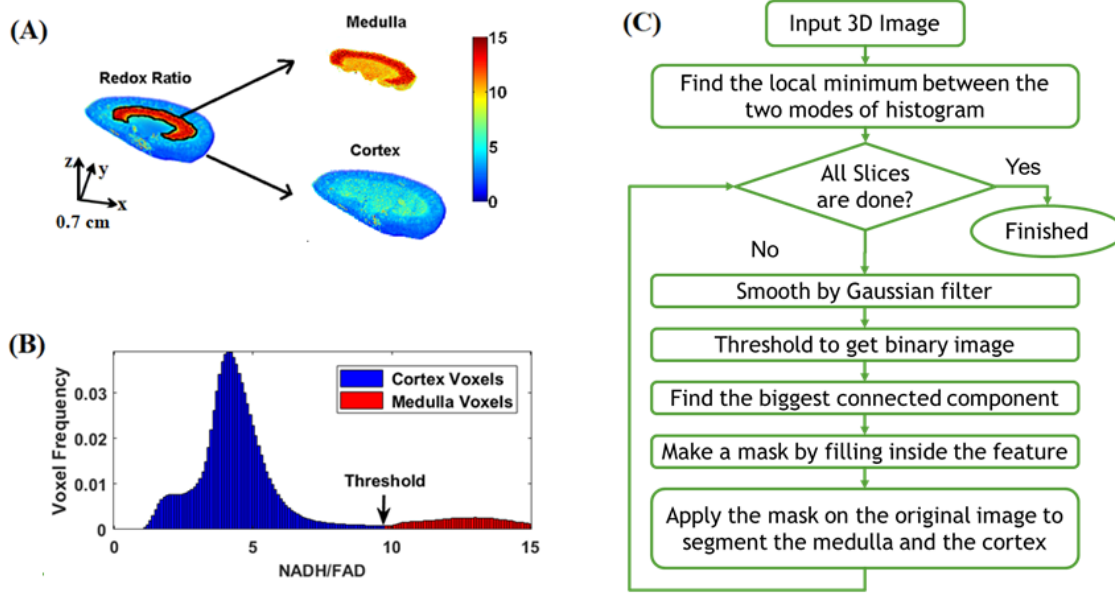
Figure 6: Medullary and cortical segmentation. *(A) a whole kidney redox ratio image (the black line shows the segmentation boundary), the segmented approximate medulla, and the rest of the kidney (approximately cortex). (B) 3D volumetric histogram of the whole kidney in part. The local minimum between approximate cortex and medulla voxels. (C) A simplified flowchart for the segmentation algorithm.*

As shown in Figure 6A, the histograms of images from kidneys were bimodal, i.e., there were two regions of a kidney with different levels of redox ratios. The two modes in the histogram are distinguished by two different colors in Figure 6B. While most of the ATP produced by the kidney, particularly in the cortex, is through aerobic mechanisms[111, 112], the medulla can efficiently use anaerobic metabolism [113]. Therefore, it can be approximated that the second mode in bimodal histograms showing a high redox ratio corresponds to the renal medulla, while the first mode with a low redox ratio corresponds to the renal cortex.

The kidney was segmented into its medullary and cortical regions to analyze the heterogeneity of redox ratio regionally, as shown in Figure 6A. The algorithm for segmenting approximate medullary and cortical regions is shown in Figure 6C. After loading the stack of grey-scale redox images, a 5×5 Gaussian filter was applied to each slice of images as a low pass filter to reduce machine-induced artifacts and noise, while improving the global thresholding. Then, the

33

smoothed image was converted to a binary image by selecting an appropriate threshold. The local minimum between the two modes of histograms was considered for thresholding, as shown in Figure 6C. Then, the largest connected component (i.e., the largest object) was found in the binary image since the medullary region is the largest high-intensity object in the redox image. This component was used as a mask for the medullary section. By filling the mask, we are assured that inside the component is also detected as the medulla. The remaining pixels correspond to the cortical and papillary regions. The papilla was visually segmented and masked to have a better approximation of the cortex. The process was repeated for every 2D image to form the 3D redox ratio for approximating both the medulla and the cortex. The same mask for segmentation was used to analyze NADH and FAD images separately.

The corresponding mean values of the whole kidney, medulla, and cortex histograms were calculated according to equations

$$mean\_cortex = \frac{1}{N_c}\sum(segmented\ cortex\ voxels),$$ (3a)

$$mean\_medulla = \frac{1}{N_m}\sum(segmented\ medulla\ voxels),$$ (3b)

where N_c and N_m are the numbers of voxels within the segmented cortex, and medulla, respectively. The mean redox ratio values of the histograms can be used for quantitative analyses of metabolic states of the cortical (Eq. 3a) and medullary (Eq. 3b) regions.

2.2.4. Results

A) Diabetic wound biopsy on mouse: Figure 7A shows 3D rendered metabolic images (NADH, FAD, and redox ratio) obtained from diabetic wound and control at the end of the experimental protocol. Figure 7B shows the histogram comparison of the redox ratio 3D images. The mean
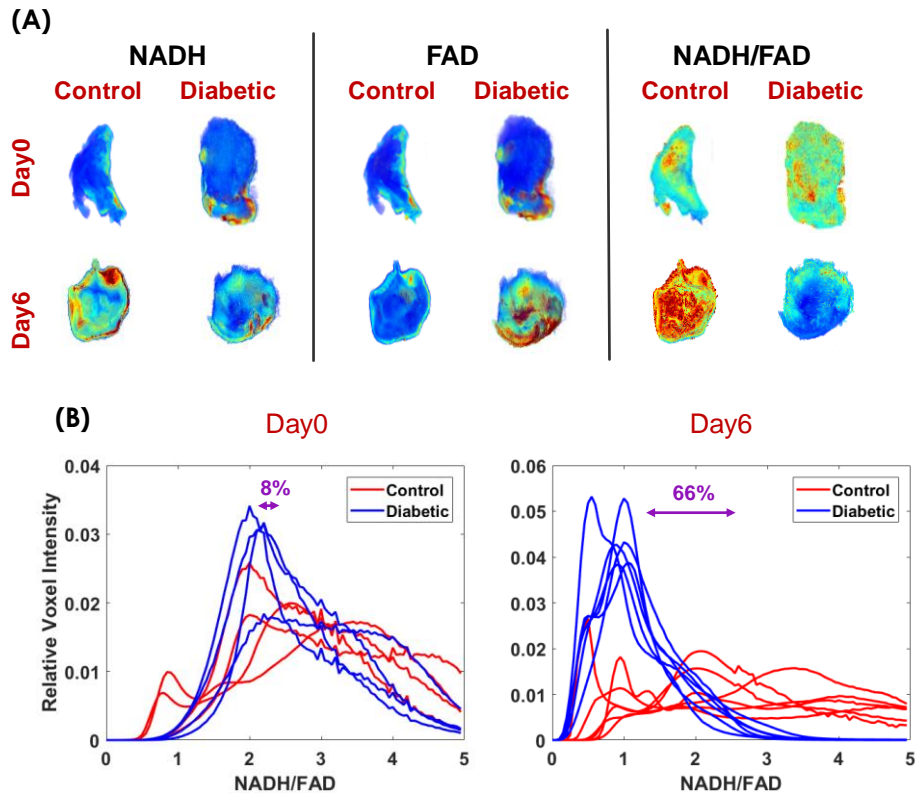
Figure 7: A comparison on redox ratio of diabetic versus control wound biopsy. *A) 3D cryo-images of representative biopsy wounds from diabetic vs. controls at day0 and day6 of post punching, B) their corresponding tissue redox ratio (NADH/ FAD) histograms. The percentage difference between the mean value of histograms (Volumetric RR) from control vs diabetic is shown for each day of post punching.*

redox ratios calculated according to Eq. (2) to display the redox state of biopsy wounds at day 4 of wound induction, shown in the legend of Figure 7B. Complying with the trend we observed with the in vivo fluorescence imager, at the end of the experimental protocol, the diabetic mouse had a %114 lower volumetric redox ratio (oxidized state) comparing to control, lower NADH and higher FAD fluorescence signals.

Figure 8a represents 3D rendered cryo-images captured from the biopsies collected at day 0 and at the end of the experimental protocol for studying FR-PBM. The color-coded images of wound biopsies show higher NADH and lower FAD in the FR-treated group in comparison with the sham-treated group resulting in a higher intensity of volumetric redox ratio images. Figure 8b indicates that on day 9, the volumetric redox ratio histograms were shifted to the right by 46% on average
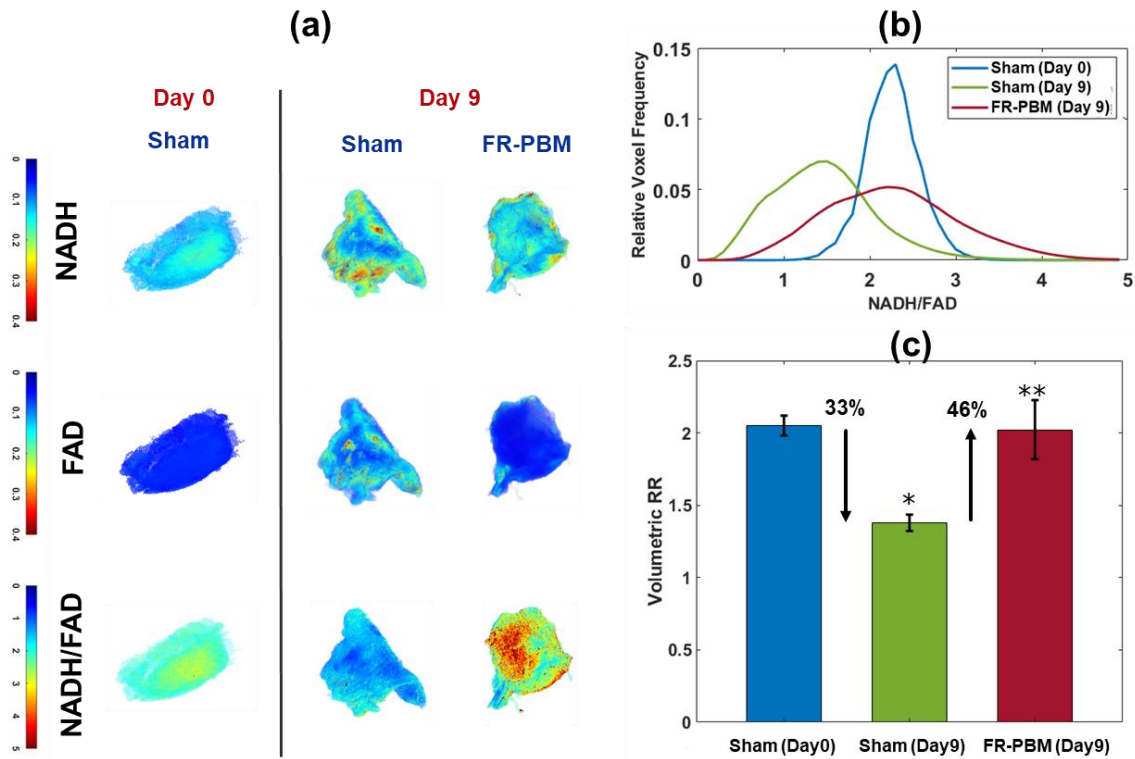
Figure 8: A comparison on redox ratio of diabetic Sham-treated versus FR-treated wound biopsy. a) Representative fluorescence cryo-images of NADH, FAD, and the tissue redox ratio (NADH/FAD) for representative wounds are shown at day 9 and day 0 (b) The redox ratio histogram of the wounds on the FR-PBM and sham-treated group of mice is also shown. (c) the bar plot illustrates the statistical analysis of volumetric RR.

in the FR-PBM group when compared to the sham-treated. The difference in mean volumetric RR ± standard error is also shown in Figure 8c. The Volumetric RR drops at day 9 of post wounding in sham-treated mice when compared to the sham-treated mice at day 0. When comparing the FR-PBM group with the sham-treated group on day 9, there is a significant difference (P<0.05). This observation confirms the data that was obtained from the *in vivo* fluorescence imager.

B) Uninephrectomy: Figure 9A shows the 3D rendered NADH, FAD, and NADH/FAD redox ratio (RR) images of right and left kidneys obtained from a single representative normal Sprague Dawley (SD) rat in which the right kidney was removed (UNX) and a single SD rat in which a sham surgery was performed (Sham). As it can be seen in pseudo color representation, the left
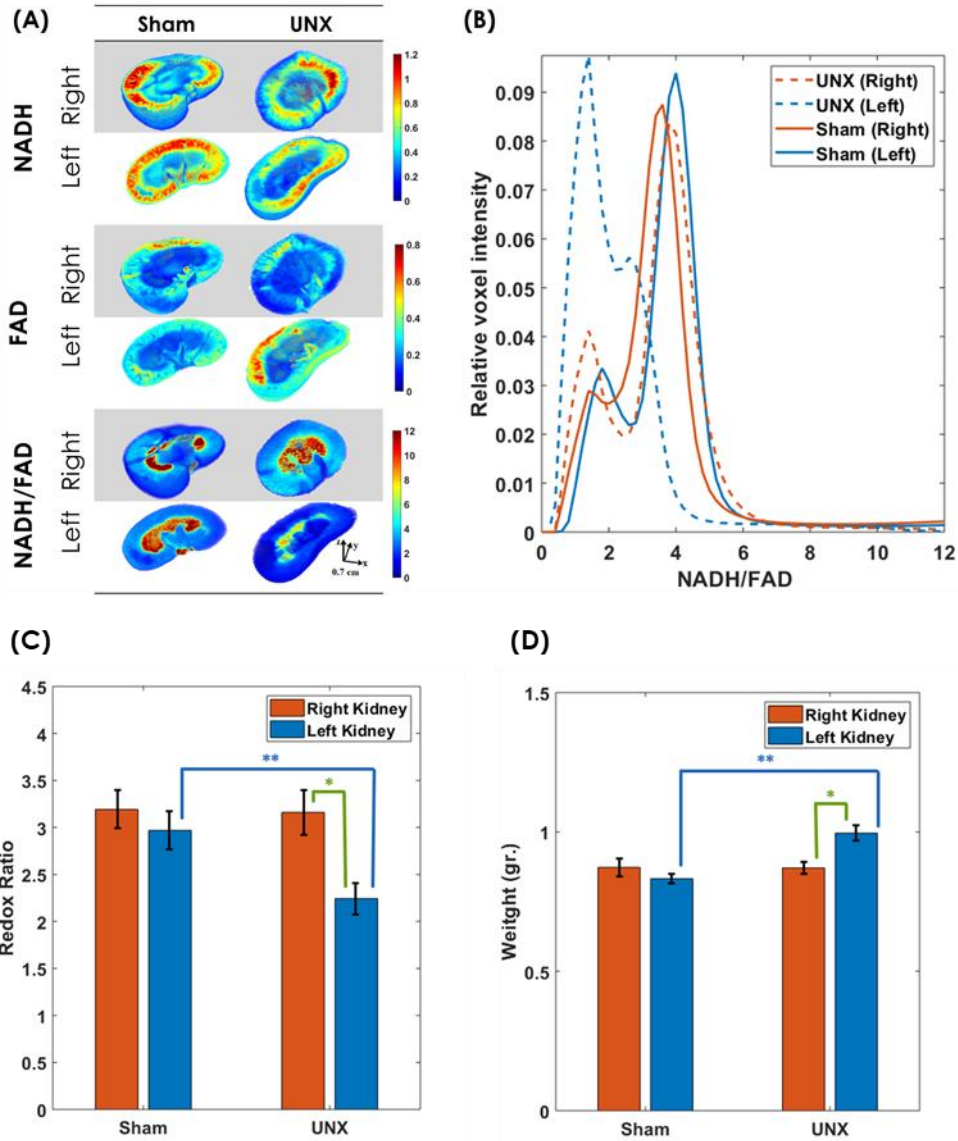
Figure 9: The effect of uninephrectomy (UNX) on the volumetric redox ratio. *(A) Representative 3-dimensional rendered images of kidneys from each treatment: UNX, and Sham. The fluorescence patterns for the redox ratio (NADH/FAD) of the whole kidney, medullary and cortical regions are shown. The corresponding intensity histogram distributions of the whole kidney (B), medullary (C), and cortical (D) redox ratios are illustrated.*

kidney in UNX exhibit a lower RR value, indicating that UNX caused an oxidized redox state within the medullary and cortical regions. Figure 9B shows the distribution of the redox ratio integrated throughout the ½ kidney calculated from the same four (½) kidneys shown in Figure 9A. The distribution of redox ratio is lower in the left kidneys of UNX rat compared to sham, while the histograms of the right kidneys exhibit similar distributions of the redox ratio.

Figure 9C summarizes the mean ± standard error of the RR calculated from the kidneys of SD rats 3 days following UNX and compared to Sham rats. It was found that the average RR of the remaining left kidney of SD rats was reduced by 29% compared to the right kidneys of these same rats that had removed 3 days earlier (P<0.01). A similar reduction of RR was observed averaging 24% (P<0.05) when the remaining left kidney was compared to the left kidney of the sham-operated rats removed 3 days following sham surgery. No significant difference was observed between the right and left kidneys of sham rats (P>0.05), neither between the right kidneys of the two groups (P> 0.05).

The mean ± standard error kidney weights of the rats summarized in Figure 9D found that UNX resulted in a 14% increase in the left kidney weight compared to the right kidneys (P<0.01). Similarly, there was a significant weight increase (20%, P<0.01) of the remaining kidney after UNX compared to the left kidneys of the sham-operated SD rats. No significant differences were observed comparing weights of the left and right kidneys of the sham rats (4%, P>0.05) neither when comparing the right kidneys of the two groups (P>0.05).

C) PBI rat kidney: Representative examples of 3D cryo-images of the NADH and FAD fluorescence signals and their redox ratios (NADH/FAD) obtained from control rats, partial body irradiated (PBI) rats, and rats treated with lisinopril after PBI (PBI+lisino) are shown in Figure 10A. The medullary and cortical regions segmented from the same three representative kidneys are shown in Figure 10B and Figure 10C, respectively. Figure 10D, Figure 10E, and Figure 10F show the corresponding redox ratio histograms of the same three representative kidneys from each group shown in Figure 10A, Figure 10B, and Figure 10C, respectively. Comparing PBI rats to controls, lower NADH and higher FAD fluorescence signals were observed throughout the kidney as shown in Figure 10A, especially in renal medullary regions. Notably, when the PBI rats were
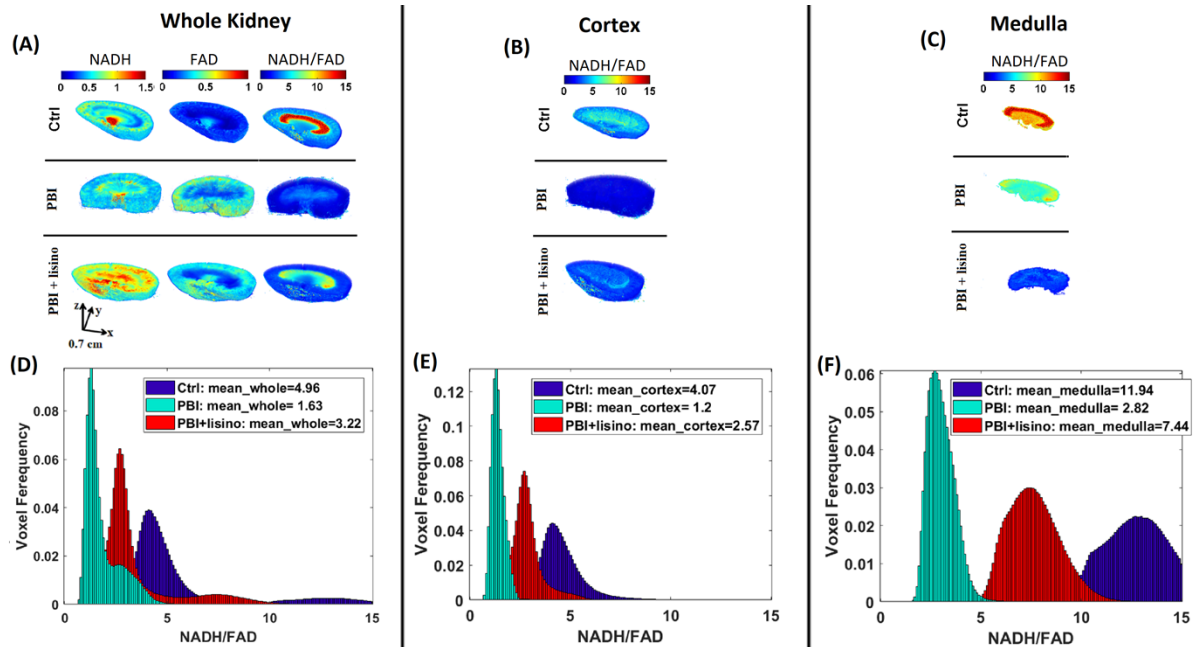
Figure 10: The effect of partial body irradiation (PBI) on the whole kidney, medullary and cortical redox ratio. (A) Representative three-dimensional rendered images of kidneys from each treatment: Non-irradiated (Control), Partial Body Irradiated without (PBI) and with lisinopril treatment (PBI+lisino). The fluorescence patterns for NADH, FAD, and the tissue redox ratio (NADH/FAD) are shown. (B) The 3D segmented cortical regions for each treatment and (C) the medullary regions for each treatment. (D), (E), and (F) are the corresponding intensity histogram distributions of the whole kidney, cortical, and medullary redox ratio, respectively.

treated with lisinopril after radiation, the kidneys exhibited higher levels of redox ratios, i.e., reduced redox state, throughout the kidney compared with those of PBI alone treated animals.

D) WTI heart exposed to IR: Figure 11(a) shows representative 3-D cryo-images obtained from the different treatment groups (TCnon, TCirr, ISCnon ISCirr, IRnon, IRirr). Representative 3-D rendered RRs from each group are also shown. A difference in the 3-D rendered images can be observed in the different experimental conditions (TC, ISC, and IR); there was no significant difference in the RR between nonirradiated and irradiated hearts under similar experimental conditions. This observation is suggesting that the RRs increased during ischemia and decreased during reperfusion when compared to their respective TCs. The individual representative images for the RR distributions are summarized in the histograms in Figure 11(b). The weighted mean value calculated using Eq. (2) is shown in the plot legend. A high mean value of RR suggests a
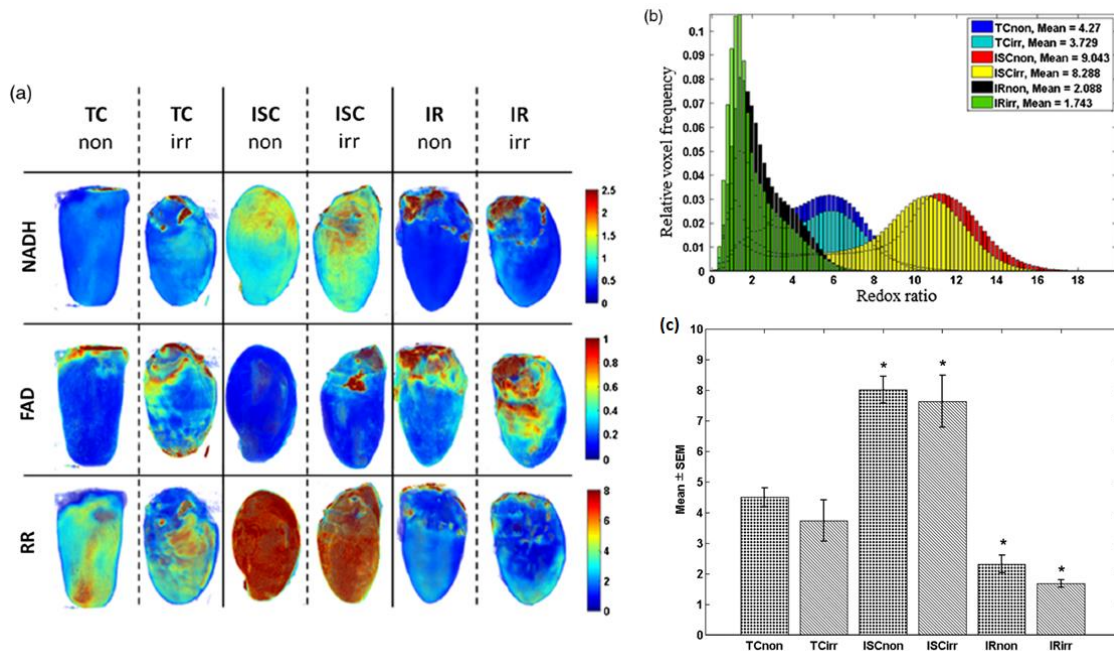
Figure 11: The effect of whole thoracic irradiation on hearts exposed to ischemia reperfusion. *a) Cryo-imaging results of representative hearts in each group. (a) 3-D fluorescent images of NADH, FAD, and RR. (b) Corresponding histograms of voxel distribution of the RR fluorescent images. (c) Bar plot of mean for volumetric histograms showing statistical analysis (n = 5/group). * shows the group that are significantly different from their respective TCs.*

reduced redox state of mitochondria, and a low value suggests an oxidized redox state of mitochondria. Figure 11(c) shows a summary bar plot of the mean ± SEM of cryo-imaging RR for each treatment group. There was a significant difference in RR ($p < 0.05$) between TC and ISC or IR for the irradiated and nonirradiated hearts when compared to their TCs. For nonirradiated and irradiated hearts, ischemia increased RR 78% and 105%, respectively, whereas IR decreased RR by 42% and 55%, respectively. Thus, there was no significant difference in the RR between the two groups.

E) IR injury in rat liver: Figure 12a shows redox ratio cryo-imaging results for all the samples in each group. The results are shown as the maximum projection of the redox ratio represented by a pseudo-color scale, with red indicating a high signal level and blue indicating low signal level. It can be seen that both ischemia groups have higher redox ratio values, which indicate a more
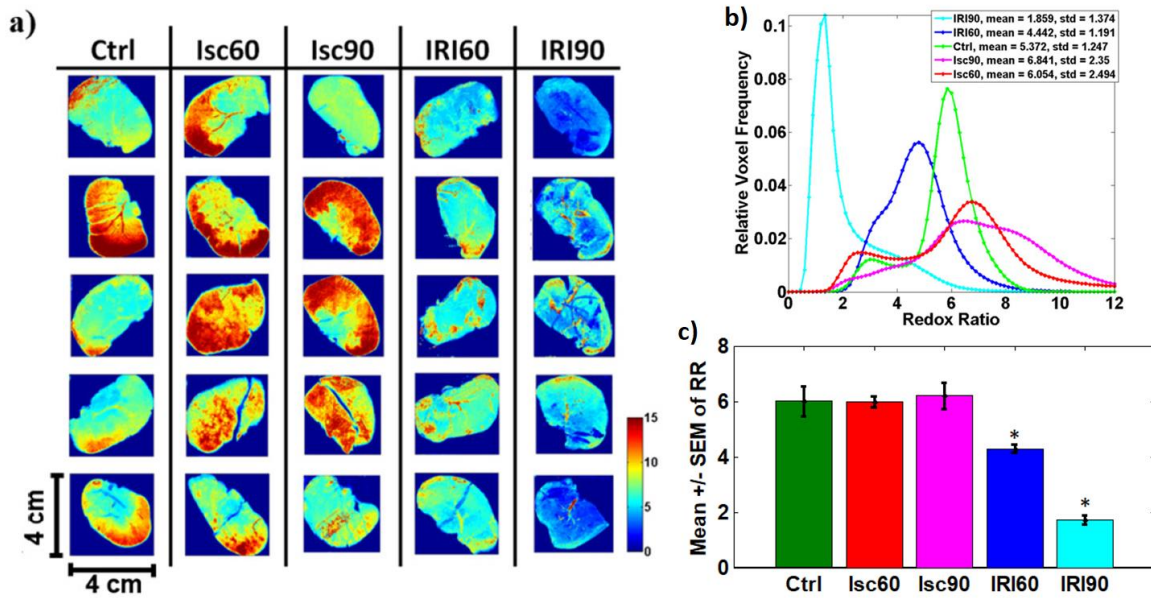
Figure 12: The mitochondrial redox state of livers exposed to ischemia reperfusion. a) Maximum projection of the redox ratio for n = 5 samples in each group. Each image scale is 4 cm × 4 cm. b) Relative voxel frequency distribution of redox ratio for a representative sample in each group. c) Statistical analysis of mean values of RR with n = 5 samples in each group and significant difference marked with *.

reduced metabolic state, whereas both reperfusion groups show lower redox ratio values and a more oxidized state. From the full 3D reconstruction of the redox ratio images, the relative voxel frequency distribution of the redox ratio for each sample was constructed. These can be seen in Figure 12b for a representative sample from each group. The ischemia groups have slightly higher redox ratio (RR) levels than the control, and the reperfusion groups show two levels of lower RR. A bar plot of the RR values for each group of samples can be seen in Figure 12c. This revealed no significant difference between the control and both ischemia groups. However, there were significant differences between the control and reperfusion groups ($p = 0.0168$ for IRI60 and $p = 2.79 \cdot 10^{-7}$ for IRI90). It was found that the IRI60 group had a 29% decrease in RR, whereas the IRI90 group had a 71% decrease in RR.

2.3. Discussion

Mitochondrial dysfunction and the resulting apoptotic cell death have a major role in the pathology of many diseases in different organs [114-121]. The dysfunctionality of mitochondria can be seen by dysregulation in mitochondrial metabolic activity. Therefore, measuring the mitochondrial metabolic state could potentially be an early indicator of organ dysfunction during the disease.

In this chapter, I presented two methods that measure fluorescence from both NADH and FAD, allowing calculations of the redox ratio, which has proven to be a powerful diagnostic marker [41]. The first method, *in vivo* fluorescence imager, can map the surface redox ratio of wounds in 2D, noninvasively. Fluorescence redox imaging was also performed using the 3D optical cryo-imager. FAD autofluorescence signal originates only from mitochondria [122, 123]. The primary source of NADH is mitochondria, with negligible contribution from cytoplasmic sources and minimal impact from NADPH [123-125]. Cytosolic NADPH, which has the same fluorescence characteristics as NADH, could be contributing to the signal attributed to NADH in this study. However, Chance et al. demonstrated that the fluorescence signal originates mostly from NADH in the mitochondria, and the contribution of NADPH - present in cytosol - is very small [126]. The fluorescence signal is mainly from NADH since its quantum yield is much higher than NADPH (1.25 to 2.5), its concentration is 5 times larger than NADPH, and is the only one affected by metabolic perturbations [127-129]. Thus, NAPDH's contribution to the NADH signal and the change in the NADH signal due to diseases studied in this thesis was assumed to be small and was ignored.

Fluorescence metabolic imaging was performed to determine the changes in mitochondrial redox state and use data to predict the progression of different ROS-mediated diseases and injuries

including, diabetic wounds, uninephrectomy, radiation-induced injuries, and ischemia-reperfusion injury. The therapeutic actions of FR-PBM on diabetic wounds and lisinopril treatment on irradiated kidneys. Mitochondrial redox state was analyzed in mouse eyes suffering from these diseases. The percentage change in the signals was expected to correlate with the severity of injuries in the tissue (injured vs. normal).

A) Diabetic wounds and FR-PBM. Our custom-designed non-contact non-invasive fluorescence imager detected the effect of diabetes and FR-PBM on wound healing trajectory by monitoring the mitochondrial metabolic state quantitatively. At days 2, 4 and 6 of post-wounding, the redox ratio of diabetic wounds was lower than those of controls. At days 6 and 9 of post-wounding, the redox ratios in FR-treated wounds on diabetic mice were higher than those of sham-treated animals. The cryo-imaging confirms the results from in vivo fluorescence imaging. These results support our previous investigations documenting the ability of FR-PBM to decrease oxidative stress and improve mitochondrial function [130, 131]. The mitochondrial dysfunction of wounds in diabetes is mitigated by FR-PBM, resulting in an accelerated healing process.

B) Uninephrectomy (UNX). We found that by day 3 following UNX, rats exhibited a significant decrease of the global redox index compared to sham controls. Mitochondrial oxidative stress is crucially involved in renal hypertension [132-141] and the ability of the nephrons to maintain a balance of the redox ratio necessary for normal bioenergetics was therefore diminished. This was observed in both the cortex and medulla of left (remaining) kidneys when compared to the matched right (removed) kidneys of the UNX rats. This indicates that both regions of the remaining kidney were utilizing more oxygen and requiring more energy to compensate for the function of the missing kidney, as was determined by studies of primary cultured proximal tubular cells from the remnant kidney of UNX rats [32]. As the proximal tubular hypertrophies, there is an increase in

the basolateral surface area of nephron and an associated increase of Na^+-K^+-ATPase activity [10]. This enables the remaining kidney to cope with the increased energy needed to reclaim the greatly increased filtered amounts of Na+, glucose, amino acids, and other solutes suddenly thrust upon the remaining kidney. Greater mitochondrial ROS production associated with the greater workload of the remaining nephrons could lead to uncoupling of oxidative phosphorylation and cell mitophagy, but the extent to which this occurs following UNX has not been quantified.

C) PBI kidney and lisinopril treatment. 3D optical cryo-imaging revealed that a single dose of PBI caused significant oxidation of the whole kidney redox state (NADH/FAD) due to lower NADH and higher FAD in the kidneys of irradiated rats compared to non-irradiated controls. Therefore, in mitochondria of irradiated kidneys, there was less NADH and more FAD compared with non-irradiated rat kidneys. That is, the ability of the nephrons to maintain balanced NADH/NAD ratio necessary for normal bioenergetics is diminished following irradiation. Hence, these changes would result in the lack of availability of adequate reducing equivalents necessary for the ETC to generate the electron-motive force required for ATP production in the irradiated kidneys. The altered mitochondrial metabolism and bioenergetics after PBI could contribute to potential compromise in renal function. The increase in the oxidized state of mitochondria following exposure to radiation could be ascribed, in part, to impaired ETC function. In this case, it is possible that the higher NADH oxidation without a concomitant increase in ATP production could cause an increase in reactive oxygen/nitrogen species (ROS/RNS) production [142, 143]. On the other hand, another report suggests the lack of the oxidative stress in the irradiated kidney by routine biochemical assays such as measurements of lipid peroxidation, carbonylated proteins or DNA oxidation [144].

Our findings confirm the results of previous studies, which showed that lisinopril, an ACE inhibitor, is effective against radiation-induced nephropathy [145]. Our findings are also in line with reports suggesting that lisinopril can be considered for use in clinical trials for the treatment of radiation injuries [146]. The rats in our study were administered lisinopril in their drinking water (see Methods), but lisinopril can be given once a day, and this provides a clinical advantage over other ACE inhibitors such as captopril, which has a shorter biological half-life and must be dosed more frequently [146]. Consistent with our previous study [85], showing that lisinopril could mitigate the radiation-induced injury on multiple organs, the present study revealed the contribution of this ACE inhibitor on the renal redox state as a potential mechanism for ameliorating the injury. The significant improvement in the redox state of PBI kidneys after lisinopril treatment suggests that renal mitochondrial disruption after PBI was mitigated by lisinopril. Furthermore, the mitigating effects of lisinopril could be ascribed, in part, to a decrease in oxidative stress.

D) WTI heart exposed to IR. The oxidation of the mitochondrial redox state on reperfusion tended to be more pronounced in the irradiated hearts, albeit not significant. This observation suggests that mitochondrial metabolism was not altered after WTI. Furthermore, the similarities in redox state in the two groups before, during, and after ischemia suggest that cardiomyocyte mitochondrial physiology was preserved during exposure to the brief pulse of WTI.

An increase in the oxidized state of mitochondria following ischemia could be ascribed to, in part, impaired ETC function and OXPHOS. Higher NADH oxidation without a concomitant increase in ATP production suggests an increase in reactive oxygen/nitrogen species (ROS/RNS) production, which are contributing factors in IR injury [142, 143, 147]. We showed previously that ROS and RNS production increase dynamically in the ex vivo perfused heart during ischemia and

on reperfusion, and the magnitude of cardiac functional recovery correlated with the extent of ROS or RNS produced. Thus, cardioprotective interventions that mitigate IR damage and improve functional recovery on reperfusion show significant attenuation of ROS emission during ischemia and on reperfusion [148]. Our functional data in the current study infer that WTI may not predispose irradiated hearts to more ROS production during IR and hence, worsening of cardiac function.

E) Ischemia reperfusion injury in livers. The main mechanism of injury in hepatic IRI is due to an immune-mediated response during the reperfusion phase [149]. This also matches well with our results because we see a significant difference in the severity of damage in the reperfused livers according to the duration of ischemia before reperfusion. The reperfusion groups both show lower redox ratios than the control group, indicating a more oxidized redox state. The change in coenzyme levels during hepatic IRI has been known to be incongruent, and it is difficult to interpret. The exact details of NADH and FAD metabolism during hepatic IRI remain elusive, though a report on human liver perfusion models indicated that the NADH:NAD ratio was unchanged after reperfusion, but the estimated FAD level was increased [150]. This means that RR, which is NADH/FAD, decreased, and it agrees with our findings that the RR decreased as the severity of the IRI increased.

The current study demonstrated the utility of RR to detect ocular and mitochondrial OS in multiple animal injury models. Moreover, I have designed and implemented a vascular segmentation algorithm from the cryo-images that is going to be explained in the next chapter.

Chapter 3

Vascular-Metabolic Imaging of

Whole Organs

3. Vascular-metabolic imaging

The objective of this research is to segment and quantify 3D vascular network of the whole organs to examine the vasculature alterations that can be caused by injuries and to provide a platform that can serve as the basis to evaluate vascular therapeutics in diseases. Most diseases are associated with endothelial and capillary injuries in blood vessels. It is expected that the quantitative monitoring of 3D vascular morphology can give more information on the progress of vessel dysfunction during progressive diseases.

We propose an approach that enables us to only perform auto-fluorescence metabolic imaging but provide both metabolic and vascular information simultaneously. Fluorescence metabolic imaging techniques pioneered by Chance et al. [107] have been developed to measure mitochondrial redox state (NADH/FAD). Fluorescence imaging or spectroscopy of metabolic indices provides 2D functional maps from the surface of tissues *in vivo* or ex vivo [44, 151, 152]. 3D functional maps can be built using our fluorescence cryo-imaging, which provides a 3D mitochondrial redox state of the tissue [21].

In this study, we present a high-resolution segmentation algorithm for vasculature detection, which is based on intrinsic fluorescence images. This novel technique enables vascular detection without the need for labeling vessels with contrast agents. We termed the technique 'vascular-metabolic imaging' (VMI). It is the foreground intrinsic fluorescence (NADH or FAD) that reveals the background vessel network devoid of such metabolic signatures. We hypothesized that the dark voxels are associated with the vasculature because the red blood cells quench the auto-fluorescence signals from NADH and FAD [107]. Our segmented vasculature from VMI quantifies a 3D vascular network of whole organs, such as kidney, lung, heart, and liver.

Remarkably, VMI, via intrinsic fluorescence, can produce both metabolic redox state and vascular information simultaneously that is currently unattainable with any other existing imaging tools. We validated our vascular detection approach by co-registering the VMI vessel images with the vessel images segmented from red fluorescence images of a genetically-modified rat kidney (TdTomato) tagging endothelial cells. Here, we also demonstrate the capability of our vascular segmentation approach by illustrating vascular damage in a rat partial body irradiation injury model.

3.1. Vascular segmentation algorithm

Figure 13 shows the flowchart of the proposed algorithm that can segment background vasculature from the foreground 3D intrinsic fluorescence images. Below is the sequence of steps that are carried out to obtain and reconstruct a vascular network from the inverted fluorescent image.

Step 1. *Brightness and contrast adjustments*: The captured intrinsic fluorescence intensity might be different from samples to samples. This step of the algorithm is designed to specifically normalize the variations in the intensity of images from various samples. Contrast enhancement is generally used to make objects in an image more distinguishable. Therefore, remapping intensity values to the full range of 16-bit images helped us to sharpen the differences between the black and white voxels.

Step 2. *Image inversion*: In our application, the objects of interests (vascular network) are the dark voxels. The inverted image can show up the vasculature as the light voxels to be able to segment vasculature using background subtraction.

Step 3. *Background Subtraction*: A background subtraction algorithm called rolling-ball background correction [153] is used next. The rolling ball radius in each organ should be at least set to the largest vessel radius that we expect the organ possesses.
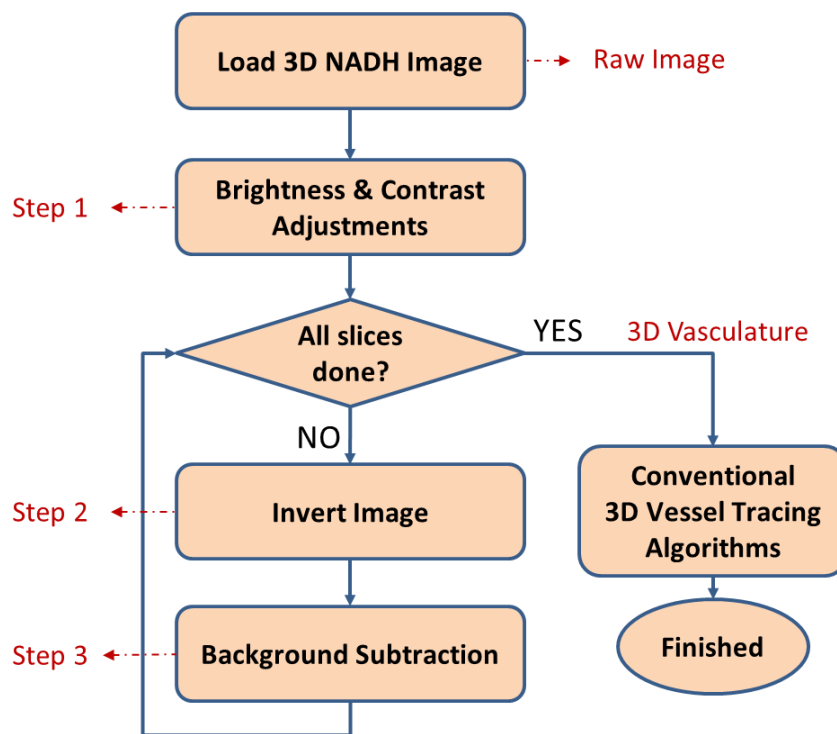
Figure 13: Algorithm flowchart for background vasculature segmentation from fluorescence images. After loading the 3D stack of images, the brightness and contrast are adjusted to have an enhanced image. Then, for each slice, the image is inverted, and the background is subtracted. The reconstructed 3D vasculature can be fed to 3D vessel tracing algorithms for quantification purposes.

Background subtraction is traditionally used in fluorescence microscopy to isolate bright objects from an uneven illumination [154].

Brightness and contrast of 3D NADH fluorescence images are adjusted to the whole volume intensity range, but the image inversion and background subtraction are performed on each 2D slices separately. Final contrast enhancement is also done on the 3D structures. Before feeding the 3D vasculature images to the tracing algorithm, the heart cavities (atria and ventricles) were masked out using a thresholding mask calculated from the original NADH images. Also, for the kidneys, the segmented vasculature from the medullary region was masked out to ensure total removal of any false segmentation originating from renal tubules within the medullary region. Since most of the vascular network of the kidney lies in the cortical region, this removal of medullary voxels will only remove a small portion of the 3D vascular network, while making sure that the segmented vasculature does not have the tubular network.

50

3.2. Vascular quantifications

By tracing the 3D vessel networks, we can track, measure, and quantify the vasculature. We used Imaris 9.5 software (Bitplane Inc.) and their filament tracing algorithm, which is based on local intensity contrast. It traces and finds the path from a large starting point(s) to the small terminal points (Figure 14A). Then, the vessel branches can be quantified to provide various vascular biomarkers. For an instance, the diameter of a vascular branch (Figure 14B) can be calculated as illustrated in Figure 14C.
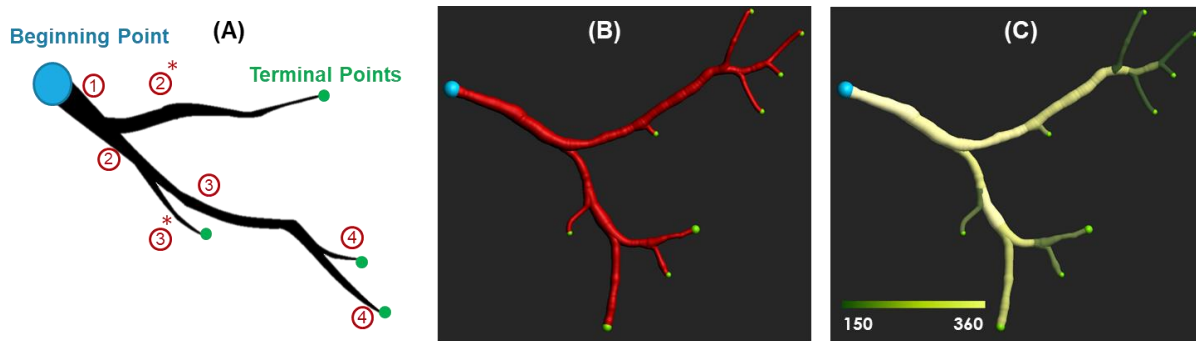
Figure 14: Quantification of vascular markers. (A) a schematic view of a branch: a vessel tracing algorithm the terminal points, and the beginning point and how the branch depths are increasing in each branch are shown. (B) a simple branch illustrated with its terminal points. (C) The branch color-coded with Vessel Diameter (µm).

There are multiple vascular quantifications that have a key role in diagnosis and therapeutic applications. The number of branches and the number of terminal points (smallest detected branches) can be related to the vascular network (Figure 14). The quantifications regarding the size of branches include vessel diameter and volume are related to vasoconstriction or vasodilation.

3.3. Validation

3.3.1. Td-tomato rats

A genetically-modified rat model expressing TdTomato in mostly vascular endothelial cells was utilized to image the vasculature in kidneys. Histological assessment of rat kidneys was also done

to visualize TdTomato expression in endothelial cells of these rats using an antibody for TdTomato. The capability of the 3D fluorescence cryo-imaging system to acquire images from multiple channels simultaneously allows us to have both red and NADH fluorescence of the kidney. We used the foreground vasculature extracted from red fluorescence as proof for examining the vasculature segmented from the NADH channel. The co-registration of the vascular network extracted from the two channels validates the proposed method of our vascular segmentation.

3.3.2. Dice coefficient

One of the common metrics for evaluating the quality of image segmentation is the Dice coefficient, which measures the overlap between the ground truth and the test [155]. For calculating the Dice coefficient, we let the 3D volume be represented by the point set $X = [x_1, \dots, x_N]$, where N is the total number of voxels. We let the red vasculature be represented by the partition V_{red} of X with assignment function $f_{red}(x)$, i.e., voxel intensity at x, and we let the VMI vasculature be represented by the partition V_{vmi} of X with assignment function $f_{vmi}(x)$. Then, the Dice coefficient is defined by:

$$Dice = \frac{2|V_{red} \cap V_{vmi}|}{|V_{red}| + |V_{vmi}|} = \frac{2\sum_{i=1}^{N} f_{red}(x_i) f_{vmi}(x_i)}{\sum_{i=1}^{N} f_{red}^2(x_i) + \sum_{i=1}^{N} f_{vmi}^2(x_i)} \tag{1}$$

where the numerator represents the common elements between the two images. To quantify $|V_{red}|$ and $|V_{vmi}|$, we used the squared sum operation. There is a multiplication by 2 in the numerator because the denominator counts the common elements twice.

The branching structure of the VMI vasculature can also be compared with red fluorescence vasculature. Murray [156] proposed an optimization theory that the fundamental

structure of a vascular tree should be such that it minimizes work. Murray's law states that a branch that fallows the "minimum work" hypothesis should also follow the equation:

$$(D_p)^3 = \sum_d (D_d)^3, \tag{2}$$

where D_p indicates the diameter of a parent vessel, and D_d indicates the diameter of the dth daughter vessel coming from the parent p. The equation 2 can be stated as the cubed diameter of a parent vessel is equivalent to the sum of the cubed diameter of its daughter vessels.

After employing the tracing algorithm using Imaris, we used the information on the depth of the vessels to define the parents and daughters. The depth of a vessel increases every time a bifurcation happens in the branch. Therefore, all vessels with a specific depth k+1 are the daughter vessels of the parent vessels with depth k and the Murray's law can be written as:

$$\sum_p (D_p^k)^3 = \sum_d (D_d^{k+1})^3, \tag{3}$$

where D_p^k indicates the diameter of pth parent vessel at depth k, and D_d^{k+1} indicates the diameter of the dth daughter vessel at depth $k+1$. Now, we can look at the relationship between the parent vessel diameters with their daughters' diameter by having the depth information of the vessels. The summation of the cubed diameter of all the vessels at each depth (parents in the left side of equation 3) are then compared with the summation of the cubed diameter of all the vessels at next depth (daughters in the right side of equation 3). A vascular data follows the Murray's law if this relationship is significantly linear and has a linear fit close to identity line.

Notably, using the depth to find the parent-daughter relationship in vessels, can impose an unavoidable error by making the left side of the equation 3 higher than the real value. The reason

is that the terminal branches from lower depths (starred in Figure 14A) are considered as parent vessel while there is no corresponding daughter in the next depth.

3.3.3. Murray's law

The branching structure of VMI vasculature can also be compared with red fluorescence vasculature. Murray[156] proposed an optimization theory that the fundamental structure of a vascular tree should be such that it minimizes work. Murray's law states that a branch that fallows the "minimum work" hypothesis should also fallow the following equation:

$$(D_p)^3 = \sum_d (D_d^p)^3. \tag{4}$$

where D_p indicates the diameter of the p$^{\text{th}}$ parent vessel and D_d^p indicates the diameter of the d$^{\text{th}}$ daughter vessel coming from p$^{\text{th}}$ parent. The equation two means the cubed diameter of a parent vessel is equivalent to the sum of the cubed diameter of the daughter vessels.

After employment of tracing algorithm using Imaris, we used the information on the diameter and the depth of the vessels. The depth of a vessel increases every time a bifurcation happens in the branch. By having the depth information of the vessels, the Murray's law can be simplified as

$$\sum_p (D_p)^3 = \sum_p \sum_d (D_d^p)^3, \tag{5}$$

which means the summation of the cubed diameter of all the vessels at depth k (parents, left side of equation) should be equivalent to the summation of the cubed diameter of all the vessels at depth k+1 (daughters, right side of equation).

3.4. Proof-of-concept using irradiated rat models

Leg-out partial body irradiation (PBI) rat model has been extensively explained in our previously published studies [59, 108, 109]. In short, the rats were placed in Plexiglas jig and irradiated uniformly by X-rays with shielding only one hind limb. Therefore, most vital organs have been irradiated and make the animal model a good choice to study multiple organ injuries by irradiation. A high dosage of radiation is well-known to damage the vessel networks of organs substantially. Therefore, a well-established radiation-induced animal injury model such as PBI can provide a proper example that allows us to show the sensitivity and efficacy of the algorithm to detect the vascular damage. In this study, 4 doses of radiation have been studied; 0Gy, 7.5Gy, 10Gy, and 12.5Gy (n=3/group).

3.5. Results

3.5.1. 3D vascular-metabolic imaging (VMI)

Figure 15 supports our hypothesis that a foreground fluorescence image can be inverted to reveal the vasculature of an organ like the kidney. The 3D raw NADH (excitation at 350nm and emission
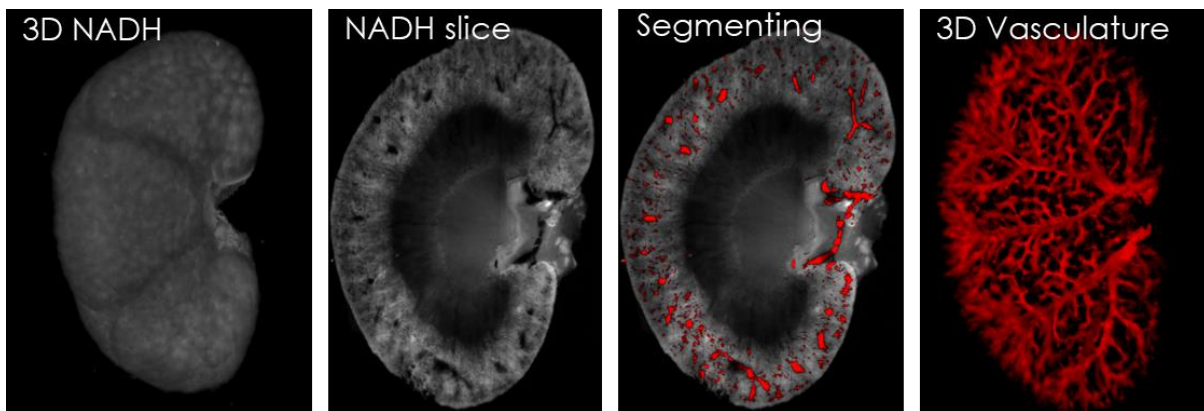
Figure 15: A background vasculature is segmented from a foreground intrinsic fluorescence image of a kidney*. For a rat kidney, a 3D raw image of NADH fluorescence is shown. A sagittal slice view of raw kidney image is chosen, and the segmented vasculature from dark voxels is shown in red and merged with the raw slice to show the localization of the vascular pixels in the image. The 3D vasculature is reconstructed from all 2D segmented pixels.*

at 460nm) image of a kidney, a sagittal slice of the kidney, and the segmented vasculature on one slice are illustrated in Figure 15. The stack of 2D vascular images reconstructed to generate the 3D vascular images of the whole kidney.

VMI can also be applied on other organs, such as heart and liver. Figure 16 shows a selected representative slice for the step-by-step outcome images of the algorithm for each organ: kidney, heart, and liver. In step 1, the contrast and brightness of the images are enhanced. The inverted images of 1 slice of each organ can be seen in step 2. Now, the feature of interest (vasculature) is bright in the image. A background-subtracted image of the slice can be seen in step 3 images. The resulting 3D vascular images are reconstructed from the stack of 2D images.
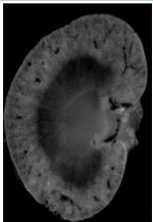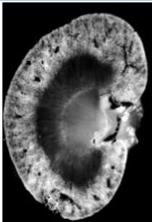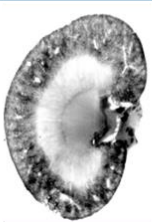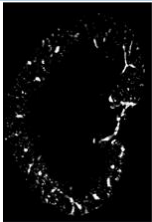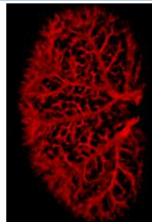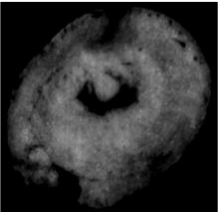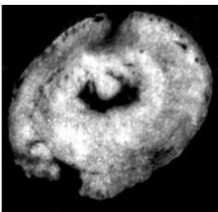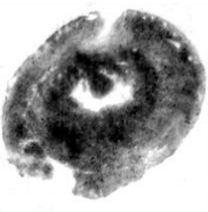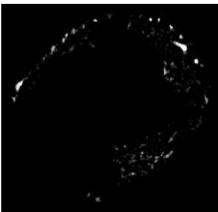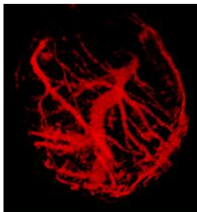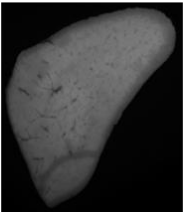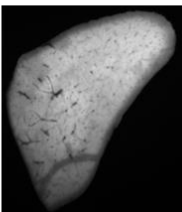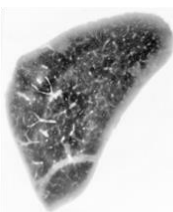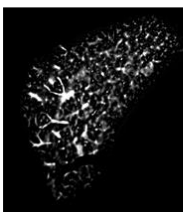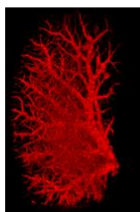
Figure 16: VMI can be used to segment vascular networks of multiple organs, including rat kidney, mouse heart, and rat liver. *An example slice in each step of the algorithm is illustrated for each organ. Step1 is contrast enhancement, step2 inverts the image, step3 background subtraction, and at last, the 3D vasculature is reconstructed.*

3.5.2. 3D vasculature of airway-injected lungs.

Vascular segmentation from the background of intrinsic fluorescence in lung tissues was not feasible because the vasculature, airway, and alveoli appeared dark in the images. Therefore, distinguishing the vasculature from these structures was not possible. To circumvent this problem, we instead injected a FITC solution into the airway and alveoli. Extrinsic fluorescence from FITC (excitation at 494 and emission at 537) and FAD (excitation at 437 and emission at 537) are overlapped. This overlap and the injection of a FITC solution into the airway and alveoli, enabled us to lighten the airway in FAD images and keep the vascular structures dark (Figure 17). Afterwards, the same proposed segmentation algorithm was applied to extract the inverted
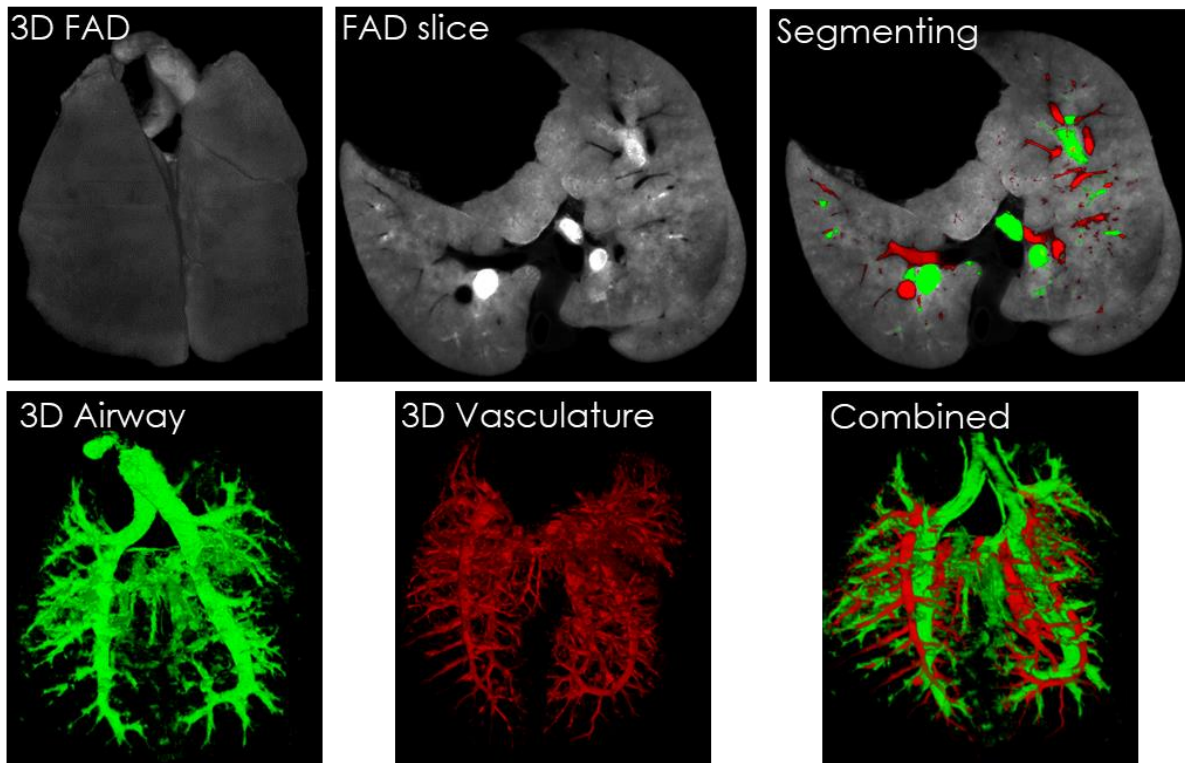
Figure 17: FITC airway injection helps to segment background vasculature from lungs. For a rat lung, FITC-dextran solution is injected into the airway. A raw 3D image of FAD fluorescence of Lung is shown. A transverse slice view of raw lung image is chosen, and the segmented airway from light voxels of FITC image and vasculature from dark voxels are shown in green and red, respectively. Segmented airway and vasculature are merged with the raw slice to show the localization of the vascular and airway pixels in the segmenting image. Also, the 3D vasculature and airway are combined and shown zero intersection with each other.

57

vasculature from the FAD images of the lungs. Figure 17 shows a 3D raw FAD image of the lung and a single slice of the lung. The airway, which is filled with FITC solution are segmented from light voxels, and vasculature is segmented via inversion of FAD images for lungs. The 3D vasculature (in red) and airway (in green) are then reconstructed as shown in 3D. In the combined or merged images, the voxels that have an overlap between the segmented airway and vasculature should be in yellow color, but due to a very little intersection, no yellow voxels appeared in the figure. The Dice coefficient < 0.001 also confirms that the airway and the vasculature had no overlap. These results demonstrate that the segmentation structures from inverted FAD images do not originate from airways but from the vasculature. Note that the FAD images are originating from both FITC and FAD fluorescence now. This helped us to lighten the airway, but the FITC fluorescence in airway also interfere with the FAD signal. Therefore, on the downside, the mitochondrial metabolic imaging does not work in the airway-injected lungs.

3.5.3. Co-registration with TdTomato rat kidney to confirm VMI vasculature

The transgenic rat model called Td-tomato is utilized as the ground truth for validating vascular segmentation method. By utilizing the TdTomato rat model, the cryo-imaging was performed in the two channels of NADH (excitation 545, emission 645), and red (excitation 545, emission 645) fluorescence. The bright voxels in the red channel and the dark voxels in the NADH channel are segmented and reconstructed (Figure 18a and Figure 18b, respectively). The anatomy of the vasculature extracted from the NADH using VMI is then combined with the vasculature segmented from red fluorescence (Figure 18c). The merged parts that overlap display yellow color. The co-registration evaluation gives a dice coefficient of 0.91, which shows a high degree of overlap between the two segmented vasculatures. In red fluorescence vessels, due to the selective staining of the endothelium rather than blood, the imaging of larger vessels is not feasible, but VMI is ideal

3D Vasculature from red fluorescence   3D vasculature from inverted NADH

(a)

(b)

Co-registration

(c)
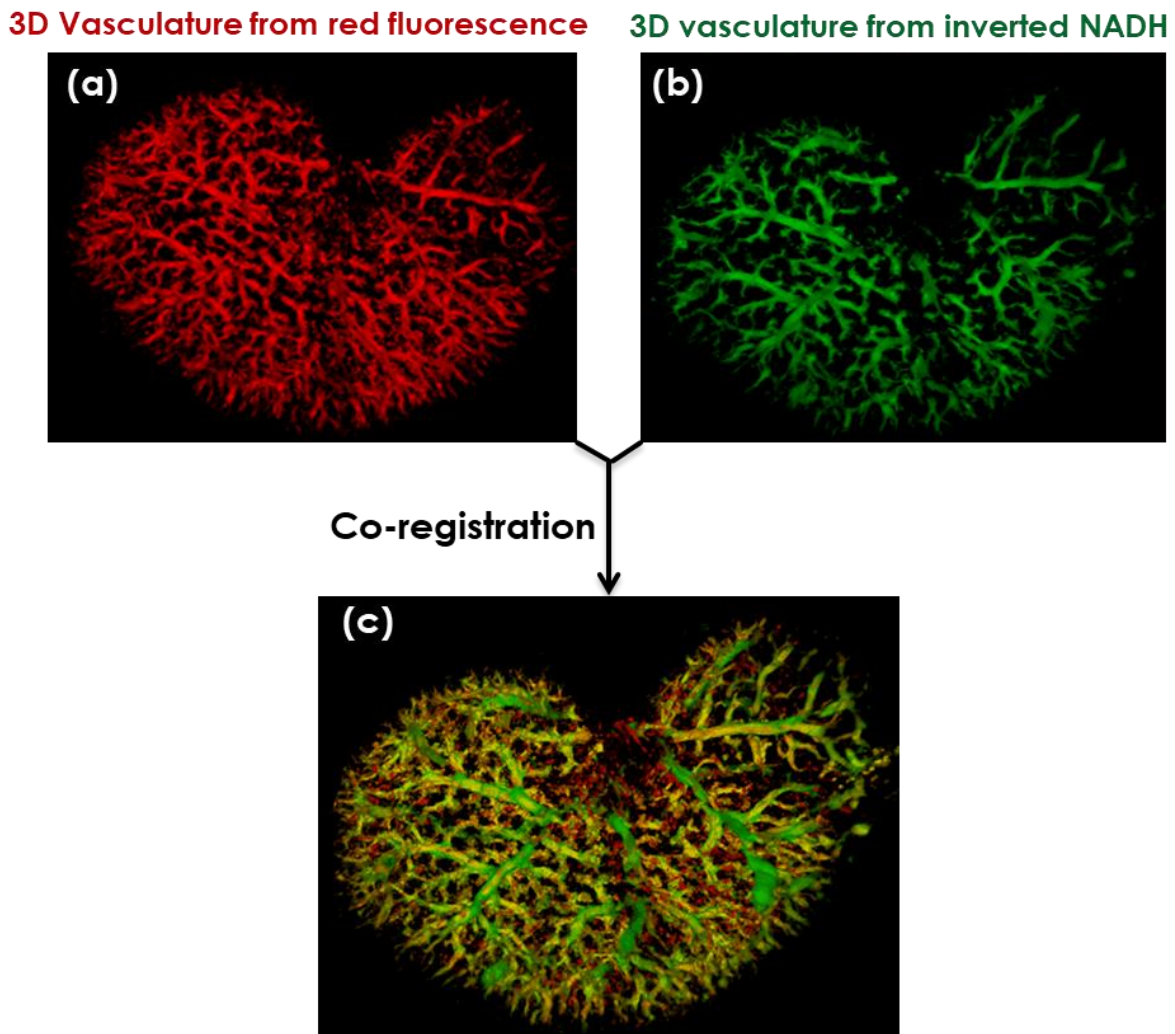
Figure 18: TdTomato rat kidney validates that VMI has high overlap with expressed vessels in red fluorescence*. The red channel is used as the ground truth for validating the vasculature extracted using VMI. The segmented vasculature from light voxels of red channel and vasculature from the dark voxels of the NADH channel (VMI technique) are shown in red and green, respectively. Segmented vasculatures are then combined to localize their intersection in yellow. The dice coefficient of 0.91 shows a great precision in vascular segmentation.*

for imaging and quantifying larger vascular structures. That might explain the small number of voxels in pure green or red color in the coregistred image (Figure 18).

The branching of the two vasculature is also compared in Figure 19. The relationship between the cubed diameter of the parent vessels to the summation of the cubed diameter of their corresponding daughter vessels are presented. Using linear regression, two lines are fitted to each set of data points and are shown in Figure 19. According to Murray's law, the data should be fitted
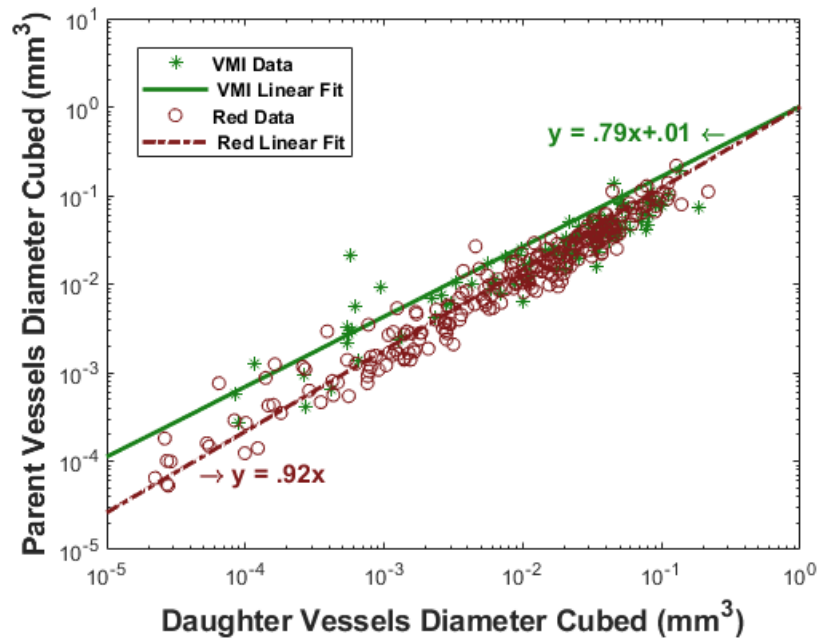
Figure 19: VMI follows Murray's Law. *The parent vessel diameter cubed is plotted against the sum of the diameter cubed of their corresponding daughter vessels. The data from red fluorescence of TdTomato rat are shown as red circles, and the data from vasculature extracted using the VMI technique are represented as green stars. Two vascular branching data from VMI and red fluorescence have merged, and their linear regression fit has shown very good compliance with Murray's law (identity line, y=x).*

to y=x line, i.e., a line with slope of 1 and y-intercept of 0. The y-intercepts for both lines are negligible, and the slopes for both VMI and Red channel are close to 1, indicating that the VMI branching like the red vascular branching follows Murray's law and the "minimum work" hypothesis successfully.

3.5.4. Partial body irradiation in different doses

Here, we present a selected example that illustrates the capability of VMI to uniquely drive the topography of two sets of parameters simultaneously: mitochondrial redox state and the 3D vascular network of whole organs. Figure 20 illustrates the representatives of the 3D rendered vascular networks of kidneys, livers, and lungs from rats exposed to different irradiation doses. Their corresponding 3D redox ratio (NADH/FAD) of kidneys and livers are also presented in
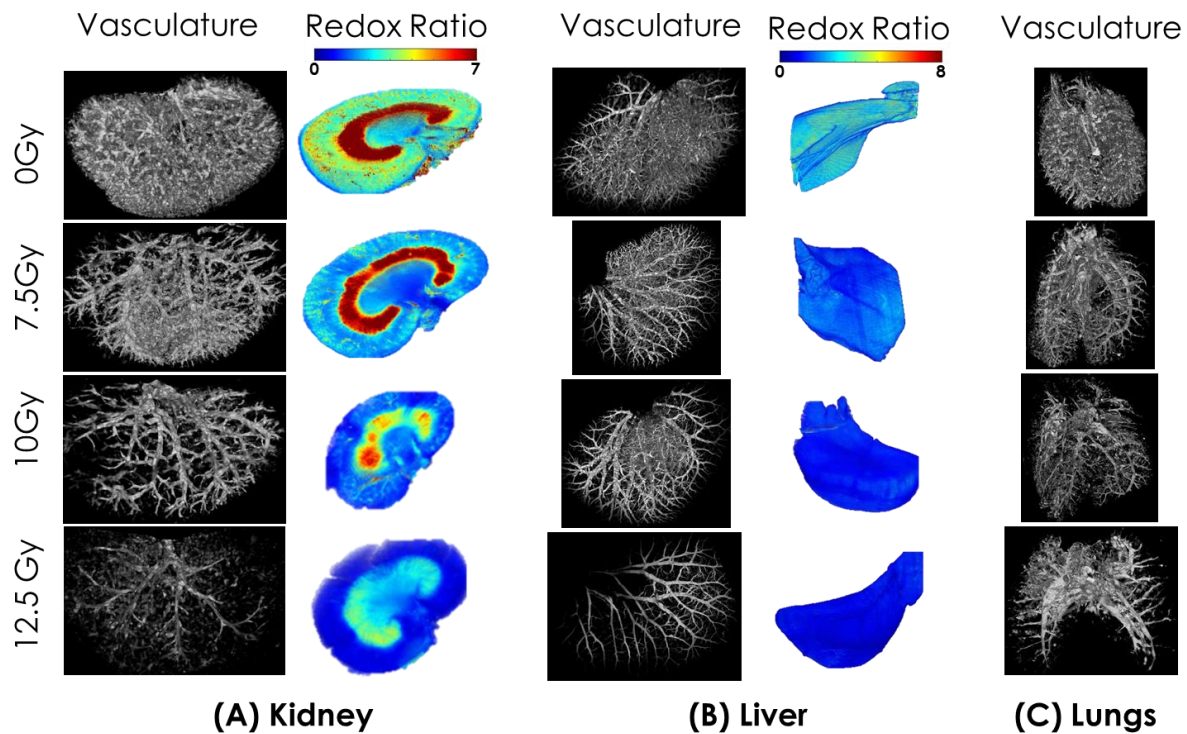
Figure 20: Different doses of PBI caused related vascular-metabolic damage in kidneys (A) and livers (B), and lungs (C). As the dosage of irradiation increases the vascular damage is increasing while the redox ratio decreases.

Figure 20. The redox ratio images of the lungs are not presented due to the interference of FITC with FAD.

The vascular networks in Figure 20 illustrates the strong virtual destruction of the vessel networks after PBI. The vascular damage in kidneys and lungs also correlated to the dosage of irradiation in the PBI rats. The redox ratio images are pseudo-colored with higher redox ratio voxels shown in red, and the lower redox ratio voxels in blue. The kidneys and livers undergone a higher dosage of irradiation are more prone to a drop in the redox ratio, i.e., more oxidized mitochondrial redox state.

3.5.5. Partial body irradiation and lisinopril treatment

Figure 21A illustrates representatives of the 3D rendered vascular networks from each group of rat kidneys. The virtual destruction of the vessel networks after PBI is strong. The damage to the

vessels due to irradiation was significantly mitigated in kidneys obtained from rats exposed to PBI+lisino compared to the PBI group. The mean vessel diameter of kidneys in the PBI rats was significantly reduced by 45%, and lisinopril treatment caused 44% improvement in the vessel diameter of PBI kidneys compared to PBI kidneys (Figure 21B). This result shows that radiation leads to significant vasoconstriction, and lisinopril negates this by increasing dilatory response.
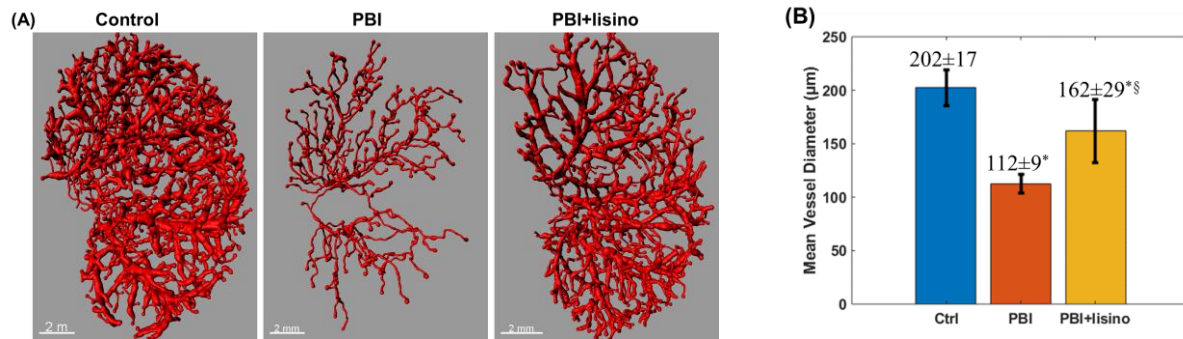
*Figure 21: Radiation-induced vascular injury and lisinopril treatment. A) Representative three-dimensional rendered vascular network of kidneys from each treatment: Non-irradiated (Control), Partial Body Irradiated without (PBI) and with lisinopril treatment (PBI+lisino). B) Bar plot of mean vessel iameter of vascular network of kidneys from each treatment. *Significant difference when compared with Control (P < 0.05); §significant difference of PBI+lisino when compared with PBI (P < 0.05).*

3.6. Discussion

Due to the weak intrinsic signals in tissue auto-fluorescence metabolic imaging, the auto-fluorescence images have limited tissue contrast anatomically when compared to the histology images. This limitation was partially circumvented in this study by using vascular-metabolic imaging (VMI) and providing the 3D vascular network of the whole organs. Here, we demonstrate the feasibility of VMI to generate anatomical and physiological information simultaneously. The vascular segmentation algorithm in VMI uses the same 3D auto-fluorescence cryo-images that we have used previously to produce tissue mitochondrial redox state [44, 59, 157].

A genetically-modified rat model of endothelium selective expression has been chosen as the ground truth testing. The high overlap between the red fluorescence of TdTomato rat kidney and VMI vasculature indicates the specificity of VMI in the segmentation of vascular networks. Also, we have shown that the minimum work hypothesis proposed by Murray has been satisfied by both approaches. This suggests that the VMI vasculature has similarities in branching with the ground truth vasculature as generated by TdTomato.

The potential interest of combining exquisitely sensitive intrinsic metabolic information with vascular information was demonstrated in a proof-of-concept study of radiation-induced damage to multiple organs. 3D mitochondrial redox state of PBI rat kidneys and livers were examined. The mitochondrial redox state of kidneys and livers dropped in close relation with irradiation dose. This result is consistent with our previous study [59] showing that the radiation diminished the ability of the cells to maintain balanced mitochondrial redox state necessary for normal bioenergetics in kidneys. Using VMI, the vascularization in different doses of irradiation was examined in the kidneys, livers, and lungs. We showed that the exposure to irradiation could also cause significant vasoconstriction, which in turn can decrease the available oxygen and trigger an increase in the oxidation state of cells. This implies the existence of tight links between the deregulation of mitochondrial metabolism and the abnormal vasculature typical of radiation injuries [110, 158, 159]. Together, this study showed that vascular metabolic imaging using intrinsic fluorescence can successfully stratify the dosage of irradiation based on these two hallmarks of injury.

The proposed algorithm in this study has generated both vascular and metabolic information with major implications:

a) The vascular images are produced without the use of any extrinsic contrast agents or tissue clearing-solvents, which might induce structural deformity by itself [160].

b) Since the technique uses optical imaging technologies, it is capable of high-resolution imaging compared to X-ray or ultrasound instruments. By increasing the resolution of the fluorescence cryo-imaging instrument, VMI can present additional details in the vascular networks.

c) The co-registration of metabolic and vascular images has perfect precision because they originate from the same 3D images.

d) Unlike laborious, complex, and time-consuming sample preparation in micro-CT [14], the only sample preparation needed for VMI is snap-freezing the samples in liquid nitrogen. In addition, VMI is less time consuming, and VMI of a whole rat organ takes less than 2 hours to finish.

e) Vascular images of the kidney, lung, heart, and liver were segmented here using VMI. This VMI approach could be extended to other organs and pathologies, such as eye, skin wounds, and tumor as we [52, 157] and others [161] have investigated in previous reports.

f) VMI is implemented by adding an image processing algorithm to the existing 3D fluorescence cryo-imaging. Therefore, no major hardware modification is needed to extract vascular network of organs from intrinsic fluorescence. Also, fluorescence metabolic imaging systems are much more cost-effective in comparison to other similar 3D whole organ vascular imaging modalities, such as micro-CT.

g) VMI can extract vascular networks from not only NADH or FAD fluorescence but also any inverted intrinsic fluorescence images that are devoid of red blood cells.

Vascular-metabolic imaging can be applied to quantitatively characterize the organ vasculatures and the metabolic state simultaneously. The vascular-metabolic imaging can also explore the pathophysiology in rodent injury and treatment models. Optical metabolic imaging has been used in this application for several years [42, 44, 48, 49, 59, 157], and by using the proposed segmentation technique, another key hallmark of injury, vascular quantifications, would significantly help in understanding the underlying effects of injuries and their treatment options in multiple organs. For example, VMI of tumors can expose the effects of drugs and radiotherapy on

the tissue metabolism and vascularization in various animal models of cancer. Also, the vascular-metabolic imaging offers the attractive options in hearts, such as the studies of the interaction of tissue metabolism, vasculature, and elasticity during myocardial infarction.

Chapter 4

Time-Lapse Fluorescence Microscopy

in vitro

4. Time-lapse fluorescence microscopy

This section is dedicated to live-cell studies, using fluorescence microscopy to assess reactive oxygen species (ROS) in cells due to the metabolic stressor, and oxygen tension.

4.1. Live cell preparation and experimental protocol

4.1.1. Retina endothelial cells and pericytes under different glucose conditions

Retina pericytes (RPC) and endothelial cells (REC) were isolated from C57BL/6 J Immorto mice and cultured, as previously described [162]. For imaging, RECs were passed and cultured on gelatin-coated, while RPCs were cultured on uncoated, 8-well chamber slide (4×104 cells/well, LabTekII, ThermoFisher) and incubated in low glucose (normal glucose; NG) growth medium for 24 h. To determine the effect of HG on cellular metabolic resistivity and ROS production, cells were grown in medium with different glucose concentrations. Following 24 h of incubation, cells were fed in 2 to 3 wells with high glucose (HG, 30 mM) medium, 2 to 3 wells with normal glucose (NG, 5 mM) medium, and 2 to 3 wells with D-glucose (5 mM) plus L-glucose (25 mM) for osmolarity control (OS) for 3 days. Following exposure to various glucose conditions, live cells were imaged using fluorescence microscopy. Before imaging, cells were subjected to nuclei staining, and during the imaging, the intracellular ROS level was determined by a mitochondrial-targeted red fluorescence probe, MitoSOX. All experiments were performed with cells between passages 9 to 11. To measure the mitochondrial ROS production rate, and hence the metabolic resistivity of REC and RPC, cells were stained with 400 nM MitoSOX (Invitrogen M36008; excitation/emission: 510/580 nm) during the experiment. MitoSOX was kept in the medium while imaging. To maintain the focus of imaging, the nuclei of the cells were also stained before imaging

67

with 200 nM Hoechst (Life technologies H1399, excitation/emission: UV/blue) and incubated in medium containing Hoechst for 30 min. Following incubation, the cells were rinsed twice with Hank's Balanced Salt Solution (HBSS, Life Technologies 14025092). After washing, HBSS was added for subsequent fluorescent imaging. Hoechst stains nuclei, whereas MitoSOX stains mitochondria ROS upon oxidation under appropriate excitation.

4.1.2. Lung endothelial cells under hypoxia

FPAECs were isolated from the normal lamb lungs. Two groups of cells were examined. The first group of cells was exposed to 2hr 3% hypoxia prolonged to an hour of fluorescence time-lapse microscopy. For the second group, the same experimental protocol of microscopy was used except they were in normoxic gas conditions. The fluorescence images of both groups of cells were captured, and intensity profiles [40] of cells were plotted to compare their mitochondrial activity. FPAECs were isolated from the normal lamb lungs and incubated in the 8-well bottom glass dishes in 5% CO2 and 37ºC for both culturing and imaging. The growth medium included 1X antibiotic/antimycotic (AB/AM) and 20% fetal bovine serum (FBS) diluted in ATCC Dulbecco's Modified Eagle's Medium (DMEM). Before each experiment, the cells were loaded with a blue fluorescent dye (250 nM Hoechst) for probing nuclei and were incubated for 20 minutes. After washing the cells twice with Hank's Balanced Salt Solution (HBSS), HBSS was added to the dish for subsequent fluorescent imaging. For hypoxic cells, before starting microscopy, the cells were incubated in hypoxia (3% O_2, 5% CO_2) and 37ºC for 2 hours. The incubation initiated with hypoxic HBSS previously bubbled with N_2 gas. This hypoxic condition was kept during microscopy.

The experimental protocol was designed as previously described in Ghanian et al [40]. Fluorescent images were captured every 1 minute. After 10 minutes of baseline imaging, the cells were loaded with Mito-SOX (250 nM). The nanomolar concentration of Mito-SOX is used to make

sure that there is no direct effect of Mito-SOX on metabolism of cells [163]. PCP (5 µM) was added 20 minutes later (30 min of protocol time) to study the dynamic of ROS production in the mitochondria as indicated by fluorescence intensity. PCP concentration was chosen to ensure that the cell's viability is not affected.

4.2. Microscope system

In this study, a Nikon Ti-E inverted fluorescence microscope was used (Figure 22). It has an environmental control chamber (37°C, a gas mixture of 95% O2 and 5% CO2) around it to make an incubation environment for the live-cells over time. It has four fluorescent interchangeable filter cubes in addition to the standard DIC and bright-field channels. An overhead halogen lamp and a mercury arc lamp are used for illumination in bright field channel and fluorescent channels, respectively. Mercury lamp's intense peaks in the ultraviolet spectrum are suitable to excite
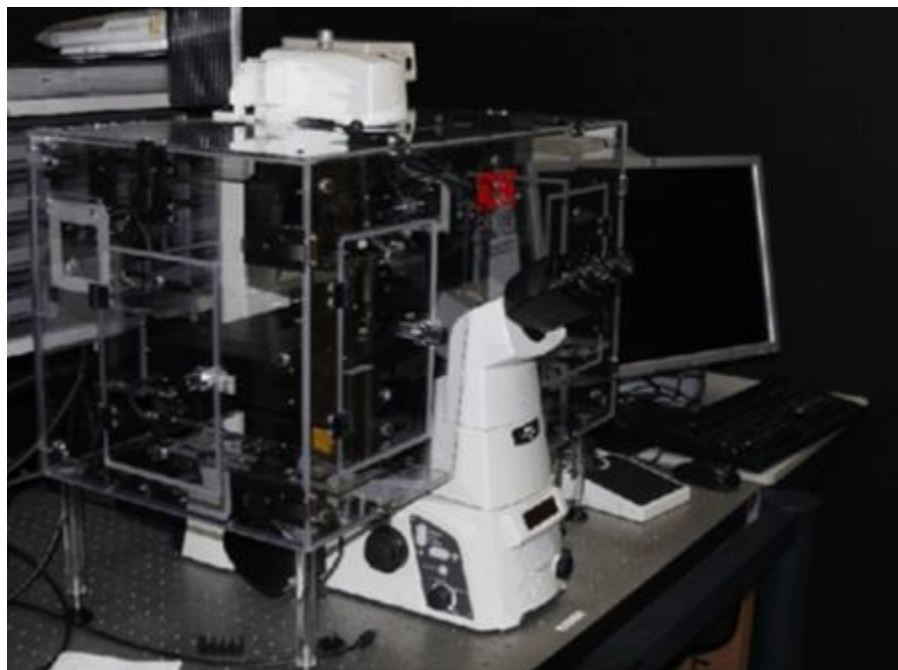
Figure 22: Time-lapse fluorescent microscope system.

fluorophores. Magnification of 20× was chosen for image acquisition due to the need for capturing a high level of image detail while maintaining a large field of view. A charge-coupled device camera (Q-imaging, Aqua Exi, 14 bit, 6.45 μm pixel) captures the images with proper exposure time and gain set to ensure that the images are in the dynamic range of the camera while avoiding saturation and photo-bleaching. The excitation and emission spectra for the blue channel are 340-380 nm and 528-553 nm, respectively, while for the red channel, the excitation and emission spectra are 435-485 nm and 590-650 nm, respectively.

4.3.   Image processing and quantifications

The cells were segmented from the first slide of the time-lapse stack using the previously described segmentation algorithm [8]. The intensity of the segmented images in the red channel is calculated and plotted as the intensity profile over time. These graphs show the dynamics of ROS production in red channel.

The intensity profile was driven in the following steps. First, the intensity profile of the background was subtracted from the intensity profile of the cells. Then, the slope of the intensity profiles after administration of PCP (between 30 min and 45 min) was calculated by linear curve-fitting. This slope represents the rate of mitochondrial ROS production [106, 164].

4.4.   Results

4.4.1.   Metabolic sensitivity of retinal pericytes under high glucose condition.

In microscopic images captured in fluorescent channels, the nuclei were targeted by Hoechst in blue, and mitochondrial compartments were detected by MitoSOX in red. Panels a and b in Figure

23 show the overlay of the blue and red fluorescent markers in REC and RPC. Panels c and d in Figure 23 demonstrate changes in the fluorescence intensity of the REC (red profiles) and RPC (blue profiles) overtime under NG and HG. Panel c and d compare the metabolic resistivity of REC with RPC under NG and HG. Figure 23(c) shows that the metabolic properties of REC and RPC were different even at a normal glucose level. However, under high glucose conditions (Figure 23(d)), RPC produced more mitochondrial ROS while REC did not exceed the level reached in NG.
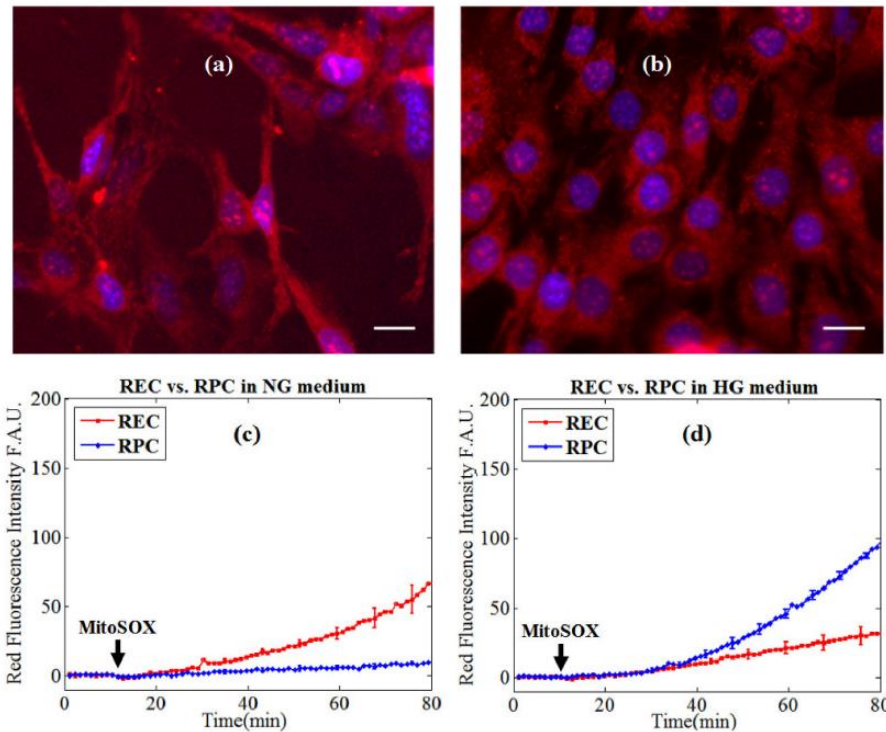
Figure 23: The fluorescence intensity of the REC and RPC over time under NG and HG. Top panels: Overlay of the blue (Hoechst) and MitoSOX red fluorescence signals. Note that the scale bar represents 32 μm (~100 pixels); a) retinal endothelial cells (REC); b) retinal pericytes (RPC). Bottom panels: Comparing resistivity of REC and RPC under normal glucose (NG) and high glucose (HG) conditions; c) The fluorescence intensity profiles of REC and RPC in NG; d) Fluorescence intensity profiles of REC and RPC in HG.

The ROS initiation rates right after the addition of PCP (t = 30 min) in REC and RPC exposed to the different glucose conditions were compared statistically in Figure 24. Bar graphs in Figure 24 demonstrate significant changes in the ROS initiation rate of the REC group (red bars) compared
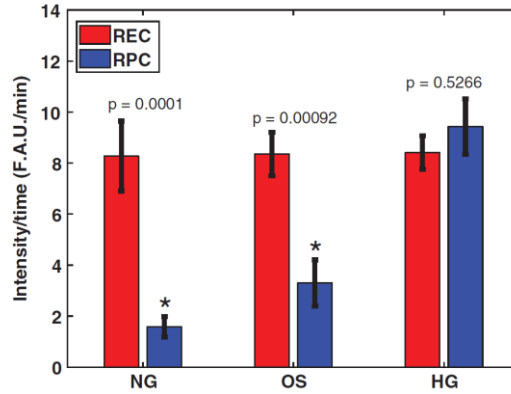
Figure 24: Bar graphs demonstrate the statistical analysis (mean±SE) of ROS initiation rate (at 30 min) induced by PCP in live retina cells in NG, OS, and HG exposures (n = 6/group).

with the RPC group (blue bars) in response to different glucose conditions. The results show that ROS initiation rate in uncoupled RPC was significantly smaller than that of uncoupled REC under NG and OS conditions, but not under HG condition. Since OS was used to account for changes in the osmolality of HG and to separate the effects of glucose from osmolality, OS-NG addresses the changes in the ROS initiation rate due to osmolality. ROS initiation rates in uncoupled REC appeared with no significant changes, while uncoupled RPC showed a significant increase of 7.33 times under high glucose conditions.

4.4.2. Lung endothelial cells under hypoxia

The panel in Figure 25 corresponds to the average background-subtracted intensity profiles of the normoxic (blue curve) and hypoxic (red curve) cells. For both hypoxic and normoxic conditions, n=6 wells of FPEACs were imaged. Under hypoxic conditions, the slope of the red intensity profile was 1.10 ± 0.06 at the time of the addition of uncoupler (PCP), while under normoxia, PCP increased the slope by 2.09 ± 0.22 degree. As Figure 25 shows, PCP induced cellular ROS production significantly greater in normoxia when compared with hypoxia.
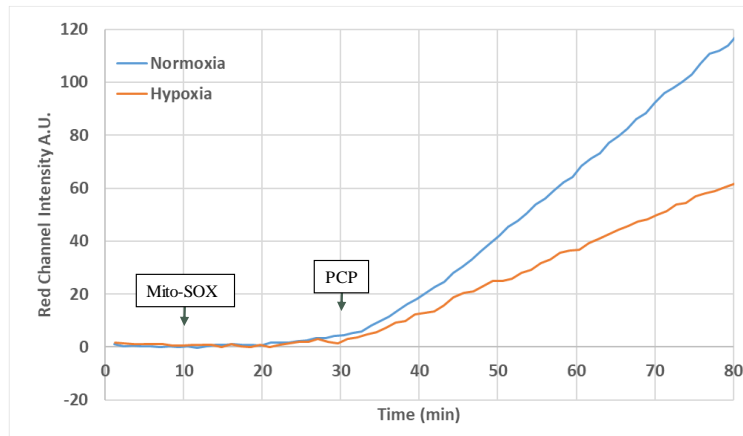
Figure 25: Dynamics of red fluorescence intensity of cells under hypoxia and normoxia.

4.5. Discussion

The fluorescence time-lapse microscopy using nano-molar Mito-SOX can be used as a tool for real-time monitoring of the mitochondrial ROS production in live cells. This approach could have far-reaching implications for the assessment of ROS in physiology and pathophysiology. The dynamics of ROS production was determined overtime before, during, and after cells were incubated with PCP. This approach has been utilized in two studies.

I investigated the metabolic resistivity of two types of retinal vascular cells, EC and PC. To gain detailed insight into preferential bioenergetic sources impacted in REC and RPC, the ROS generation rate was studied under different glucose conditions, including HG. A major finding of this study regarding the different metabolic activity of REC and RPC is that under normal glucose conditions, REC and RPC exhibited different sensitivity to mitochondrial stressors. Under the HG condition, only the metabolic resistivity of RPC was affected by the increase in glucose levels and showed an increase in the ROS production rate. These results may justify the sensitivity of RPC to HG condition and/or diabetes [105].

73

Figure 23(c) shows that the metabolic properties of REC and RPC are different even at a normal glucose level. However, under high glucose (Figure 23(d)), RPC generated more mitochondrial ROS while REC did not exceed the levels reached in normal glucose. These results suggest that high glucose has a minimal effect on the metabolic activity of REC and their mitochondrial ROS production. The enhanced expression and activity of endothelial nitric oxide synthase (eNOS) may explain the inhibitive effect on mitochondrial ROS production in REC under HG. eNOS, which is expressed in EC [165], is responsible for most of the vascular nitric oxide (NO) production. NO mediates vasodilation by acting on perivascular supporting cells and can act as a scavenger of superoxide anions maintaining a cellular balance of redox signaling in the endothelium in NG levels [166]. Huang et al. reported an enhanced expression of eNOS in retinal EC under HG [104]. The enhanced eNOS activity, and hence increased bioavailability of NO [167, 168]. is consistent with the decreased generation rate of superoxide in retinal EC under HG. Moreover, the increased production of eNOS is shown to prevent apoptosis of EC under HG [169]. This may justify the decreased rate of apoptosis in REC compared to the RPC due to diabetes. However, the potential differences in glucose uptake in these cells cannot be ruled out.

We found that mitochondrial uncoupling by PCP increased ROS production in both REC and RPC. PCP binds to mitochondrial proteins and inhibits mitochondrial ATPase activity. Thus, both the formation of ATP and the release of energy to the cell from the breakdown of ATP to ADP are prevented. Electron transport is not inhibited by PCP, although reactions dependent on available high-energy bonds, such as oxidative and glycolytic phosphorylation, are affected. Although glycolysis is the main source of ATP in cultured REC, the higher level of oxidative stress in uncoupled REC indicates that glycolysis and oxidative phosphorylation are linked for ATP production. Cultured RECs are highly dependent on ATP for their activity. Since PCP inhibits

mitochondrial ATPase activity, RECs activate a mechanism to compensate for ATP and increase the ETC activity in the uncoupled chain [170]. This mechanism expedites the electron transfer through the chain leading to the generation of more ROS. This does not appear to be the case for RPC. Lack of proton gradient for phosphorylation and polarized membrane potential activates a mechanism to compensate for the uncoupling effect of PCP, by increasing proton pumping and respiration, to reestablish the proton gradient. Ironically, the increase in the activity of the complex I and II in the uncoupled chain [106] increases electron transfer along the electron transport chain. As a result, increases electron leak to oxygen leading to superoxide production [171-174].

Although RPC and REC are differentially affected by metabolic stress conditions, most likely because of their preferential bioenergetic sources, both cell types showed a higher rate of ROS production under stress. However, RPCs were more resistant to mitochondrial stress under normal glucose conditions when compared with REC. Right after incubation with a mitochondrial stressor (PCP), REC showed a significantly greater increase in the rate of ROS production when compared with RPC. These results suggest that both inhibited REC and RPC metabolic activities, at least under normal glucose conditions, may depend on the integrity of mitochondrial respiration. However, the reason for enhanced ROS generation in REC is not clear and requires further delineation of the bioenergetic pathways utilized by these cells. These may be linked to the oxygen and glucose levels. The use of different glucose and/or oxygen levels provides additional insight into the preferential bioenergetic pathway(s) utilized by these cells. However, the preferential utilization of glycolysis by REC as the major bioenergetic source suggests that REC may also depend on some intermediate metabolite(s), including those generated by isocitrate dehydrogenase 1, during respiration to maintain the cellular reductive state. Thus, attenuation of respiration could

significantly reduce the level of such metabolite(s) and result in increased accumulation of ROS in REC.

Our results revealed a higher sensitivity of the RPC compared to REC under HG conditions. While under normal glucose conditions, the metabolic resistivity of RPC was greater than REC, the metabolic resistivity of RPC significantly decreased under HG condition triggering the pre-apoptosis process of the RPC. ROS overproduction in this stage leads to a higher level of oxidative stress [175], which is known as an underlying mechanism causing the apoptosis of vascular cells associated with diabetic retinopathy. However, it remains unclear how the HG condition leads to REC apoptosis. We have observed that the incubation of REC under high glucose does not affect their rate of apoptosis [104]. Other studies suggest an indirect role for HG mediated REC death in retinal vasculature [176]. Thus, deterioration of vascular structure due to RPC loss may contribute to the demise and dysfunction of REC in the retinal vasculature.

The disparity seen between RPC and REC may be also explained by the fact that mitochondrial oxygen consumption is compromised in RPC exposed to HG. Therefore, the extracellular acidification levels may be an influential factor in RPC. Trudeau et al. reported an increase in extracellular acidification levels in REC, possibly to compensate for HG-induced decreased mitochondrial oxygen consumption [177]. This compensation helps EC to maintain the rate of ROS generation with HG exposure without a significant increase compared to NG condition. Interestingly, the inability of the RPC to compensate for the HG induced decrease in mitochondrial oxygen consumption, due to the significant decrease in extracellular acidification [177], indicates an increased susceptibility of the RPC to HG.

Moreover, the differential transport of glucose between the two cell types may also illustrate their different metabolic resistivity under HG conditions. Previous reports have shown that HG

downregulates Glut1 activity in PC but not in EC [178]. Thus, different extracellular acidification levels and possibly glycolytic levels may indirectly lead to the differential alternation of ROS production rate and metabolic resistivity in RPC and REC in response to HG exposure. Further research is required to indicate the mechanisms for the observed difference between the two cell types.

Chapter 5

Conclusion and Future Direction

5. Conclusion and future direction

This thesis has illustrated how different optical techniques are developed and implemented to quantify the effect of injuries on the physiology and structure of multiple organs. The novel approaches presented in this thesis have shown the ability for the quantitative detection of mitochondrial and vascular dysfunction due to injuries and stress conditions in tissue and cells.

The following four sub-sections present the conclusions and outlook for each optical imaging technique.

5.1. *In vivo* fluorescence imaging

I developed a device that provides an optical metabolic marker, redox ratio, which is sensitive to the impaired diabetic wound healing, suggesting the diagnostic potential of optical imaging systems for clinical wound care. The *in vivo* fluorescence imager has also successfully distinguished the mitigation effect of FR-PBM, confirming the application of this technique in detecting the effect of wound healing strategies.

Apart from the expansion of application to a wide variety of wounds in preclinical studies, a prototype is also designed that can be used in clinical wounds to pilot the diagnostic potential of this novel and emerging technology. The system is non-invasive, non-contact, and portable to hospitals and clinics for in situ wound assessment. Such an investigation would be relevant to examine the efficacy of wound healing interventions targeting ROS and mitochondrial dysfunction during diabetic wound healing.

5.2. 3D fluorescence cryo-imaging

The results of 3D cryo-imaging studies demonstrate the quantitative capability of this device to measure the mitochondrial redox state. Optical redox imaging yields a direct analysis of the cellular metabolic state within the mitochondrial compartment of the multiple organs from the animal model of diabetes, uninephrectomy, radiation induce injuries, and ischemia-reperfusion injuries, which have not previously been reported.

3D optical cryo-imaging is helpful to study the effect of disease and injuries on wound biopsies, kidney, heart, and liver metabolism. Our results revealed that an increase of oxidative stress may be an important signal for renal hypertrophy following UNX driven by enhanced mitochondrial energy production of the remaining kidney. We also observed a significant difference in the redox state of mitochondria between the irradiated and non-irradiated kidneys. Furthermore, lisinopril restored mitochondrial redox state after 13Gy single fraction radiation. However, we did not observe any significant difference in the redox state of mitochondria between the irradiated and nonirradiated hearts, and irradiation did not lead to aggravated reperfusion injury. The mitochondrial redox state can also be successfully served as a quantitative marker of hepatic IR injury.

These results will inspire future studies that will allow researchers to establish a diagnostic tool for early detection of different diseases, and to study a correlation between disease progression and changes in the RR levels as a marker of oxidative stress. Furthermore, the studies presented in this thesis set the stage for future studies of using 3D cryo-imaging of mitochondrial redox states to characterize disease progression in various diseases and injuries to evaluate mitochondria-targeted drug regimens that diminish oxidative stress.

5.3. Vascular metabolic imaging

Autofluorescence metabolic imaging has been used to image mitochondrial metabolites (NADH and FAD). However, it has not been used to report anatomical aspects of organs such as the vasculature. I have developed a 3-dimensional (3D) vascular segmentation technique, leveraging intrinsic fluorescence images of whole organs. This novel technique provides 3D vascular-metabolic imaging (VMI) without the need for a contrast agent for the first time. VMI allows the simultaneous acquisition of vasculature and metabolism in multiple organs in rats. The vasculature from genetically engineered rats expressing endothelial-specific red fluorescent protein TdTomato, demonstrated a high overlap with VMI, confirming the identification of vasculature by VMI. Lung airways perfused with a fluorescent dye and showed no overlap of signal with VMI. The VMI also showed convincing evidence for the "minimum work" hypothesis in the vascular network by following Murray's law. Finally, I utilized a partial body irradiation rat model for a proof-of-concept to detect radiation-induced vascular regression by VMI.

The pre-clinical vascular-metabolic imaging has the capacity to explore the pathophysiology in rodents and study the rodent models of whole organ injuries. Optical metabolic imaging has been used in this application for several years, and by using the proposed segmentation technique, another key hallmark of injury (vascular quantification) would significantly help in understanding the underlying effects of injuries in multiple organs. Another straight-forward application of vascular-metabolic is in imaging tumors to study metabolism and vascularization of drugs and radiotherapy in various animal models of cancer. Also, the vascular-metabolic imaging offers the attractive options in hearts, such as the studies of the interaction of metabolic, vascular,

and mechanical (that is, tissue elasticity) of myocardial infarction are currently underway in our laboratory.

5.4. Time-lapse fluorescence microscopy

Using time-lapse fluorescence microscopy, the dynamics of $O_2^{\bullet-}$ production was quantified under different simulated oxygen and metabolic stress conditions in intact live cells. Utilizing fluorescence microscopy, ROS dynamics were assessed in retina cells due to metabolic stress (high glucose, diabetes) and in PAECs due to oxygen tension (hypoxia, IR). ROS-mediated injuries, including hypoxia and IR, were modeled with the hypoxic environment in microscope top incubator.

Metabolic modulation and IR demonstrated greater mitochondrial superoxide production rates. However, uncoupled ETC in hypoxic conditions showed that lower concentration of ambient oxygen decreases the severity of the metabolic stress and mitochondrial dysfunction. This phenomenon shows the potential of hypoxia therapy for lung injuries, including hyperoxia and PPHN, and it is our next step to further expand this research.

These results show that the approach has far-reaching implications for the assessment of ROS in physiology and pathophysiology. Measuring the $O_2\bullet-$ dynamics, particularly in the *early phase* of the stress response, could lead to future studies extending the approach to situations that would allow us to establish a diagnostic tool for assessing the role of the mitochondrial ROS in different diseases. It is intended for future studies to monitor the behavior of the injured PAECs under long hypoxic conditions followed by hyperoxic conditions to investigate the effect of the ambient oxygen concentrations on the severity of the lung injuries. Studying a hypoxic condition

followed by a hyperoxic condition is advantageous in another aspect as well since it simulates the birth transition of the fetal lung for the PAECs. The immature lung of the fetus that develops in moderate hypoxia in-utero might be more vulnerable to another injury in the relatively hyperoxic extra-uterine environment.

References

[1]   L. V. Wang and H.-i. Wu, *Biomedical optics: principles and imaging*. John Wiley & Sons, 2012.

[2]   S. S. Virani *et al.*, "Heart Disease and Stroke Statistics 2020 Update. A Report From the American Heart Association.," *Circulation,* vol. 141, no. 9, pp. e139-e596, 2020.

[3]   S. Hedgire and B. Ghoshhajra, "Vascular imaging," *Cardiovascular Diagnosis and Therapy,* vol. 9, no. Suppl 1, p. S1, 2019.

[4]   D. A. Nordsletten, S. Blackett, M. D. Bentley, E. L. Ritman, and N. P. Smith, "Structural morphology of renal vasculature," *American Journal of Physiology-Heart and Circulatory Physiology,* vol. 291, no. 1, pp. H296-H309, 2006.

[5]   H. Tomiyama and A. Yamashina, "Non-invasive vascular function tests," *Circulation Journal,* pp. 0911120515-0911120515, 2010.

[6]   K. Kimura, A. Tojo, H. Matsuoka, and T. Sugimoto, "Renal arteriolar diameters in spontaneously hypertensive rats. Vascular cast study," *Hypertension,* vol. 18, no. 1, pp. 101-110, 1991.

[7]   A. R. Kee, T. Y. Wong, and L. J. Li, "Retinal vascular imaging technology to monitor disease severity and complications in type 1 diabetes mellitus: A systematic review," *Microcirculation,* vol. 24, no. 2, p. e12327, 2017.

[8]   Z. Ghanian *et al.*, "Quantitative Assessment of Retinopathy Using Multi-parameter Image Analysis," *Journal of medical signals and sensors,* vol. 6, no. 2, p. 71, 2016.

[9]   T. Mirabella *et al.*, "3D-printed vascular networks direct therapeutic angiogenesis in ischaemia," *Nature biomedical engineering,* vol. 1, no. 6, pp. 1-8, 2017.

[10]   D. Scoles *et al.*, "In-vivo imaging of retinal nerve fiber layer vasculature: imaging-histology comparison," *BMC ophthalmology,* vol. 9, no. 1, p. 9, 2009.

[11]   M. Cano Sanchez, S. Lancel, E. Boulanger, and R. Neviere, "Targeting oxidative stress and mitochondrial dysfunction in the treatment of impaired wound healing: A systematic review," *Antioxidants & redox signaling,* vol. 7, no. 8, p. 98, 2018.

[12]   C. Di Mario *et al.*, "Detection and characterization of vascular lesions by intravascular ultrasound: an in vitro study correlated with histology," *Journal of the American Society of Echocardiography,* vol. 5, no. 2, pp. 135-146, 1992.

[13]   K. Tainaka *et al.*, "Whole-body imaging with single-cell resolution by tissue decolorization," *Cell,* vol. 159, no. 4, pp. 911-924, 2014.

[14]   J. Epah *et al.*, "3D imaging and quantitative analysis of vascular networks: a comparison of ultramicroscopy and micro-computed tomography," *Theranostics,* vol. 8, no. 8, p. 2117, 2018.

[15]   G. Hong *et al.*, "Multifunctional in vivo vascular imaging using near-infrared II fluorescence," *Nature medicine,* vol. 18, no. 12, p. 1841, 2012.

[16]   G. Pastor *et al.*, "A general protocol of ultra-high resolution MR angiography to image the cerebro-vasculature in 6 different rats strains at high field," *Journal of neuroscience methods,* vol. 289, pp. 75-84, 2017.

[17]   C. Errico *et al.*, "Ultrafast ultrasound localization microscopy for deep super-resolution vascular imaging," *Nature,* vol. 527, no. 7579, pp. 499-502, 2015.

[18]   E. L. Ritman, "Current status of developments and applications of micro-CT," *Annual review of biomedical engineering,* vol. 13, pp. 531-552, 2011.

[19] A. Ertürk *et al.*, "Three-dimensional imaging of solvent-cleared organs using 3DISCO," *Nature protocols,* vol. 7, no. 11, p. 1983, 2012.

[20] D. Hanahan and R. A. Weinberg, "Hallmarks of cancer: the next generation," *cell,* vol. 144, no. 5, pp. 646-674, 2011.

[21] J. Provost *et al.*, "Simultaneous positron emission tomography and ultrafast ultrasound for hybrid molecular, anatomical and functional imaging," *Nature biomedical engineering,* vol. 2, no. 2, pp. 85-94, 2018.

[22] T. Beyer *et al.*, "A combined PET/CT scanner for clinical oncology," *Journal of nuclear medicine,* vol. 41, no. 8, pp. 1369-1379, 2000.

[23] H. Lodish *et al.*, *Molecular cell biology*. Macmillan, 2008.

[24] D. C. Rizzo, *Fundamentals of anatomy and physiology*. Cengage Learning, 2015.

[25] N. A. Campbell, B. Williamson, and R. J. Heyden, "Biology: Exploring Life. Boston, Massachusetts: Pearson Prentice Hall," ISBN 0-13-250882-6, 2006.

[26] T. M. Buttke and P. A. J. I. t. Sandstrom, "Oxidative stress as a mediator of apoptosis," vol. 15, no. 1, pp. 7-10, 1994.

[27] A. B. Fisher, "Intermediary metabolism of the lung," *Environmental health perspectives,* vol. 55, pp. 149-158, 1984.

[28] X. Wen *et al.*, "Deconvoluting the role of reactive oxygen species and autophagy in human diseases," vol. 65, pp. 402-410, 2013.

[29] A. Boveris and B. J. B. J. Chance, "The mitochondrial generation of hydrogen peroxide. General properties and effect of hyperbaric oxygen," vol. 134, no. 3, pp. 707-716, 1973.

[30] H. NOHL and D. HEGNER, "Do mitochondria produce oxygen radicals in vivo?," *European Journal of Biochemistry,* vol. 82, no. 2, pp. 563-567, 1978.

[31]   B. Halliwell and J. M. Gutteridge, *Free radicals in biology and medicine*. Oxford University Press, USA, 2015.

[32]   P. M. Abou-Sleiman, M. M. Muqit, and N. W. Wood, "Expanding insights of mitochondrial dysfunction in Parkinson's disease," *Nature Reviews Neuroscience,* vol. 7, no. 3, p. 207, 2006.

[33]   A. H. de Mello, A. B. Costa, J. D. G. Engel, and G. T. Rezin, "Mitochondrial dysfunction in obesity," *Life sciences,* vol. 192, pp. 26-32, 2018.

[34]   I. G. Onyango, J. Dennis, and S. M. Khan, "Mitochondrial dysfunction in Alzheimer's disease and the rationale for bioenergetics based therapies," *Aging and disease,* vol. 7, no. 2, p. 201, 2016.

[35]   C.-C. Hsu, L.-M. Tseng, and H.-C. Lee, "Role of mitochondrial dysfunction in cancer progression," *Experimental biology and medicine,* vol. 241, no. 12, pp. 1281-1295, 2016.

[36]   H. A. Funes, A. Blas-Garcia, J. V. Esplugues, and N. Apostolova, "Efavirenz alters mitochondrial respiratory function in cultured neuron and glial cell lines," *Journal of Antimicrobial Chemotherapy,* vol. 70, no. 8, pp. 2249-2254, 2015.

[37]   M. D. Brand and D. G. Nicholls, "Assessing mitochondrial dysfunction in cells," *Biochemical Journal,* vol. 435, no. 2, pp. 297-312, 2011.

[38]   K. E. Conley, A. S. Ali, B. Flores, S. A. Jubrias, and E. G. Shankland, "Mitochondrial NAD(P)H In vivo: Identifying Natural Indicators of Oxidative Phosphorylation in the 31P Magnetic Resonance Spectrum," (in English), *Frontiers in Physiology,* Original Research vol. 7, no. 45, 2016.

[39]   V. Ntziachristos, "Going deeper than microscopy: the optical imaging frontier in biology," *Nature methods,* vol. 7, no. 8, p. 603, 2010.

[40] Z. Ghanian, "Quantitative Optical Studies of Oxidative Stress in Rodent Models of Eye and Lung Injuries," PhD, Electrical Engineering, University of Wisconsin Milwaukee, 2016.

[41] M. A. Wall *et al.*, "Metabolic Imaging Approaches: Optical Imaging," in *Imaging and Metabolism*: Springer, 2018, pp. 99-126.

[42] M. F. la Cour *et al.*, "Optical imaging for the assessment of hepatocyte metabolic state in ischemia and reperfusion injuries," *Biomedical Optics Express,* vol. 8, no. 10, pp. 4419-4426, 2017.

[43] S. A. Lewis *et al.*, "The effect of Tmem135 overexpression on the mouse heart," vol. 13, no. 8, p. e0201986, 2018.

[44] M. F. la Cour *et al.*, "Optical metabolic imaging of irradiated rat heart exposed to ischemia-reperfusion injury," *BIOMEDO,* vol. 23, no. 1, pp. 1-9, 2018.

[45] M. Aldakkak, D. F. Stowe, J. S. Heisner, M. Spence, and A. K. Camara, "Enhanced Na+/H+ exchange during ischemia and reperfusion impairs mitochondrial bioenergetics and myocardial function," *Journal of cardiovascular pharmacology,* vol. 52, no. 3, p. 236, 2008.

[46] H.-H. Lu *et al.*, "Molecular imaging of ischemia and reperfusion in vivo with mitochondrial autofluorescence," *Analytical chemistry,* vol. 86, no. 10, pp. 5024-5031, 2014.

[47] M. Ranji *et al.*, "Optical Cryoimaging Reveals a Heterogeneous Distribution of Mitochondrial Redox State in ex vivo Guinea Pig Hearts and Its Alteration During Ischemia and Reperfusion," *IEEE Journal of Translational Engineering in Health and Medicine,* vol. 4, pp. 1-10, 2016.

[48] M. Ranji *et al.*, "Quantifying acute myocardial injury using ratiometric fluorometry," *Ieee Transactions on Biomedical Engineering,* vol. 56, no. 5, pp. 1556-1563, 2009.

[49] R. Sepehr *et al.*, "Optical Imaging of Lipopolysaccharide-Induced Oxidative Stress in Acute Lung Injury from Hyperoxia and Sepsis," (in eng), *J Innov Opt Health Sci,* vol. 6, no. 3, p. 1350017, Jul 1 2013.

[50] S. Maleki, R. Sepehr, K. Staniszewski, N. Sheibani, C. M. Sorenson, and M. Ranji, "Mitochondrial redox studies of oxidative stress in kidneys from diabetic mice," (in eng), *Biomed Opt Express,* vol. 3, no. 2, pp. 273-81, Feb 1 2012.

[51] S. Maleki *et al.*, "Optical imaging of mitochondrial redox state in rodent model of retinitis pigmentosa," *BIOMEDO,* vol. 18, no. 1, p. 016004, 2013.

[52] Z. Ghanian, S. Maleki, S. Park, C. M. Sorenson, N. Sheibani, and M. Ranji, "Organ specific optical imaging of mitochondrial redox state in a rodent model of hereditary hemorrhagic telangiectasia-1," (in eng), *J Biophotonics,* vol. 7, no. 10, pp. 799-809, Oct 2014.

[53] F. Salehpour *et al.*, "Effects of p67phox on the mitochondrial oxidative state in the kidney of Dahl salt-sensitive rats: optical fluorescence 3-D cryoimaging," (in eng), *Am J Physiol Renal Physiol,* vol. 309, no. 4, pp. F377-82, Aug 15 2015.

[54] A. W. Cowley, Jr. *et al.*, "Evidence of the Importance of Nox4 in Production of Hypertension in Dahl Salt-Sensitive Rats," (in eng), *Hypertension,* vol. 67, no. 2, pp. 440-50, Feb 2016.

[55] Z. Zhang *et al.*, "Redox ratio of mitochondria as an indicator for the response of photodynamic therapy," vol. 9, no. 4, pp. 772-779, 2004.

[56]   H. N. Xu *et al.*, "Chop Therapy Induced Mitochondrial Redox State Alteration in Non-Hodgkin's Lymphoma Xenografts," (in eng), *J Innov Opt Health Sci,* vol. 6, no. 2, p. 1350011, Apr 2013.

[57]   J. H. Ostrander *et al.*, "Optical redox ratio differentiates breast cancer cell lines based on estrogen receptor status," vol. 70, no. 11, pp. 4759-4766, 2010.

[58]   L. Z. Li, H. N. Xu, M. Ranji, S. Nioka, and B. Chance, "Mitochondrial Redox Imaging for Cancer Diagnostic and Therapeutic Studies," (in eng), *J Innov Opt Health Sci,* vol. 2, no. 4, pp. 325-341, Oct 2009.

[59]   S. Mehrvar, M. F. l. Cour, M. Medhora, A. K. S. Camara, and M. Ranji, "Optical metabolic imaging for assessment of radiation-induced injury to rat kidney and mitigation by lisinopril," *Annals of biomedical engineering,* vol. 47, no. 7, 2019.

[60]   M. Niwayama *et al.*, "A 200-channel imaging system of muscle oxygenation using CW near-infrared spectroscopy," *IEICE TRANSACTIONS on Information and Systems,* vol. 85, no. 1, pp. 115-123, 2002.

[61]   M. MasoudiMotlagh *et al.*, "Monitoring hemodynamic changes in stroke-affected muscles using near-infrared spectroscopy," *Journal of Rehabilitation and Assistive Technologies Engineering,* vol. 2, p. 2055668315614195, 2015.

[62]   G. Yu *et al.*, "Time-dependent blood flow and oxygenation in human skeletal muscles measured with noninvasive near-infrared diffuse optical spectroscopies," *BIOMEDO,* vol. 10, no. 2, pp. 024027-02402712, 2005.

[63]   P. Kadamati *et al.*, "Near-infrared spectroscopy muscle oximetry of patients with postural orthostatic tachycardia syndrome," vol. 11, no. 05, p. 1850026, 2018.

[64]   C. K. Sen, "Human wounds and its burden: an updated compendium of estimates," ed: Mary Ann Liebert, Inc., 2019.

[65]   S. a. Guo and L. A. DiPietro, "Factors affecting wound healing," *Journal of dental research,* vol. 89, no. 3, pp. 219-229, 2010.

[66]   T. J. Fahey III, A. Sadaty, W. G. Jones II, A. Barber, B. Smoller, and G. T. Shires, "Diabetes impairs the late inflammatory response to wound healing," *Journal of Surgical Research,* vol. 50, no. 4, pp. 308-313, 1991.

[67]   A. Terranova, "The effects of diabetes mellitus on wound healing," *Plastic surgical nursing: official journal of the American Society of Plastic and Reconstructive Surgical Nurses,* vol. 11, no. 1, pp. 20-25, 1991.

[68]   A. Raghav, Z. A. Khan, R. K. Labala, J. Ahmad, S. Noor, and B. K. Mishra, "Financial burden of diabetic foot ulcers to world: a progressive topic to discuss always," *Therapeutic advances in endocrinology and metabolism,* vol. 9, no. 1, pp. 29-31, 2018.

[69]   S. Enoch and D. J. Leaper, "Basic science of wound healing," *Surgery (Oxford),* vol. 26, no. 2, pp. 31-37, 2008.

[70]   D. M. Rojas-Canales, J. Y. Li, L. Makuei, and J. M. Gleadle, "Compensatory renal hypertrophy following nephrectomy: When and how?," *Nephrology,* vol. 24, no. 12, pp. 1225-1232, 2019.

[71]   E. MacKay, L. L. MacKay, and T. Addis, "The degree of compensatory renal hypertrophy following unilateral nephrectomy: I. The influence of age," *Journal of Experimental Medicine,* vol. 56, no. 2, pp. 255-265, 1932.

[72] Y. M. Barri, T. Parker III, Y. Daoud, and R. Glassock, "Definition of chronic kidney disease after uninephrectomy in living donors: what are the implications?," *J Transplantation,* vol. 90, no. 5, pp. 575-580, 2010.

[73] R. Z. Alicic, M. T. Rooney, and K. R. Tuttle, "Diabetic kidney disease: challenges, progress, and possibilities," *Clinical Journal of the American Society of Nephrology,* vol. 12, no. 12, pp. 2032-2045, 2017.

[74] A. D. Muzaale *et al.*, "Risk of end-stage renal disease following live kidney donation," *Jama,* vol. 311, no. 6, pp. 579-586, 2014.

[75] G. Mjøen *et al.*, "Long-term risks for kidney donors," *Kidney international,* vol. 86, no. 1, pp. 162-167, 2014.

[76] Y. Ki *et al.*, "Effect of Coenzyme Q10 on Radiation Nephropathy in Rats," *Journal of Korean Medical Science,* vol. 32, no. 5, pp. 757-763, 2017.

[77] L. A. Dawson *et al.*, "Radiation-Associated Kidney Injury," *International Journal of Radiation Oncology*Biology*Physics,* vol. 76, no. 3, pp. S108-S115, 2010.

[78] M. Watanabe Nemoto *et al.*, "Delayed renal dysfunction after total body irradiation in pediatric malignancies," *Journal of radiation research,* vol. 55, no. 5, pp. 996-1001, 2014.

[79] J. P. Williams *et al.*, "Animal Models for Medical Countermeasures to Radiation Exposure," *Radiation research,* vol. 173, no. 4, pp. 557-578, 2010.

[80] T. Fliedner, H. Dorr, and V. Meineke, "Multi-organ involvement as a pathogenetic principle of the radiation syndromes: a study involving 110 case histories documented in SEARCH and classified as the bases of haematopoietic indicators of effect," *The British journal of radiology,* no. 1, pp. 1-8, 2005.

[81] J. R. Cassady, "Clinical radiation nephropathy," *International Journal of Radiation Oncology* Biology* Physics,* vol. 31, no. 5, pp. 1249-1256, 1995.

[82] M. E. Robbins, W. Zhao, C. S. Davis, S. Toyokuni, and S. M. Bonsib, "Radiation-induced kidney injury: a role for chronic oxidative stress?," *Micron,* vol. 33, no. 2, pp. 133-141, 2002.

[83] M. Robbins and W. Zhao, "Chronic oxidative stress and radiation-induced late normal tissue injury: a review," *International journal of radiation biology,* vol. 80, no. 4, pp. 251-259, 2004.

[84] M. Medhora *et al.*, "Model development and use of ACE inhibitors for preclinical mitigation of radiation-induced injury to multiple organs," *Radiation research,* vol. 182, no. 5, pp. 545-555, 2014.

[85] B. L. Fish *et al.*, "Combined Hydration and Antibiotics with Lisinopril to Mitigate Acute and Delayed High-dose Radiation Injuries to Multiple Organs," *Health Physics,* vol. 111, no. 5, pp. 410-419, 2016.

[86] J. Kharofa, E. P. Cohen, R. Tomic, Q. Xiang, and E. Gore, "Decreased risk of radiation pneumonitis with incidental concurrent use of angiotensin-converting enzyme inhibitors and thoracic radiation therapy," *International Journal of Radiation Oncology* Biology* Physics,* vol. 84, no. 1, pp. 238-243, 2012.

[87] E. P. Cohen *et al.*, "Mitigation of late renal and pulmonary injury after hematopoietic stem cell transplantation," *International Journal of Radiation Oncology* Biology* Physics,* vol. 83, no. 1, pp. 292-296, 2012.

[88] C. G. Lenneman and D. B. Sawyer, "Cardio-Oncology An Update on Cardiotoxicity of Cancer-Related Treatment," *Circulation research,* vol. 118, no. 6, pp. 1008-1020, 2016.

[89]   B. J. Geist, S. Lauk, M. Bornhausen, and K.-R. Trott, "Physiologic consequences of local heart irradiation in rats," *International Journal of Radiation Oncology Biology Physics,* vol. 18, no. 5, pp. 1107-1113, 1990.

[90]   E. J. Hall and A. J. Giaccia, *Radiobiology for the radiologist*, Seventh edition ed. Philadelphia: Wolters Kluwer Health/Lippincott Williams and Wilkins (in English), 2012.

[91]   F. Stewart, "Mechanisms and dose–response relationships for radiation-induced cardiovascular disease," *Annals of the ICRP,* vol. 41, no. 3, pp. 72-79, 2012.

[92]   M. Boerma and M. Hauer-Jensen, "Preclinical research into basic mechanisms of radiation-induced heart disease," *Cardiology research and practice,* vol. 2011, 2010.

[93]   A. Sardaro, M. F. Petruzzelli, M. P. D'Errico, L. Grimaldi, G. Pili, and M. Portaluri, "Radiation-induced cardiac damage in early left breast cancer patients: risk factors, biological mechanisms, radiobiology, and dosimetric constraints," *Radiotherapy and Oncology,* vol. 103, no. 2, pp. 133-142, 2012.

[94]   M. J. Adams, P. H. Hardenbergh, L. S. Constine, and S. E. Lipshultz, "Radiation-associated cardiovascular disease," *Critical reviews in oncology/hematology,* vol. 45, no. 1, pp. 55-75, 2003.

[95]   E. Senkus-Konefka and J. Jassem, "Cardiovascular effects of breast cancer radiotherapy," *Cancer treatment reviews,* vol. 33, no. 6, pp. 578-593, 2007.

[96]   G. Gagliardi, I. Lax, A. Ottolenghi, and L. Rutqvist, "Long-term cardiac mortality after radiotherapy of breast cancer—application of the relative seriality model," *The British journal of radiology,* vol. 69, no. 825, pp. 839-846, 1996.

[97]   G. Pili *et al.*, "Geometric and dosimetric approach to determine probability of late cardiac mortality in left tangential breast irradiation: comparison between wedged beams and field-

in-field technique," *International Journal of Radiation Oncology* Biology* Physics,* vol. 81, no. 3, pp. 894-900, 2011.

[98] B. Seddon *et al.*, "Detection of defects in myocardial perfusion imaging in patients with early breast cancer treated with radiotherapy," *Radiotherapy and Oncology,* vol. 64, no. 1, pp. 53-63, 2002.

[99] C. García-Ruíz, A. Morales, and J. C. Fernández-Checa, "Oxidative Stress and Liver Ischemia–Reperfusion Injury," in *Studies on Hepatic Disorders*: Springer, 2015, pp. 149-170.

[100] I. Hilmi *et al.*, "The impact of postreperfusion syndrome on short-term patient and liver allograft outcome in patients undergoing orthotopic liver transplantation," vol. 14, no. 4, pp. 504-508, 2008.

[101] S.-M. Jeong, "Postreperfusion syndrome during liver transplantation," *Korean Journal of Anesthesiology,* vol. 68, no. 6, pp. 527-539, 2015.

[102] J. M. Cacicedo, S. Benjachareowong, E. Chou, N. B. Ruderman, and Y. Ido, "Palmitate-induced apoptosis in cultured bovine retinal pericytes: roles of NAD (P) H oxidase, oxidant stress, and ceramide," *Diabetes,* vol. 54, no. 6, pp. 1838-1845, 2005.

[103] R. A. Kowluru, "Diabetic retinopathy: mitochondrial dysfunction and retinal capillary cell death," *Antioxidants & redox signaling,* vol. 7, no. 11-12, p. 1581, 2005.

[104] Q. Huang and N. Sheibani, "High glucose promotes retinal endothelial cell migration through activation of Src, PI3K/Akt1/eNOS, and ERKs," (in eng), *Am J Physiol Cell Physiol,* vol. 295, no. 6, pp. C1647-57, Dec 2008.

[105] E. S. Shin *et al.*, "STAT1-mediated Bim expression promotes the apoptosis of retinal pericytes under high glucose conditions," (in eng), *Cell Death Dis,* vol. 5, p. e986, 2014.

[106] Z. Ghanian, G. G. Konduri, S. H. Audi, A. K. Camara, and M. Ranji, "Quantitative optical measurement of mitochondrial superoxide dynamics in pulmonary artery endothelial cells," *Journal of innovative optical health sciences,* vol. 11, no. 01, p. 1750018, 2018.

[107] B. Chance, B. Schoener, R. Oshino, F. Itshak, and Y. Nakase, "Oxidation-reduction ratio studies of mitochondria in freeze-trapped samples. NADH and flavoprotein fluorescence signals," *Journal of Biological Chemistry,* vol. 254, no. 11, pp. 4764-4771, 1979.

[108] M. Medhora *et al.*, "Delayed Effects of Acute Radiation Exposure (Deare) in Juvenile and Old Rats: Mitigation by Lisinopril," 2019.

[109] E. R. Jacobs *et al.*, "Cardiac Remodeling and Reversible Pulmonary Hypertension During Pneumonitis in Rats after 13-Gy Partial-Body Irradiation with Minimal Bone Marrow Sparing: Effect of Lisinopril," 2019.

[110] M. Medhora *et al.*, "Whole-thorax irradiation induces hypoxic respiratory failure, pleural effusions and cardiac remodeling," *Journal of radiation research,* vol. 56, no. 2, pp. 248-260, 2015.

[111] S. P. Soltoff, "ATP and the regulation of renal cell function," (in eng), *Annual review of physiology,* vol. 48, pp. 9-31, 1986.

[112] P. Hansell, W. J. Welch, R. C. Blantz, and F. Palm, "Determinants of kidney oxygen consumption and their relationship to tissue oxygen tension in diabetes and hypertension," *Clinical and experimental pharmacology & physiology,* vol. 40, no. 2, pp. 123-137, 2013.

[113] J. J. Cohen, "Is the function of the renal papilla coupled exclusively to an anaerobic pattern of metabolism?," (in eng), *The American journal of physiology,* vol. 236, no. 5, pp. F423-33, May 1979.

[114] J. L. Dunaief, T. Dentchev, G.-S. Ying, and A. H. Milam, "The role of apoptosis in age-related macular degeneration," *Archives of ophthalmology,* vol. 120, no. 11, pp. 1435-1442, 2002.

[115] F. Podesta *et al.*, "Bax is increased in the retina of diabetic subjects and is associated with pericyte apoptosis in vivo and in vitro," *The American journal of pathology,* vol. 156, no. 3, pp. 1025-1032, 2000.

[116] L. A. Kerrigan, D. J. Zack, H. A. Quigley, S. D. Smith, and M. E. Pease, "TUNEL-positive ganglion cells in human primary open-angle glaucoma," *Archives of ophthalmology,* vol. 115, no. 8, pp. 1031-1035, 1997.

[117] Y. Du, C. M. Miller, and T. Kern, "Hyperglycemia increases mitochondrial superoxide in retina and retinal cells," *Free Radical Biology and Medicine,* vol. 35, no. 11, pp. 1491-1499, 2003.

[118] N. G. Docherty *et al.*, "Endoglin regulates renal ischaemia–reperfusion injury," *Nephrology Dialysis Transplantation,* vol. 21, no. 8, pp. 2106-2119, 2006.

[119] M. Jerkic *et al.*, "Pulmonary hypertension in adult Alk1 heterozygous mice due to oxidative stress," *Cardiovascular research,* vol. 92, no. 3, pp. 375-384, 2011.

[120] M. Toporsian *et al.*, "Spontaneous adult-onset pulmonary arterial hypertension attributable to increased endothelial oxidative stress in a murine model of hereditary hemorrhagic telangiectasia," *Arteriosclerosis, thrombosis, and vascular biology,* vol. 30, no. 3, pp. 509-517, 2010.

[121] F. Seta, M. Rahmani, P. V. Turner, and C. D. Funk, "Pulmonary oxidative stress is increased in cyclooxygenase-2 knockdown mice with mild pulmonary hypertension induced by monocrotaline," *PLoS One,* vol. 6, no. 8, 2011.

[122] R. Brandes and D. M. Bers, "Increased work in cardiac trabeculae causes decreased mitochondrial NADH fluorescence followed by slow recovery," (in eng), *Biophys J,* vol. 71, no. 2, pp. 1024-35, Aug 1996.

[123] E. M. Nuutinen, "Subcellular origin of the surface fluorescence of reduced nicotinamide nucleotides in the isolated perfused rat heart," (in eng), *Basic Res Cardiol,* vol. 79, no. 1, pp. 49-58, Jan-Feb 1984.

[124] L. A. Katz, A. P. Koretsky, and R. S. Balaban, "Respiratory control in the glucose perfused heart. A 31P NMR and NADH fluorescence study," (in eng), *FEBS Lett,* vol. 221, no. 2, pp. 270-6, Sep 14 1987.

[125] R. W. Estabrook, "Fluorometric measurement of reduced pyridine nucleotide in cellular and subcellular particles," (in eng), *Analytical Biochemistry,* vol. 4, pp. 231-45, Sep 1962.

[126] B. Chance, P. Cohen, F. Jobsis, and B. Schoener, "Intracellular Oxidation-Reduction States in Vivo: The microfluorometry of pyridine nucleotide gives a continuous measurement of the oxidation state," *Science,* vol. 137, no. 3529, pp. 499-508, 1962.

[127] Y. Avi-Dor, J. M. Olson, M. D. Doherty, and N. O. Kaplan, "Fluorescence of pyridine nucleotides in mitochondria," *Journal of Biological Chemistry,* vol. 237, no. 7, pp. 2377-2383, 1962.

[128] L. K. Klaidman, A. C. Leung, and J. Adams, "High-performance liquid chromatography analysis of oxidized and reduced pyridine dinucleotides in specific brain regions," *Analytical biochemistry,* vol. 228, no. 2, pp. 312-317, 1995.

[129] M. O'Connor *et al.*, "Origin of labile NADH tissue fluorescence," *Oxygen Physiol. Funct,* vol. 10, no. 10, 1977.

[130] M. Fitzgerald *et al.*, "Near infrared light reduces oxidative stress and preserves function in CNS tissue vulnerable to secondary degeneration following partial transection of the optic nerve," (in eng), *J Neurotrauma,* vol. 27, no. 11, pp. 2107-19, Nov 2010.

[131] J. T. Eells, S. Gopalakrishnan, and K. Valter, "Near-infrared photobiomodulation in retinal injury and disease," in *Retinal Degenerative Diseases. Advances in Experimental Medicine and Biology*, no. 854): Springer, 2016, pp. 437-441.

[132] F. Palm and L. Nordquist, "Renal oxidative stress, oxygenation, and hypertension," *American Journal of Physiology-Regulatory, Integrative and Comparative Physiology,* vol. 301, no. 5, pp. R1229-R1241, 2011.

[133] N. Tomar *et al.*, "A thermodynamically-constrained mathematical model for the kinetics and regulation of NADPH oxidase 2 complex-mediated electron transfer and superoxide production," *Free Radical Biology and Medicine,* vol. 134, pp. 581-597, 2019.

[134] J. Francis and R. L. Davisson, "Emerging concepts in hypertension," ed: Mary Ann Liebert, Inc. 140 Huguenot Street, 3rd Floor New Rochelle, NY 10801 USA, 2014.

[135] R. Rodrigo, J. González, and F. Paoletto, "The role of oxidative stress in the pathophysiology of hypertension," *Hypertension Research,* vol. 34, no. 4, pp. 431-440, 2011.

[136] T. Mori and A. W. Cowley, Jr., "Renal oxidative stress in medullary thick ascending limbs produced by elevated NaCl and glucose," (in eng), *Hypertension,* vol. 43, no. 2, pp. 341-6, Feb 2004.

[137] A. Makino, M. M. Skelton, A. P. Zou, R. J. Roman, and A. W. Cowley, Jr., "Increased renal medullary oxidative stress produces hypertension," (in eng), *Hypertension,* vol. 39, no. 2 Pt 2, pp. 667-72, Feb 2002.

[138] S. I. Dikalov and A. E. Dikalova, "Contribution of mitochondrial oxidative stress to hypertension," *Current opinion in nephrology and hypertension,* vol. 25, no. 2, p. 73, 2016.

[139] S. I. Dikalov and Z. Ungvari, "Role of mitochondrial oxidative stress in hypertension," *American Journal of Physiology-Heart and Circulatory Physiology,* vol. 305, no. 10, pp. H1417-H1427, 2013.

[140] S. Rubattu *et al.*, "Pathogenesis of target organ damage in hypertension: role of mitochondrial oxidative stress," *International Journal of Molecular Sciences,* vol. 16, no. 1, pp. 823-839, 2015.

[141] A. W. Cowley, Jr., "Renal medullary oxidative stress, pressure-natriuresis, and hypertension," (in eng), *Hypertension,* vol. 52, no. 5, pp. 777-86, Nov 2008.

[142] A. K. Camara, E. J. Lesnefsky, and D. F. Stowe, "Potential therapeutic benefits of strategies directed to mitochondria," *Antioxidants & redox signaling,* vol. 13, no. 3, pp. 279-347, 2010.

[143] D. F. Stowe and A. K. Camara, "Mitochondrial reactive oxygen species production in excitable cells: modulators of mitochondrial and cell function," *Antioxidants & redox signaling,* vol. 11, no. 6, pp. 1373-1414, 2009.

[144] M. Lenarczyk *et al.*, "Chronic oxidative stress as a mechanism for radiation nephropathy," *Radiation research,* vol. 171, no. 2, pp. 164-172, 2009.

[145] E. P. Cohen, B. L. Fish, J. D. Imig, and J. E. Moulder, "Mitigation of normal tissue radiation injury: evidence from rat radiation nephropathy models," *Journal of Radiation Oncology,* vol. 5, no. 1, pp. 1-8, 2016/03/01 2016.

[146] J. E. Moulder, E. P. Cohen, and B. L. Fish, "Mitigation of experimental radiation nephropathy by renin-equivalent doses of angiotensin converting enzyme inhibitors," *International journal of radiation biology,* vol. 90, no. 9, pp. 762-768, 2014.

[147] A. K. Camara, M. Bienengraeber, and D. F. Stowe, "Mitochondrial approaches to protect against cardiac ischemia and reperfusion injury," *Frontiers in physiology,* vol. 2, p. 13, 2011.

[148] M. Aldakkak, D. F. Stowe, Q. Chen, E. J. Lesnefsky, and A. K. Camara, "Inhibited mitochondrial respiration by amobarbital during cardiac ischaemia improves redox state and reduces matrix Ca2+ overload and ROS release," *Cardiovascular research,* vol. 77, no. 2, pp. 406-415, 2008.

[149] K. M. Quesnelle, P. V. Bystrom, and L. H. Toledo-Pereyra, "Molecular responses to ischemia and reperfusion in the liver," *Archives of toxicology,* vol. 89, no. 5, pp. 651-657, 2015.

[150] B. G. Bruinsma *et al.*, "Metabolic profiling during ex vivo machine perfusion of the human liver," *Scientific reports,* vol. 6, 2016.

[151] Y. Wu and J. Y. Qu, "Autofluorescence spectroscopy of epithelial tissues," *J Journal of biomedical optics,* vol. 11, no. 5, p. 054023, 2006.

[152] K. Staniszewski, S. H. Audi, R. Sepehr, E. R. Jacobs, and M. Ranji, "Surface fluorescence studies of tissue mitochondrial redox state in isolated perfused rat lungs," *Annals of biomedical engineering,* vol. 41, no. 4, pp. 827-836, 2013.

[153] S. R. Sternberg, "Biomedical image processing," *Computer,* no. 1, pp. 22-34, 1983.

[154] T. Pécot *et al.*, "Background fluorescence estimation and vesicle segmentation in live cell imaging with conditional random fields," *IEEE Transactions on Image Processing,* vol. 24, no. 2, pp. 667-680, 2014.

[155] A. A. Taha and A. Hanbury, "Metrics for evaluating 3D medical image segmentation: analysis, selection, and tool," *J BMC medical imaging,* vol. 15, no. 1, p. 29, 2015.

[156] C. D. Murray, "The physiological principle of minimum work: I. The vascular system and the cost of blood volume," *Proceedings of the National Academy of Sciences of the United States of America,* vol. 12, no. 3, p. 207, 1926.

[157] S. Mehrvar *et al.*, "Fluorescence Imaging of Mitochondrial Redox State to Assess Diabetic Wounds," *IEEE Journal of Translational Engineering in Health and Medicine,* vol. 7, pp. 1-9, 2019.

[158] F. Stewart, S. Hoving, and N. Russell, "Vascular damage as an underlying mechanism of cardiac and cerebral toxicity in irradiated cancer patients," *Radiation research,* vol. 174, no. 6b, pp. 865-869, 2010.

[159] E. Vorob'ev and R. Stepanov, "Ionizing radiations and blood vessels," 1985.

[160] K. Tainaka, A. Kuno, S. I. Kubota, T. Murakami, and H. R. Ueda, "Chemical principles in tissue clearing and staining protocols for whole-body cell profiling," *Annual review of cell and developmental biology,* vol. 32, pp. 713-741, 2016.

[161] J. M. Watson *et al.*, "Two-photon excited fluorescence imaging of endogenous contrast in a mouse model of ovarian cancer," *Lasers in surgery and medicine,* vol. 45, no. 3, pp. 155-166, 2013.

[162] X. Su, C. M. Sorenson, and N. Sheibani, "Isolation and characterization of murine retinal endothelial cells," (in eng), *Mol Vis,* vol. 9, pp. 171-8, May 1 2003.

[163] B. A. Roelofs, X. G. Shealinna, P. E. Studlack, and B. M. Polster, "Low micromolar concentrations of the superoxide probe MitoSOX uncouple neural mitochondria and inhibit complex IV," *Free Radical Biology and Medicine,* vol. 86, pp. 250-258, 2015.

[164] Z. Ghanian, S. Mehrvar, N. Jamali, N. Sheibani, and M. Ranji, "Time-lapse microscopy of oxidative stress demonstrates metabolic sensitivity of retinal pericytes under high glucose condition," *Journal of biophotonics,* p. e201700289, 2018.

[165] U. Förstermann and W. C. Sessa, "Nitric oxide synthases: regulation and function," *European heart journal,* vol. 33, no. 7, pp. 829-837, 2012.

[166] W. C. Sessa, "Regulation of endothelial derived nitric oxide in health and disease," *Memórias do Instituto Oswaldo Cruz,* vol. 100, pp. 15-18, 2005.

[167] A. B. El-Remessy, G. Abou-Mohamed, R. W. Caldwell, and R. B. Caldwell, "High glucose-induced tyrosine nitration in endothelial cells: role of eNOS uncoupling and aldose reductase activation," *Investigative ophthalmology & visual science,* vol. 44, no. 7, pp. 3135-3143, 2003.

[168] I. Fleming and R. Busse, "Molecular mechanisms involved in the regulation of the endothelial nitric oxide synthase," *American Journal of Physiology-Regulatory, Integrative and Comparative Physiology,* vol. 284, no. 1, pp. R1-R12, 2003.

[169] F. M. Ho, S. H. Liu, C. S. Liau, P. J. Huang, S. G. Shiah, and S. Y. Lin-Shiau, "Nitric oxide prevents apoptosis of human endothelial cells from high glucose exposure during early stage," *Journal of cellular biochemistry,* vol. 75, no. 2, pp. 258-263, 1999.

[170] M. Kalbáčová, M. Vrbacký, Z. Drahota, and Z. Mělková, "Comparison of the effect of mitochondrial inhibitors on mitochondrial membrane potential in two different cell lines

using flow cytometry and spectrofluorometry," *Cytometry Part A: The Journal of the International Society for Analytical Cytology,* vol. 52, no. 2, pp. 110-116, 2003.

[171] E. Cadenas and A. Boveris, "Enhancement of hydrogen peroxide formation by protophores and ionophores in antimycin-supplemented mitochondria," *Biochemical Journal,* vol. 188, no. 1, pp. 31-37, 1980.

[172] Y.-L. Dong, P.-J. Zhou, S.-Y. Jiang, X.-W. Pan, and X.-H. Zhao, "Induction of oxidative stress and apoptosis by pentachlorophenol in primary cultures of Carassius carassius hepatocytes," *Comparative biochemistry and physiology. Toxicology & pharmacology: CBP,* vol. 150, no. 2, pp. 179-185, 2009.

[173] M. Aon, S. Cortassa, and B. O'Rourke, "Redox-optimized ROS balance: a unifying hypothesis," *Biochimica et Biophysica Acta (BBA)-Bioenergetics,* vol. 1797, no. 6-7, pp. 865-877, 2010.

[174] R. F. Feissner, J. Skalska, W. E. Gaum, and S.-S. Sheu, "Crosstalk signaling between mitochondrial Ca2+ and ROS," *Frontiers in bioscience: a journal and virtual library,* vol. 14, p. 1197, 2009.

[175] F. Giacco and M. Brownlee, "Oxidative stress and diabetic complications," *Circulation research,* vol. 107, no. 9, pp. 1058-1070, 2010.

[176] J. V. Busik, S. Mohr, and M. B. Grant, "Hyperglycemia-induced reactive oxygen species toxicity to endothelial cells is dependent on paracrine mediators," *Diabetes,* vol. 57, no. 7, pp. 1952-1965, 2008.

[177] K. Trudeau, A. J. Molina, and S. Roy, "High glucose induces mitochondrial morphology and metabolic changes in retinal pericytes," *Investigative ophthalmology & visual science,* vol. 52, no. 12, pp. 8657-8664, 2011.

[178] L. J. Mandarino, J. Finlayson, and J. Hassell, "High glucose downregulates glucose transport activity in retinal capillary pericytes but not endothelial cells," *Investigative ophthalmology & visual science,* vol. 35, no. 3, pp. 964-972, 1994.

Curriculum Vitae:

Shima Mehrvar

EDUCATION

PhD Candidate in Electrical Engineering   (2016 – Present)
University of Wisconsin-Milwaukee, Minor: Biomedical Engineering, GPA: 3.96/4
Advisor: Dr. Mahsa Ranji, Thesis title: *Quantitative optical imaging of metabolic and structural biomarkers in rodent injury models*

Master of Science in Biomedical Engineering   (2011 – 2013)
Amirkabir University of Technology, GPA: 3.94/4
Thesis: *Nonlinear speech analysis and synthesis for enhancement using neural networks*

Bachelor of Science in Electrical Engineering   (2007 – 2011)
Shahid Beheshti University, GPA: 3.68/4

RESEARCH EXPERIENCES

Research Assistant – Dissertator Fellow   (2016 – Present)
Biophotonics Lab, University of Wisconsin-Milwaukee

Image Processing
- Designed an algorithm to segment 3D vascular network of multiple organs
- Performed 3D vascular reconstruction, visualization, and quantification
- Segmented live cells and their mitochondrial compartment in time-lapse microscopy images
- Optimized a segmentation algorithm using parallel processing

Biomedical Imaging
- Developed a fluorescence imager, as a diagnostic tool for diabetes:
  - Optical design, prototyping, system evaluation
  - Implementing graphical user interface using LabVIEW
  - Establishing experimental protocol for IACUC and IRB confirmation
  - Imaging, data collection, image processing, and statistical analysis
- Investigated multiple animal models using fluorescence cryo-imaging

Interpersonal
- Collaborated in a multi-disciplinary team of five to ten people
- Led multiple projects simultaneously as a senior member

Research Assistant   (2011 – 2014)
Speech Processing Lab, Amirkabir University of Technology

Machine Learning
- Enhanced speech quality using deep NN, RNN
- Modeled human tendency via interactions between attractors in ANN
- Optimized the structure of a CNN for face recognition

PUBLICATIONS

Patent

– S. Mehrvar, M. Ranji, "Label-free 3D vascular extraction," Approved IP by UWMRF (2019)

Journal Publications

1. **S. Mehrvar**, S. Mostaghimi, F. Foomani, M. Medhora, A. Camara, and M. Ranji, "3D vascular-metabolic imaging using inverted intrinsic fluorescence," (In submission).

2. **S. Mehrvar**, K. Rymut, F. Foomani, S. Mostaghimi, J. Eells, S. Gopalakrishnan, and M. Ranji, "670nm Photobiomodulation Improves the Mitochondrial Redox State in Diabetic Wounds," (Submitted).

3. S. Gopalakrishnan, **S. Mehrvar**, S. Maleki, H. Schmitt, P. Summerfelt, A. M. Dubis, B. Abroe, T. B. Connor, J. Carroll, W. Huddleston, M. Ranji, and J. T. Eells, "Photobiomodulation Preserves Mitochondrial Redox State and is Retinoprotective in a Rodent Model of Retinitis Pigmentosa," (In preparation).

4. **S. Mehrvar**, F. Foomani, S. Shimada, C. Yang, N. Zheleznova, S. Mostaghimi, A Cowley, and M. Ranji, "The Early Effects of Uninephrectomy on Rat Kidney Metabolic State Using Optical Imaging," *Journal of Biophotonics*, (Under revision).

5. **S. Mehrvar**, K. Rymut, F. Foomani, S. Mostaghimi, J. Eells, M. Ranji, and S. Gopalakrishnan, "Noninvasive fluorescence imaging of mitochondrial redox state to assess diabetic wounds," *IEEE Journal of Translational Engineering and Health Medicine*, (2019)

6. **S. Mehrvar**, M. la Cour, M. Medhora, A. Camara, and M. Ranji, "Optical Metabolic Imaging for Assessment of Radiation-Induced Injury to Rat Kidney and Mitigating by Lisinopril," *Annals of Biomedical Engineering*, (2019)

7. S. Lewis, T. Takimoto, **S. Mehrvar**, H. Higuchi, A. Doebley, G. Stokes, N. Sheibani, S. Ikeda, M. Ranji, and A. Ikeda. "The effect of Tmem135 overexpression on the mouse heart," *PloS one*, (2018)

8. P. Kadamati, J. Sugar, B. Quirk, **S. Mehrvar**, G. Chelimsky, T. Chelimsky, H. Whelan, and M. Ranji, "Near-infrared spectroscopy muscle oximetry of patients with postural orthostatic tachycardia syndrome," *Journal of Innovative Optical Health Sciences*, (2018)

9. Z. Ghanian, **S. Mehrvar**, N. Jamali, N. Sheibani, and M. Ranji, "Time-lapse microscopy of oxidative stress demonstrates metabolic sensitivity of retinal pericytes under high glucose condition," *Journal of Biophotonics*, (2018)

10. **S. Mehrvar**, M. la Cour, J. Heisner, M. MasoudiMotlagh, M. Medhora, M. Ranji, A. Camara, "Optical metabolic imaging of irradiated rat heart exposed to ischemia–reperfusion injury," *Journal of Biomedical Optics*, (2018)

11. **S. Mehrvar**, M. la Cour, J. Kim, A. Martin, M. A. Zimmerman, J. Hong, and M. Ranji, "Optical imaging for the assessment of hepatocyte metabolic state in ischemia and reperfusion injuries," *Biomedical Optics Express*, (2017)

Selected Conference & Presentation

1. **S. Mehrvar**, K.T. R S. Mostaghimi, **S. Mehrvar**, F. Foomani, B. Abroe, J.T. Eells, M. Ranji, and S. Gopalakrishnan, "The Effect of NIR Light Treatment in Metabolic State of Diabetic Wounds," *BMES*, Philadelphia (2019)

2. **S. Mehrvar**, F. Foomani, S. Mostaghimi, M. Medhora, A. Camara, and M. Ranji, **"**Radiation-induced Injuries to Rat Kidney Vasculature," *BMES*, Philadelphia (2019)

3. F. Foomani, **S. Mehrvar**, S. Mostaghimi, S. Shimada, C. Yang, N. Zheleznova, Allen Cowley, and Mahsa Ranji, **"**The Early Effects of Uninephrectomy on Rat Kidney Metabolic State Using Optical Imaging," *BMES*, Philadelphia (2019)

4. **S. Mehrvar**, K.T. Rymut, J.T. Eells, M. Ranji, and S. Gopalakrishnan, "Optical imaging for the metabolic redox state assessment of wound healing in diabetic mice," *Biophotonics Congress: Optics in the Life Sciences*, Tucson (2019)

5. **S. Mehrvar**, M.F. la Cour, M. Medhora, A.K.S. Camara, and M. Ranji, "Optical cryoimaging for assessment of radiation-induced injury to rat kidney metabolic state," *Proc. of SPIE*, San Francisco (2018)

6. **S. Mehrvar**, K.T. Rymut, J.T. Eells, M. Ranji, and S. Gopalakrishnan, "When time does not heal wounds: optical imaging of diabetic wounds," *three-minute thesis competition (3MT)*, Milwaukee (2018)

7. **S. Mehrvar**, F. Foomani, S. Mostaghimi, M. Medhora, A. Camara, and M. Ranji, "Optical cryoimaging to assess metabolic state of radiation-induced injury in rat kidney," *SPIE BIOS*, San Francisco (2018*)*

8. **S. Mehrvar**, M. la Cour, J. Kim, A. Martin, M. A. Zimmerman, J. Hong, and M. Ranji, "Optical imaging for liver transplant application," *5th Annual Solid Organ Transplantation Research Symposium*, Milwaukee (2017)

9. Z. Ghanian, **S. Mehrvar**, N. Jamali, N. Sheibani, and M. Ranji, "A Comparison of retina endothelial cells and pericytes in metabolic sensitivity using time-lapse microscopy," *McPherson Eye Research Institute Poster Session*, Madison (2017)

10. **S. Mehrvar**, M.F. la Cour, M. Medhora, A.K.S. Camara, and M. Ranji, "Ischemia reperfusion in hearts: optical cryo-imaging," *Milwaukee Engineering Research Conference*, Milwaukee (2017)

11. **S. Mehrvar**, M.F. la Cour, M. Medhora, A.K.S. Camara, and M. Ranji, "Optical Cryoimaging of Hearts during Ischemia and Reperfusion," *IEEE Larry Hause Student Poster Competition*, Milwaukee (2017)

12. **S. Mehrvar**, Z. Ghanian, G. Kondouri, A.K.S. Camara, M. Ranji, "Time-lapse microscopy of lung endothelial cells under hypoxia," *Proc. of SPIE*, San Francisco (2017)

HONORS & AWARDS

− Distinguished Dissertator Fellow (2019)
− Featured graduate student in Graduate School Viewbook (2018)
− Featured in UWM report article "*Grad students' research aims to change our world*" (2018)

- Finalist in three-minute thesis (3MT) competition   (2018)
- Second place in IEEE Larry Hause Student Poster Competition   (2017 & 2019)
- Chancellor's Graduate Student Awardee   (2016 & 2017)